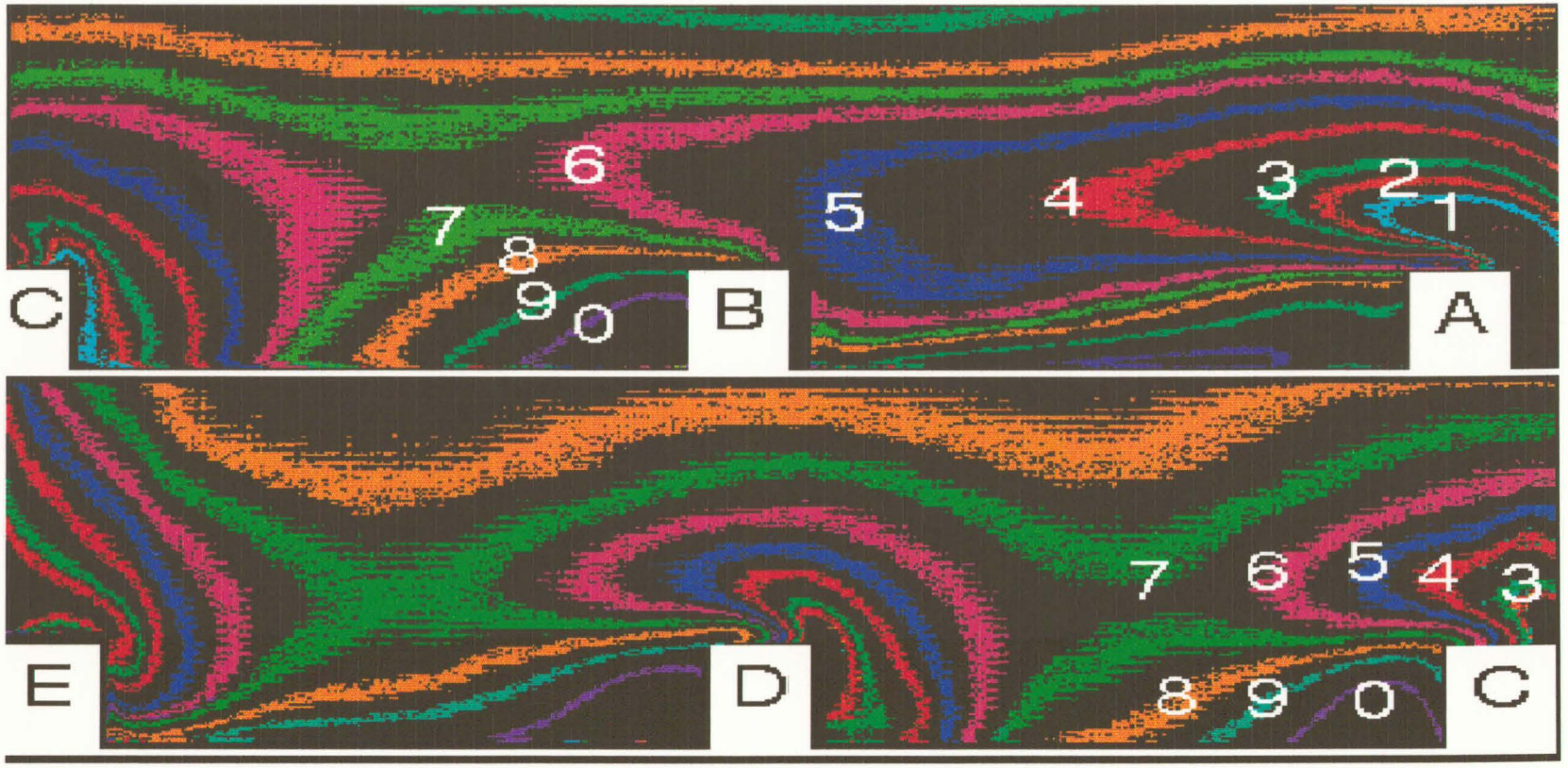

FIGURE 3.26 False colour images indicating the iso-Nusselt number lines for Re=20000 between the 1st and 3rd rib (top) and 3rd and 5th rib (bottom)

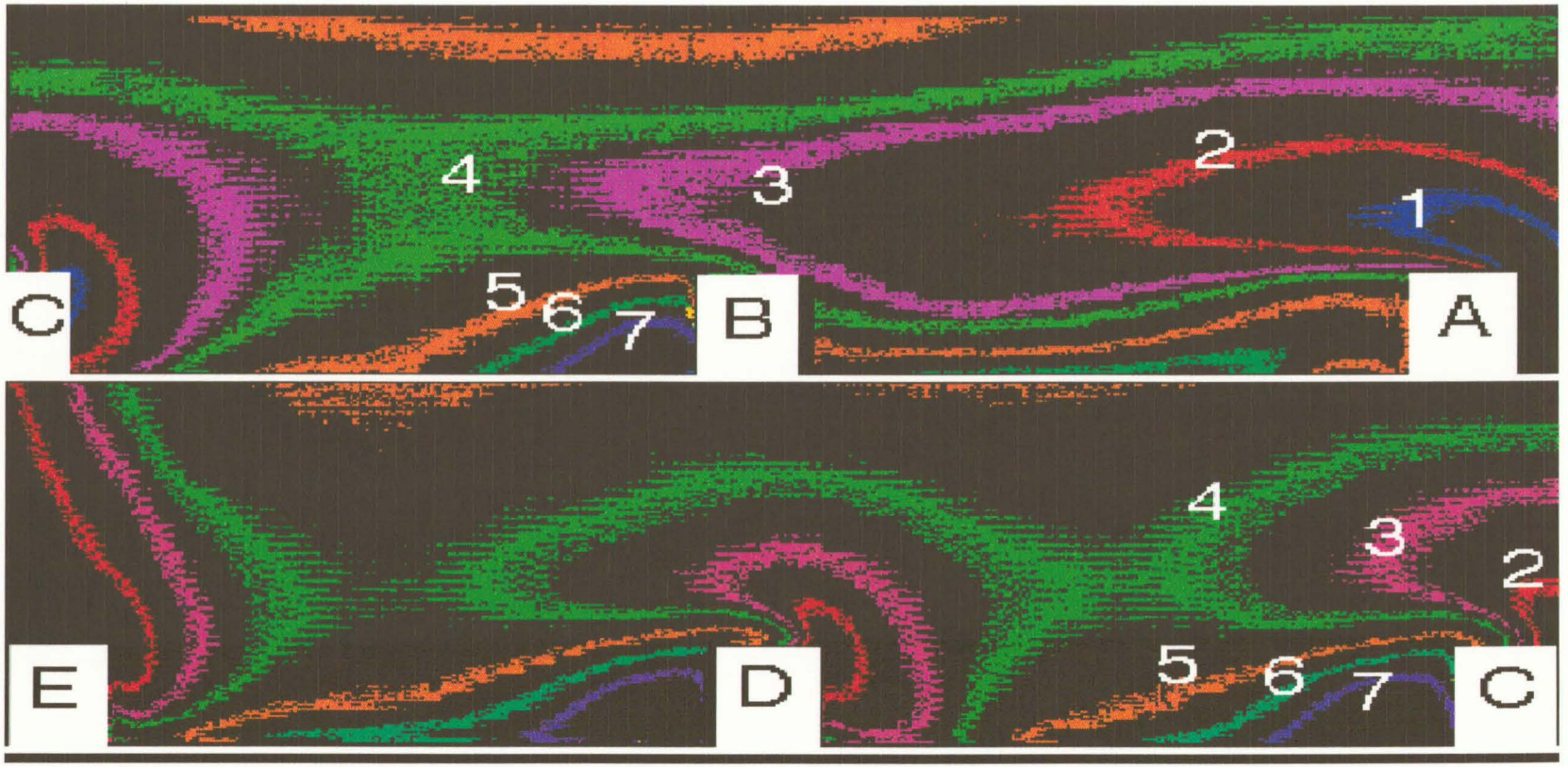

FIGURE 3.27 False colour images indicating the iso-Nusselt number lines for Re=10000 between the 1st and 3rd rib (top) and 3rd and 5th rib (bottom)

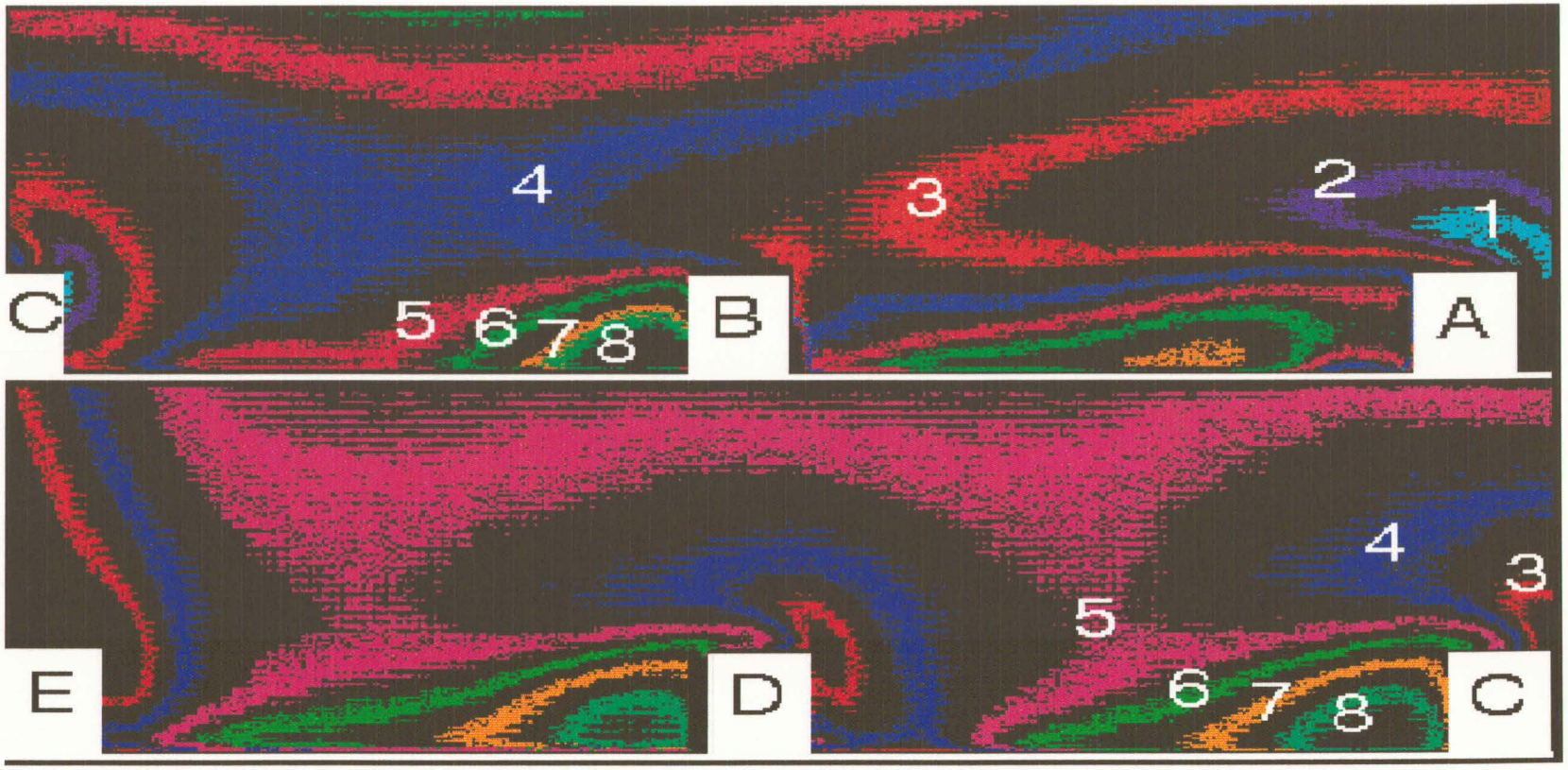

FIGURE 3.28 False colour images indicating the iso-Nusselt number lines for Re=6000 between the 1st and 3rd rib (top) and 3rd and 5th rib (bottom)

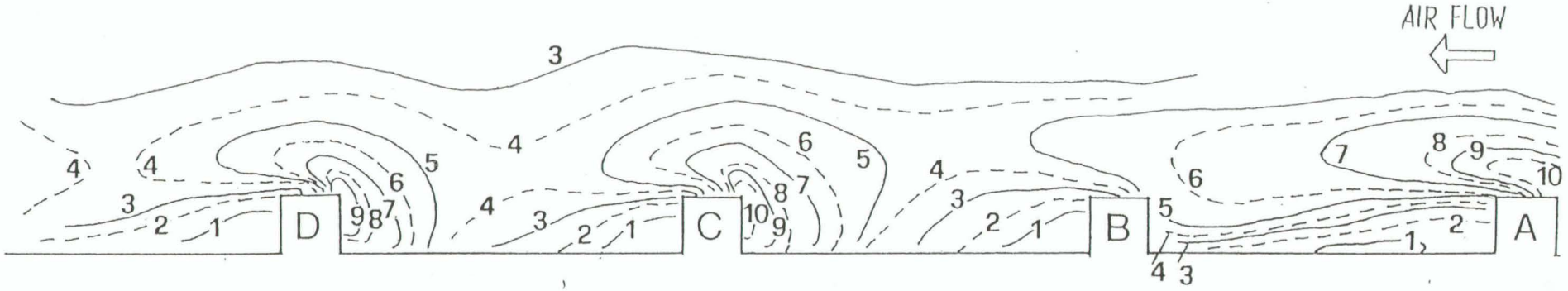

FIGURE 3.29 Contours of lines at equal Nu number, Re=20000.
1,(Nu=) 79; **2**,99; **3**,113; **4**,123; **5**,136; **6**,147; **7**,160; **8**,175; **9**,185; **10**,209.

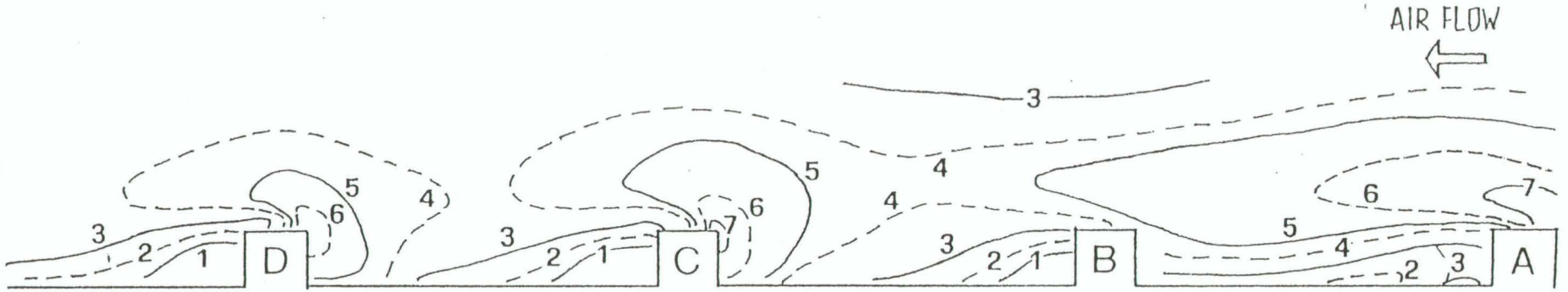

FIGURE 3.30 Contours of lines at equal Nu number, Re=10000.
1,(Nu=) 52; **2**,61; **3**,72; **4**,85; **5**,93; **6**,112; **7**,131.

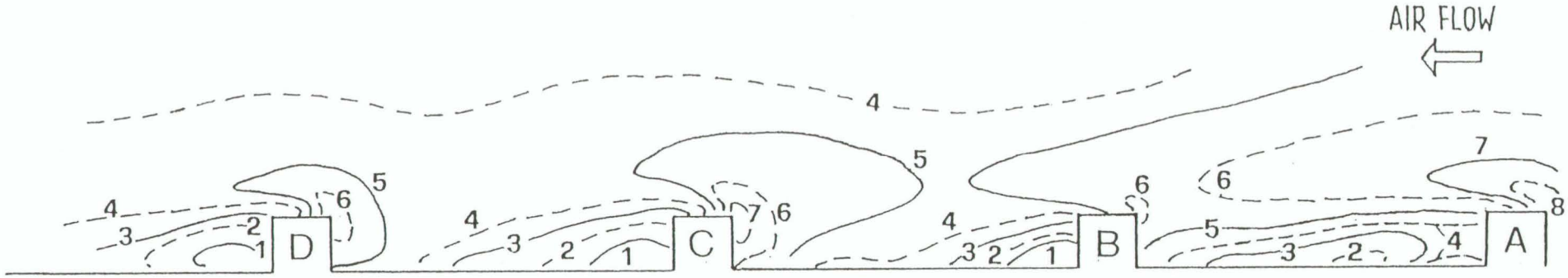

FIGURE 3.31 Contours of lines at equal Nu number, Re=6000.
1,(Nu=) 40; **2**,44; **3**,49; **4**,56; **5**,62; **6**,74; **7**,91; **8**,100.

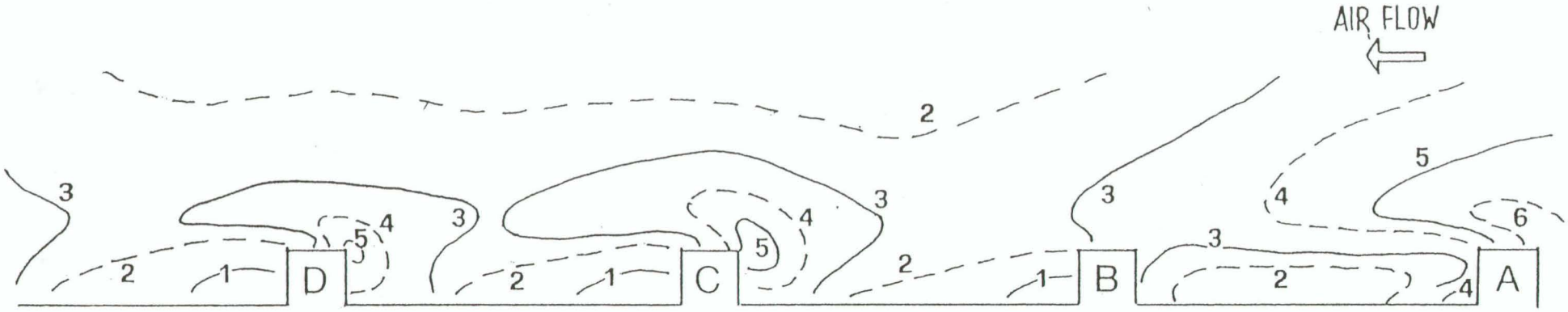

FIGURE 3.32 Contours of lines at equal Nu number, Re=3500.
1,(Nu=) 38; **2**,49; **3**,57; **4**,63; **5**,71; **6**,79.

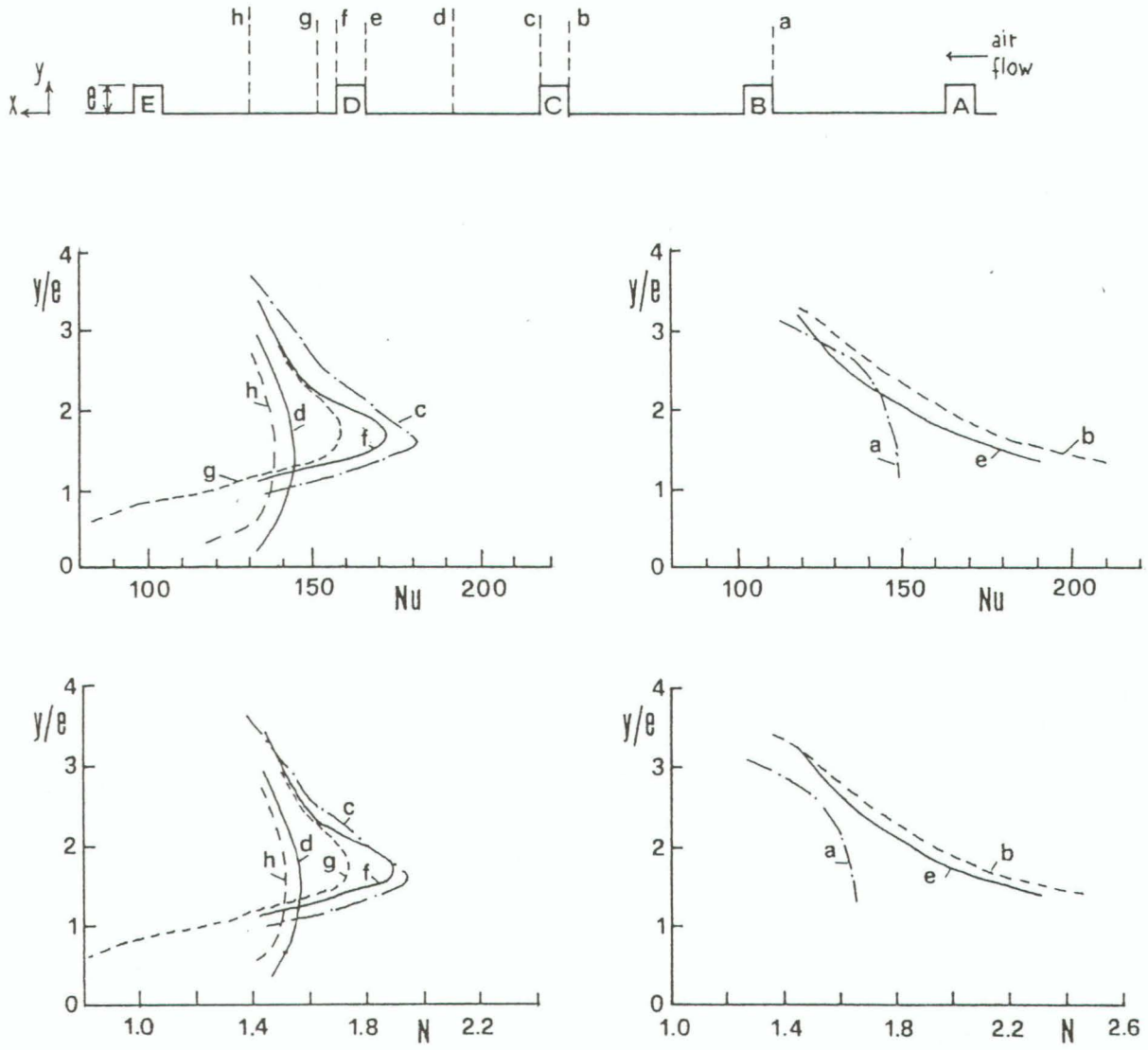

FIGURE 3.33 Nu and N profiles along y-coordinate at several axial x-locations, Re=20000.

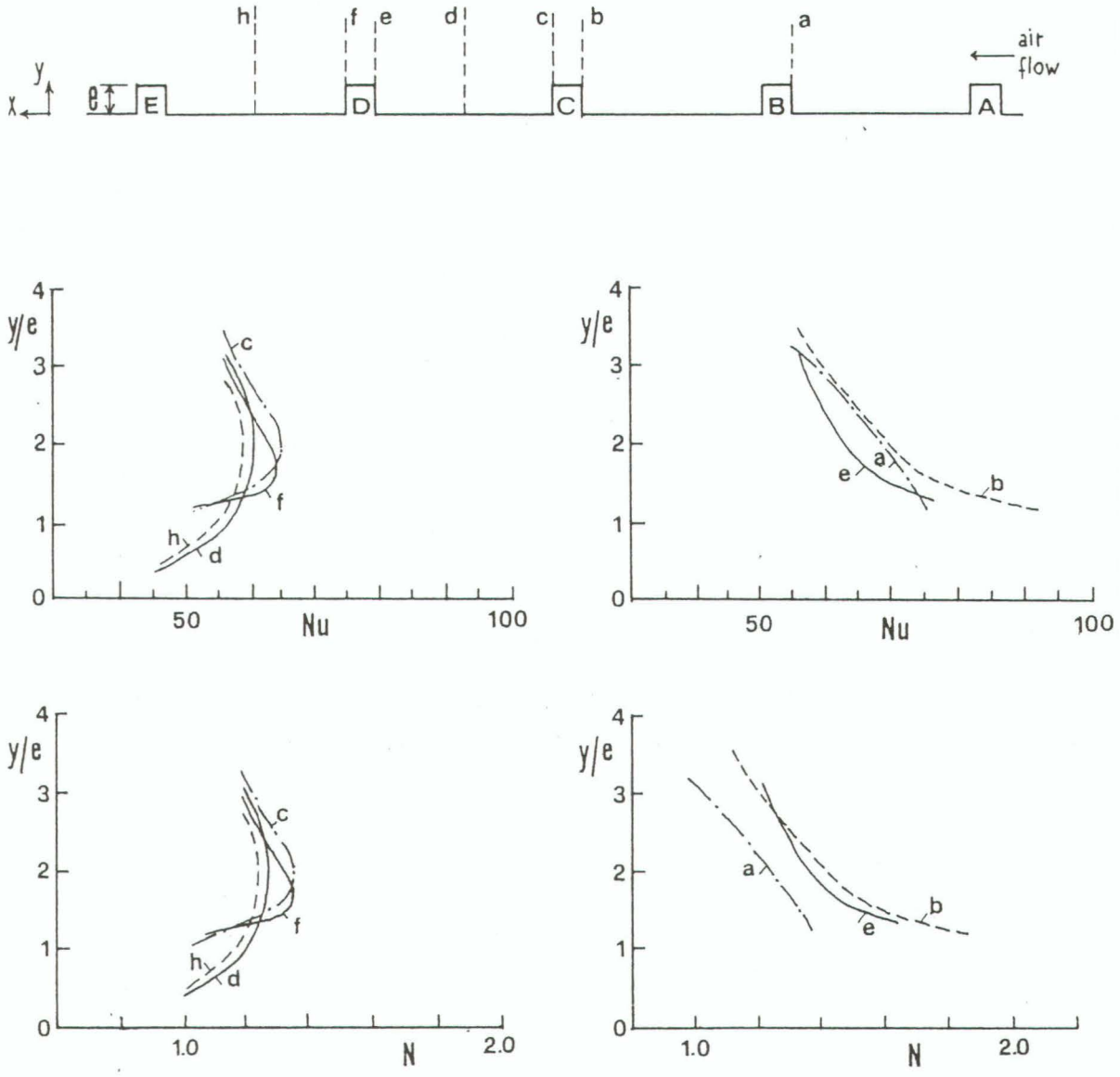

FIGURE 3.34 Nu and N profiles along y-coordinate at several axial x-locations, Re=6000.

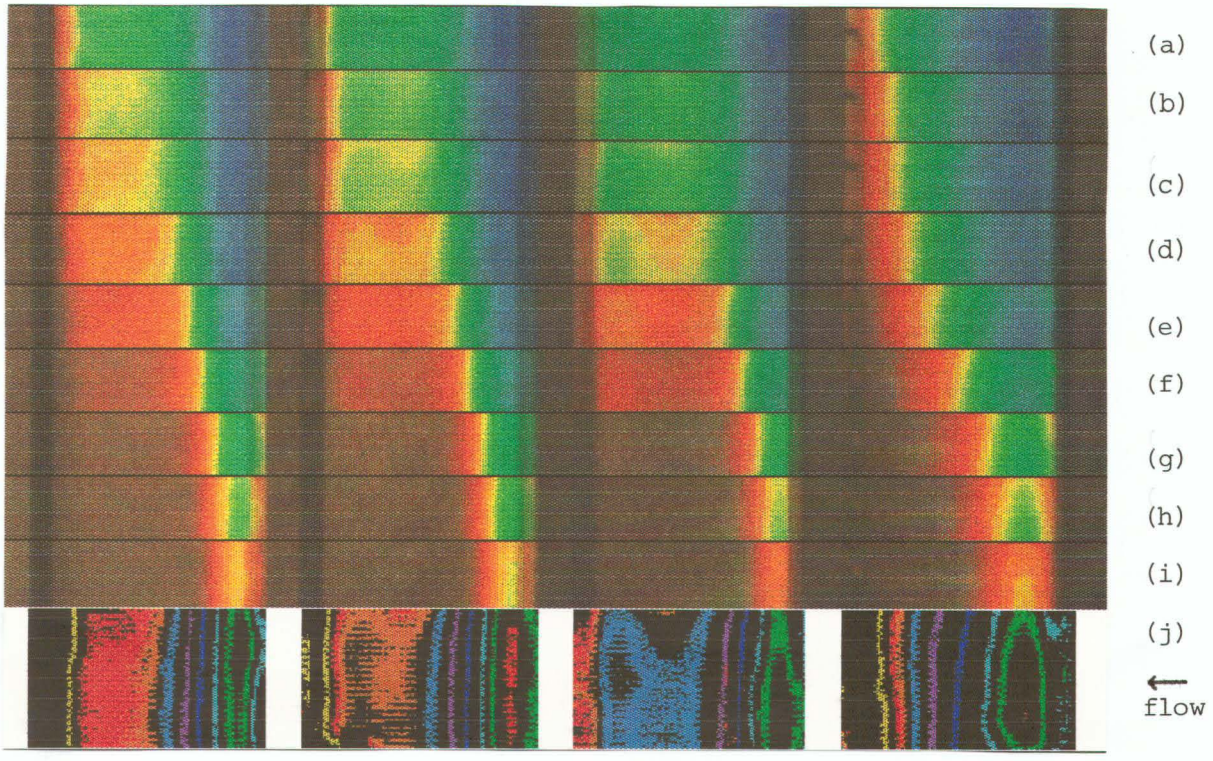

FIGURE 3.35 (a-i) LC true-colour images for nine experiments at fixed Re and different water temperature; (j) false-colour image indicating the iso-Nusselt lines. Re=20000.

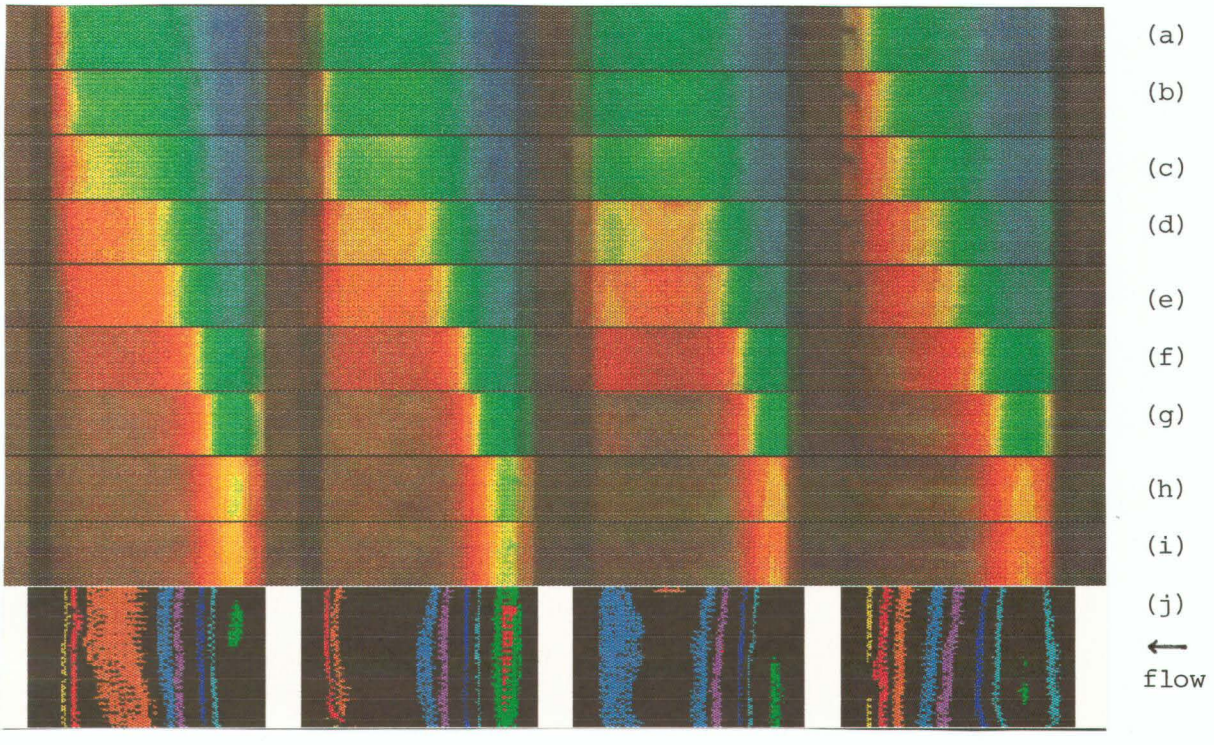

FIGURE 3.36 (a-i) LC true-colour images for nine experiments at fixed Re and different water temperature; (j) false-colour image indicating the iso-Nusselt lines. Re=10000.

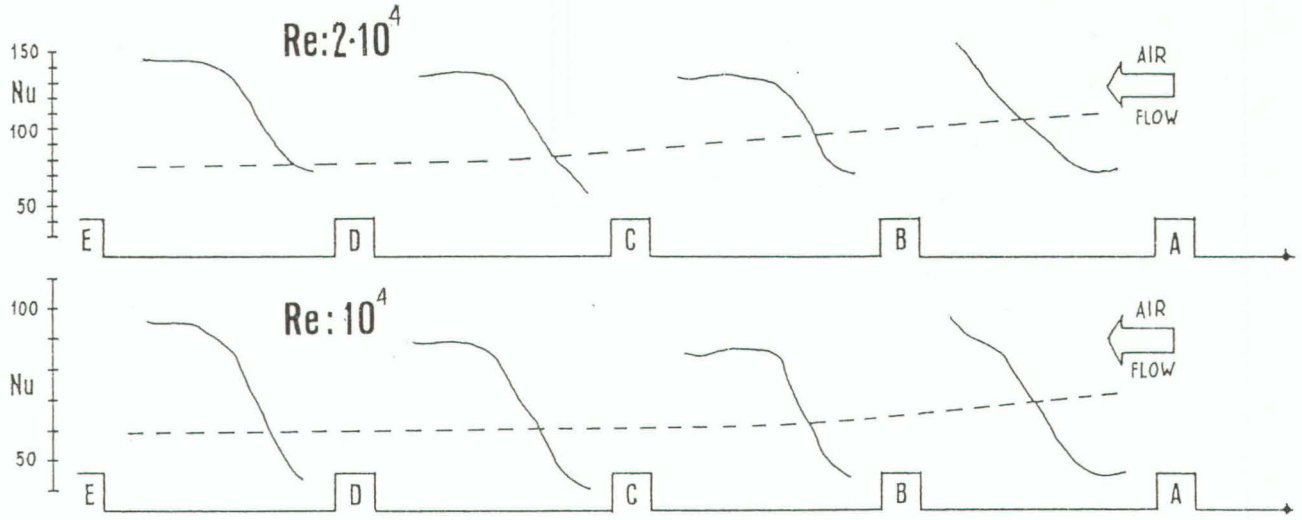

FIGURE 3.37 Local Nu number distributions along the test plate (continuous line: ribbed config. R2, dashed line: flat plate) for Re=20000 (top) and Re=10000 (bottom).

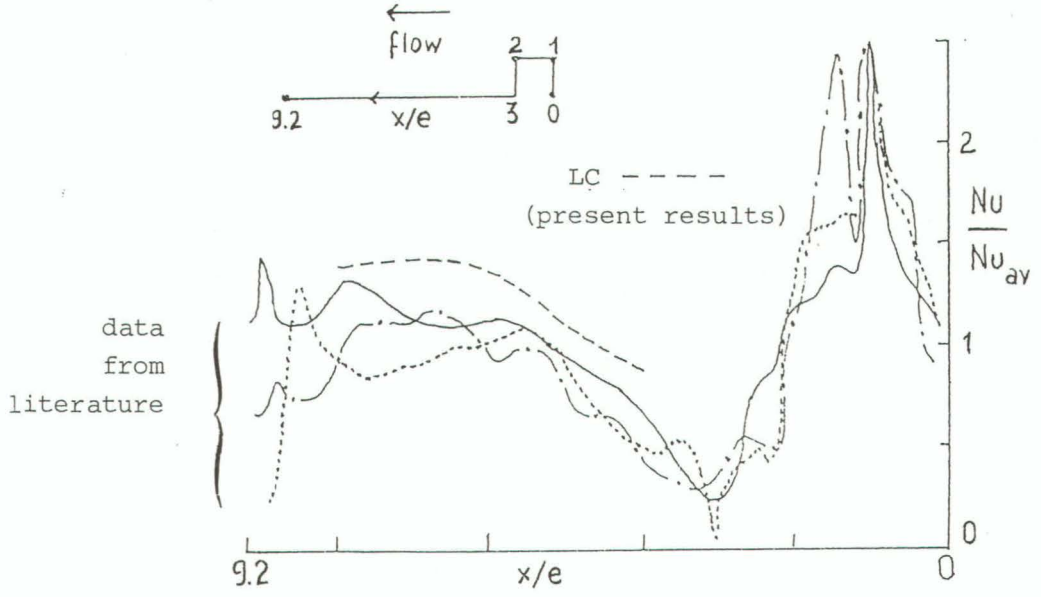

FIGURE 3.38 Normalised Nusselt number distributions. Comparison among present results and data from the literature, ribbed configuration R2

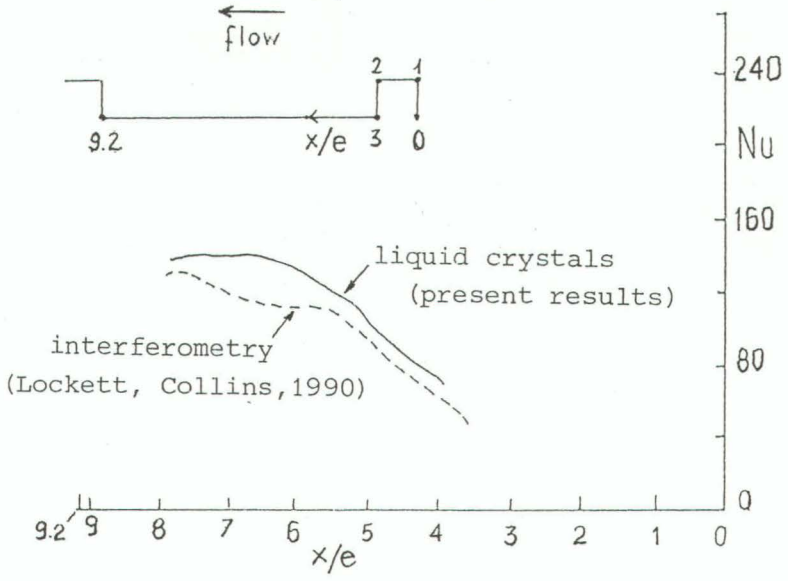

FIGURE 3.39 Nusselt number distributions. Comparison between present results and data from Lockett and Collins,1990. Re≈ 20000, ribbed config.R2

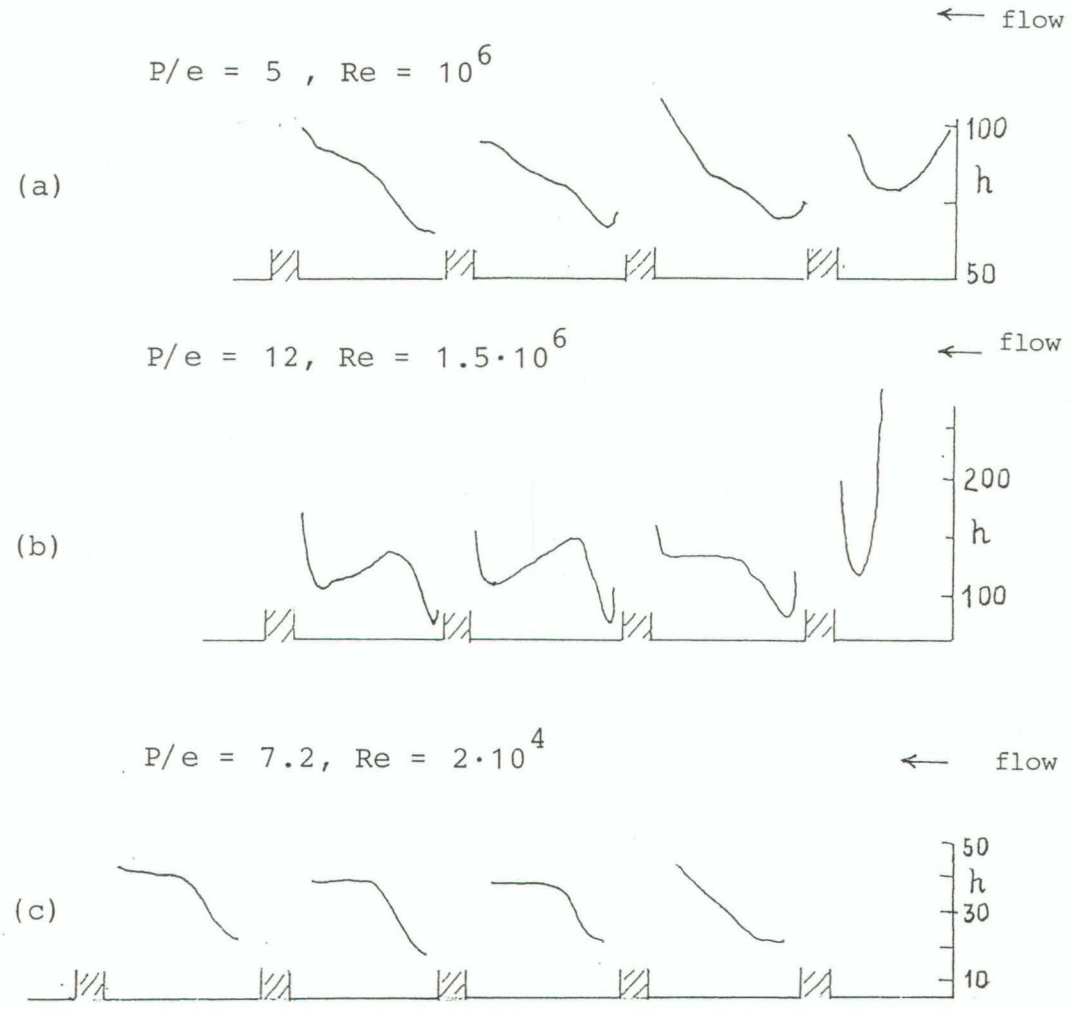

FIGURE 3.40 Local heat transfer coefficient distributions. (a-b) data from Aliaga et al.,1994; (c) present results.

4. EXPERIMENTS BY THE SCHLIEREN METHOD IN RIB-ROUGHENED CHANNELS

The schlieren method has been employed here to investigate free convection heat transfer in vertical rib-roughened channels. As in the forced convection experiments, additional tests have also been performed for the corresponding smooth channel, in order to compare the heat transfer behaviour with and without the ribs.

4.1 The apparatus

The experimental apparatus includes: (a) the test section, (b) the instrumentation for measuring temperature, electrical power and pressure, (c) the optical system, (d) the image processing system.

The test section was entirely designed by the author of this project, as well as the procedure for obtaining heat transfer coefficients and temperature distributions from schlieren images (Tanda 1992a, 1992b, 1993a, 1993b, Tanda 1995). Whereas in previous schlieren experiments conducted by the author the index-of-refraction gradients were recorded only along one direction, here the apparatus was modified in order to detect n gradients along two directions, owing to the characteristic shape of the ribbed walls. In addition, an image processing system including "self-made" dedicated software has been employed to reconstruct the thermal field from schlieren images.

4.1.1. The test section

The test section is schematically shown in Fig.4.1. Two aluminium ribbed walls, with three plane electrical resistances sandwiched between them, are faced by two insulated walls to form two symmetrical vertical channels. Each ribbed wall was fabricated from a solid block of aluminium and therefore the ribs were integral to the baseplate, without thermal contact resistance between them. The two insulated walls were made of perspex (thickness 4 mm) with an insulation layer on the rear and a plastic reflective sheet on the face opposite to aluminium walls, to reduce radiant heat transfer from the heated walls.

Owing to the symmetry of the geometrical configuration, the heat power dissipated by the Joule effect into the aluminium plates was expected to be transferred equally to the air flowing in the two channels. The main reasons for choosing a symmetrical configuration are (a) to evaluate the

total power dissipated into the fluid by electric measurement with great accuracy and (b) to provide an effective check of schlieren local heat transfer measurement, where the integral of local heat transfer must be equal to the overall power dissipated.

An additional plate assembly was arranged by using two flat aluminium sheets (without ribs). Three plane resistors were fitted inside them, as in the previous case. Experiments in the presence of the plane heated walls (in lieu of the ribbed heated walls) were carried out for the following reasons:

(i) free convection inside a channel with one heated wall and one adiabatic wall has been extensively studied in the past and a considerable quantity of experimental or numerical results are available from the literature for a comparison with the schlieren experiments;

(ii) the tests on smooth channels enable a comparison to be made between ribbed and unribbed channels.

Unlike the forced convection experiments, no wind tunnel was required to convey the air flow to the test section, as the buoyancy forces are responsible for driving the fluid within the channels. However, the channels were confined on four sides by glass walls having open grids at the bottom (see Fig.4.2). Runs conducted without the side walls revealed negligible effects on heat transfer performance, but their presence was deemed necessary to minimise extraneous air-current effects that might disturb the optical measurements.

4.1.2 The instrumentation

The experiments were carried out in a large isolated room with all instrumentation (scanning thermometer, barometer, voltmeters, and ammeters) as well as the power supply system set far away from the test section.

Both the aluminium plate assembly and its surroundings, comprising the adiabatic plates and ambient air, were instrumented with fine-gauge, chromel-alumel thermocouples, calibrated to ±0.1 K. Up to 30 thermocouples were embedded in the wall of each plate at different locations through 0.5-mm-dia holes drilled into the rear surfaces of the two coupled aluminium plates, as shown in Figs.4.3 and 4.4. Care was taken to drill the holes as close to the exposed surfaces as possible. The adiabatic walls were instrumented by three thermocouples, placed at different elevations between the plastic cover and the perspex through small holes drilled in the material, while the ambient air temperature was measured by five

shielded thermocouples situated just below the channels (Fig.4.3). All thermocouple signals were read by a Keithley multi-channel digital thermometer, with automatic compensation to yield temperatures in ^{o}C directly.

The power input was dissipated into the aluminium plates by delivering to the resistors known amounts of electrical currents from three separate DC power supplies, accurately controlled by independent voltage and current measurements. The power supplied to the plate assembly was transferred to the surroundings mainly by natural convection. Since the thermal resistance of the plate material was very small, owing to the high thermal conductivity of aluminium, the heated plate assembly was expected to be virtually isothermal. Owing to the low thermal resistance of the material, the three independent heaters required the same electrical current to provide surface-temperature uniformity. This was checked by the thermocouples embedded in the wall. The maximum variations in temperature over the heated plate assembly turned out to be about 2 percent of the mean plate-to-ambient temperature difference. Hence, the plate (whether ribbed or flat) assembly was assumed to attain a uniform temperature, the value of which depended on the characteristics of the buoyancy-induced flow and on the amount of heating power transferred to the surroundings.

As previously noted, all of the heating power supplied to the aluminium plate assembly was dissipated at its exposed surfaces mainly by natural convection. The radiant contribution was expected to be small owing to the low emittance of aluminium and the high reflectance of the opposite walls. In fact, the radiation heat transfer was estimated to be less than 10-15 percent of the total power input by using the net-radiation method for enclosures of diffuse-gray surfaces. It has been subtracted from the total heat transfer (given by the overall electrical power supplied to the heaters), thereby yielding the overall natural convection heat transfer rate.

4.1.3 The optical system

A schlieren optical system was employed to reconstruct the thermal field and to perform measurements of local heat transfer coefficients. The schlieren system is schematically shown in Fig.4.5 (a). A non-coherent light beam from a vertical slit source, collimated by the concave mirror M_1 (38 cm. diameter) passes through the test section. A second concave mirror M_2 (38 cm. diameter) is then used to form a real image of the slit source

in the focal plane and a real image of the test section onto a screen or camera. Owing to the inhomogeneities of the fluid refractive index around the plates, the light rays undergo angular deflections. Regions of the optical field that have the same light deflection can be identified by shifting an opaque vertical filament in the focal plane of mirror M_2, as shown in Fig.4.5 (b). When a disturbed light ray is stopped by the focal filament, the image of the corresponding region of fluid will appear dark on the screen, while the remaining field will be bright. The deviation of a disturbed ray in the focal plane of mirror M_2 can be recorded by measuring the distance between the middle of the undisturbed image of the slit source and the centreline of the filament, i.e. the distance between the filament positions 1 and 2 displayed in Fig.4.5 (b). If the thermal field is assumed to be two-dimensional (i.e. temperature is independent of z-coordinate) the shift Δ_y of each light ray (due to the deflection in the y-z plane) can be related to the local temperature gradient by the relationship:

$$\Delta_y = \Omega \cdot (\partial T/\partial y)/T^2 \qquad (4.1)$$

where T=T(x,y) is the absolute temperature, y is the direction in which the light deflection is recorded and Ω is a constant depending on the fluid, the pressure, the plate length and geometric parameters of the optical components. In the present experiment, Ω was equal to -0.0456 m^2K. The temperature reconstruction procedure is based on a set of photographs (for each experimental run) obtained with the focal filament placed at different distances Δ_y from the undisturbed slit-source image. A typical example of a photograph taken by the schlieren apparatus is reported in Fig.4.6. By identifying for each photograph the coordinates of the centreline of the filament shadow, it is possible to obtain the profile of lines of constant light-deviation values Δ_y and thus, taking into account Eq.(4.1), reconstruct the temperature distribution in the entire optical field. The knowledge of lines at equal Δ_y in the optical field is sufficient to reconstruct the distribution of the function T(x,y). Despite this, it could be useful, especially for evaluating the heat transfer coefficients around the ribs, to record the pattern of lines at equal Δ_x, i.e. the locus of points giving rise to the same light deflection along the x-direction, in the plane x-z. This was made possible by mounting the slit source as well as the focal filament onto supports able to rotate by an angle of up to 90 degrees. The arrangement of both slit source and focal filament in the horizontal direction enabled Δ_x deviations to be determined and temperature

gradients along x to be derived according to the relationship:

$$\Delta_x = \Omega \cdot (\partial T/\partial x)/T^2 \qquad (4.2)$$

An alternative series of schlieren images have been recorded by using the colour-image system. This method implies the use of a coloured filter (thin transparent coloured strips) placed in the focal plane of the schlieren head (mirror M_2) in lieu of the focal filament. No displacement of the filter is required. The strips have to be used with a slit source, which must be in the vertical position if horizontal temperature gradients are to be detected. Temperature inhomogeneities in the test section cause the deflected rays to pass through different coloured strips of the filter. Therefore, the image of all the points which deflect the light beam through the same angle has the same colour. This method has the advantage of enabling a whole-field image of the phenomenon to be obtained without the need of superimposing a number of images, as occurs with the focal filament method. Unfortunately, the measurement range is limited by the small number of coloured strips that can be mounted on the same filter (usually less than 10, for the present experiment). Therefore, the images obtained by the colour method have been presented only for qualitative purposes, for instance for the comparison between the smooth channel case and the rough channel case. The filter used for the colour schlieren images is sketched in Fig.4.7. Under working conditions, the image of the slit source has been collimated on the central strip (light blue) in order to assign this conventional colour to the regions of the test section characterised by negligible light deviation. This condition means the regions are at the same temperature as the ambient air. Adjacent colours, from the centre to the end side of the filter, correspond to progressively increasing light angular deflections, that is, thermal gradients in the test section. The colour pattern is symmetrical owing to the symmetry of the test sections employed.

The working principles of the colour method are concisely demonstrated in Fig.4.8. Five light rays pass through the test section at different y-coordinates 0-1-2-3-4 (Fig. 4.8 a); owing to the temperature gradients in the test region they are deflected by different amounts (Fig. 4.8 b) and impinge against the coloured filter (held at the focus of mirror M_2) at different positions 0-1-2-3-4 (Fig.4.8 c). Therefore, the image of the test section (projected onto the camera) is artificially coloured (Fig.4.8 d).

The light deviation associated with each colour is proportional to the distance between the centreline of the coloured strip and the centreline of the central (reference) strip, measured on the filter.

4.1.4 The data processing system

The local heat transfer coefficient can be directly obtained from schlieren images without having to reconstruct the whole thermal field. Indeed, if the focal filament is moved until its shadow intersects the surface profile (in the image projected on the camera), the displacement of the filament corresponds to the deviation Δ_w of the light ray passing in the vicinity of the surface at the desired location. The relation between light deviation Δ_w and the local heat transfer coefficient is derived in Appendix A2. While performing the local measurement of Δ_w at the surface, the slit-source and focal filament must be aligned to the surface profile. This alignment must be in the vertical or the horizontal direction when heat transfer coefficients along either vertical or horizontal surfaces have to be measured.

The local heat transfer coefficient then may be estimated by direct measurement and without the need to process the image. This facility makes the method very powerful. On the other hand, since the function T(x,y) can not be explicitly obtained from Eq.4.1, the temperature reconstruction requires the processing of a series of images recorded, for a given experiment,with the focal filament in different positions. From the superposition of these images, the pattern of lines at equal light deviation is obtained and then, using Eqs. (4.1) and (4.2), the thermal field is reconstructed. The required steps for data processing, as well as the mathematical treatment of optical data, are explained in Appendix A2.

4.2 The geometry

As stated in Paragraph 4.1.1, two different test sections were considered. Firstly, free convection from **smooth** vertical channels having one wall heated (**at uniform surface temperature**) and the opposite wall thermally insulated has been considered. This configuration is depicted in Fig. 4.9: the input power dissipated into the heaters is symmetrically transferred to the upward moving fluid. The dimensions of the heated plate assembly were: overall thickness t=12 mm, height H=17.5 cm, and length L=30 cm. The length was chosen to be much greater than the other dimensions in

order to favour a two-dimensional thermal field in the channels.

The main body of experiments involved the use of **rib-roughened** vertical channels having the rough wall heated (**at uniform surface temperature**) and the opposite (smooth) wall thermally insulated (Fig.4.10). Again, the symmetry of the configuration led to an equal subdivision of the power input to the adjacent channels. The rough plate assembly has the following dimensions: overall thickness t=12 mm, height H=17.5 cm, and length L=30 cm. The wall sides exposed to the ambient air were roughened by square ribs having the height e equal to 4.85 mm and a pitch-to-height ratio P/e=7.2. This geometry was as in forced convection experiments, and resulted in each wall side containing 5 ribs identically sized and spaced.

For both smooth and rough wall configurations, different values of the channel spacing S were chosen in the course of the experiments. Conversely, the wall-to-fluid temperature difference was kept constant and equal to about 45 K, in order to perform all the experiments at the same Rayleigh number (based on the overall height H of the channel).

4.3 Operating procedure

Experimental runs were performed according to the following procedure:
i) arrangement of the channel aspect ratio, by setting the value of the interplate spacing S equal on both sides. For this purpose, calibrated spacers were used;
ii) heating of the aluminium plates by given amounts of electrical power into the heaters in order to attain, for steady state conditions, a temperature surface uniformity;
iii) in the steady state, measurements of wall and ambient air temperatures and reconstruction of the thermal field from a set of schlieren photographs (from 10 to 20 for each run);
iv) optical measurement of the light deflections near the vertical and horizontal walls in order to obtain the local heat transfer coefficients at several locations.

4.4 Results and discussion

Each experiment was performed by adjusting the input power in order to

attain a prescribed temperature difference between the heated walls and the ambient air. Therefore, a significant input parameter is expressed by the Rayleigh number, based on the wall-to-fluid temperature difference and introduced in Appendix A2. Since the geometric dimensions of the channels were not fixed, additional input parameters are given by the aspect ratio (spacing-to-height ratio) of the channel and by the rib-height to channel-spacing ratio. The rib pitch-to-height ratio was held fixed and equal to 7.2. The measured quantities are expressed in terms of a convenient dimensionless temperature and of the Nusselt number, as explained in Appendix A2. The dimensionless temperature is particularly suitable to present the temperature profiles of the fluid in the channel while the Nusselt number, obtained on a local basis from schlieren visualisations and on an overall basis from the energy balance, is related to the efficiency of heat transfer from the wall to the fluid.

Temperature and heat transfer results will be presented in the following sequence:

a) smooth channel configuration;

b) rib-roughened channel configuration.

For both cases comparisons of experimental results with data reported in the literature will be also presented and discussed.

4.4.1 The smooth channel

A first set of experiments was conducted for vertical channels formed by flat plates (Fig.4.9). The aspect ratio S/H was varied over the range 0.05-0.4. In all cases the wall-to-fluid temperature difference was held constant and equal to 45 K, giving a Rayleigh number Ra equal to $1.8 \cdot 10^7$.

Preliminary tests showed that the degree of uniformity in surface temperature attained by the heated plate assembly, recorded by 13 thermocouples deployed in different positions, was satisfactory. In fact, for the ambient air temperature of 20 °C, the surface temperature in the measured location deviated by ±1 K at most from the mean value (65°C). That is, a maximum surface temperature nonuniformity, relative to the mean wall-to-fluid temperature difference, of ± 2% was recorded. Several repeated tests showed a repeatability in local heat transfer coefficients within ±3.5 % and in overall heat transfer coefficients within ±1% (heat balance) and ±2.5% (schlieren visualisation).

Schlieren images obtained by the colour method are presented in Figs. 4.11-4.13. Figures 4.11 and 4.12 refer to images recorded with the colour

filter mounted vertically, in order to visualise, with different colours, regions of fluid in the channel characterised by non-negligible temperature gradients in the horizontal direction. Five values of the aspect ratio have been considered, namely S/H=0.4 (Fig. 4.11 a), 0.3 (Fig.4.11 b), 0.2 (Fig.4.12 a), 0.1 (Fig.4.12 b), and 0.05 (Fig.4.12 c). Images were recorded under steady state conditions, for the Rayleigh number $Ra=1.8\cdot10^{7}$. For these conditions, no disturbances in the colour contours were noticed. This means that the flow was laminar in all cases. As is apparent from the figures, the colour pattern is symmetrical, owing to the symmetry of the geometry (two adjacent channels heated on one side and adiabatic on the opposite side) and of the filter (illustrated in Fig.4.7). When the aspect ratio is high (S/H=0.4, Fig.4.11a), a large part of the fluid flowing in the channels appears light blue, which is the colour associated with zero or negligible thermal gradients. This situation is typical of the single, vertical, heated plate, since the opposite adiabatic plate does not seem to affect the thermal field. The progression in colours from outside the thermal boundary layer to the heated wall indicates strong temperature gradients at the leading edge of the heated plate, where the heat transfer is more effective. Despite the low thermal emittance of the heated walls, a small heat exchange by radiation between opposite walls occurs. This radiant heat flow is responsible for a slight increase, relative to ambient, of surface temperature on the unheated side of the channels. This fact is confirmed by the thin "yellow" portion of fluid close to the unheated walls opposite to the heated plate assembly as well as by local surface temperature measurements.

As the aspect ratio is reduced, the unheated wall gradually begins to influence the heat transfer mechanism from the heated plate to the fluid. At the minimum interplate distance (S/H=0.05, Fig.4.12 c), the thickness of the boundary layer, growing from the leading to the trailing edge of the heated plate, rapidly reaches the opposite plate, whose surface temperature dramatically increases. Despite the thermal insulation, a small amount of heat is transferred across the unheated plates and is convected to the ambient air at the opposite face.

Figure 4.13 shows images recorded with the colour filter mounted horizontally. For such conditions, the colours refer to the regions of fluid in the channel with non-negligible temperature gradients in the vertical direction. Schlieren images are displayed only for two S/H values:

0.3 (Fig.4.13 a) and 0.05 (Fig.4.13 b). As expected, non-zero vertical gradients in temperature occur only in the vicinity of the leading and trailing edges of the heated plate. They are due to the presence of the horizontal boundaries of the heated plate and to conductive effects in the fluid close to the inlet of the channel. The "yellow" region appears to be wider in the narrower channel.

The reconstruction of the fluid temperature profiles required, for each test, a set of schlieren photographs obtained by the focal filament method. For instance, images obtained for S/H=0.3 and $Ra=1.8\cdot10^7$ are reported in Fig.4.14, for various positions of the focal filament, displaced vertically and progressively moved from $\Delta_y=0$ mm (reference position) to $\Delta_y=4.9$ mm. From the schlieren images, the centrelines of the filament shadows (lines at equal deviation of light) were extracted. The contours of lines deflecting the light by the same amount are reported in Figs.4.15 and 4.16 for $Ra=1.8\cdot10^7$. The aspect ratio values are S/H=0.4 (Fig. 4.15 a), 0.3 (Fig. 4.15 b), 0.2 (Fig. 4.16 a), 0.1 (Fig. 4.16 b), and 0.05 (Fig. 4.16 c). Owing to the symmetric configuration of the test section, results are reported only for one of the two identical adjacent channels. The processing of the iso-deflection lines enabled the fluid temperature distribution to be obtained for each experiment. The profiles of the dimensionless temperature θ as a function of the normalised coordinates y/S and x/H are reported in Fig.4.17, for the whole range of S/H values explored. When the S/H value is high (0.4), the temperature of the fluid approaches the external air temperature at relatively small distances from the heated wall. At the lowest S/H value (0.05), large increases in fluid temperature are shown. The heating condition imposed at the right surface clearly affects the temperature values at the opposite left surface. Here θ exceeds 0.4 close to the exit of the channel.

In Fig. 4.18 temperature data are recast according to a different format of presentation: θ is expressed as a function of a dimensionless variable $\eta=(y/x)(Ra_x)^{1/4}$, where $Ra_x=\beta g x^3(T_w-T_{air})Pr/\nu^2$ is the Rayleigh number based on the local elevation x. The continuous line represents the theoretical solution obtained by Ostrach (1953) for free convection from a vertical, single, isothermal plate. It appears from the figure that the majority of experimental temperature data for S/H between 0.1 and 0.4 are in good agreement with Ostrach's results: this demonstrates the negligible role played by the opposite adiabatic plate for the above-mentioned range

of the aspect ratio. It should be noted that points obtained close to the leading edge (symbols with the downward leg) do not agree too well with the theory. In fact, the boundary layer assumption made in the theoretical development implies that the distance along the plate is large when compared with the boundary layer thickness. This assumption is obviously invalid near the leading edge. For the lowest aspect ratio (S/H = 0.05), the departure of experimental data from the single plate solution is evident: here, the thermal interaction between the facing plates is marked.

For the lowest aspect ratios, experimental temperature results can be compared with those predicted by numerical simulations obtained for natural convection in asymmetrical heated channels. A numerical study of this problem has been conducted by the present author some years ago (Tanda, 1987 and 1988). The two-dimensional field equations for laminar, incompressible, boundary layer flow were discretised by finite-difference equations and solved by the "marching procedure" method. Such a procedure requires that the pressure, the temperature and the velocity fields be given as input data at the channel inlet section. Since the inlet velocity is unknown in a free convection problem, it is treated as a computational parameter. That is, a value of the inlet velocity is given and the computation, beginning at the inlet section, proceeds upward until the pressure becomes equal to the ambient pressure. At the corresponding elevation the computation is terminated and the channel exit section is found *a posteriori*. Figure 4.19 presents the comparison of experimental results with those predicted numerically for S/H=0.1 (a) and S/H=0.05 (b). The corresponding modified Rayleigh numbers are 1800 and 160, respectively. It should be noted that for larger S/H values and a wall-to-fluid temperature difference of 45 K, the modified Rayleigh number exceeds the critical value (about 2000) for which flow reversals, situated adjacent to the unheated wall in the upper part of the channel, occur (Sparrow et al., 1984). For these conditions, the parabolic numerical scheme adopted is not compatible with the presence of recirculating flow and therefore numerical results were not obtained. For S/H=0.1 the comparison is in reasonable agreement far from the leading edge. In fact, the numerical solution neglects the streamwise second derivatives and tends to overpredict the temperature gradients at the wall close to the inlet section of the channel. For S/H=0.05 the disagreement persists over the bottom half of the channel. In fact, the region affected by non-zero vertical temperature

gradients develops along a relatively large portion of the channel, as appears from Fig. 4.13 (b). Moreover, the experimentally reconstructed temperatures become increasingly higher than the predicted results as the unheated (passive) wall is approached. This phenomenon, also observed by other experimentalists (Webb and Hill, 1989) in similar conditions, could be the result of minor radiation heat transfer to the passive wall from the heated wall. The variation of thermophysical properties (not included in the predictions) could also introduce additional discrepancies between measured and computed data.

Local heat transfer results are reported in Figs.4.20 and 4.21. In particular, Fig. 4.20 shows the local heat transfer coefficients, evaluated by the schlieren focal filament method, plotted against the local elevation x, for all the aspect ratio values, while in Fig.4.21 local heat transfer characteristics are presented in dimensionless form, through the local Nusselt number Nu_x and the local Rayleigh number Ra_x. For each S/H value, the local heat transfer coefficient has been estimated by an average between values recorded, at the same elevation, at the left and right sides of the heated plate assembly. As is evident from inspection of the figures, there are only small differences between the heat transfer coefficients obtained for S/H between 0.1 and 0.4. Entrance effects are responsible for the larger heat transfer coefficients at the leading edge as S/H is progressively reduced. For the lowest aspect ratio investigated (S/H=0.05), the heat transfer coefficient distribution starts from a very high value, due to the acceleration of inlet flow provoked by the reduced passage area, and then sharply decreases as the axial coordinate is increased.

Figures 4.22 and 4.23 refer to the overall heat transfer characteristics. As explained in Appendix A2, the overall heat transfer coefficient of the heated plate can be obtained in two different ways:
(a) by evaluating, from the energy balance, the overall convective heat transfer from the wall to the fluid (h_{av});
(b) by numerically integrating the local heat transfer coefficients given by the schlieren experiments over the heat transfer area (h_o).
Firstly, h_{av} and h_o are plotted as a function of the aspect ratio S/H (Fig.4.22). Data obtained by the two different procedures are in excellent agreement (within ±4%). From both the energy balance and the optical measurements the aspect ratio, for the range explored here, is found to

slightly affect the overall heat transfer coefficient. In the range of S/H from 0.4 to 0.2, the heat transfer effectiveness is constant. For S/H=0.1, the heat transfer coefficient has a maximum value. This is due to the entrance effect (acceleration of flow at the inlet section) that provokes an increase of heat transfer efficiency close to the leading edge. Further reductions in S/H lead to larger enhancements at the leading edge, but the boundary layer is likely to interact with the opposite plate; as a result, the overall heat transfer coefficient decreases. The dimensionless overall results are plotted in Fig.4.23, where the modified Nusselt numbers (obtained both from the heat balance and the optical data) are reported versus the modified Rayleigh number and compared with data from the literature. Symbols refer to experiments while solid,dashed and dotted lines represent the composite equation of Bar-Cohen and Rohsenow (1984), the semiempirical relationship of Sparrow et al. (1985) and the numerical results of Tanda (1987), respectively. The experimental results presented here are successfully correlated by the Bar-Cohen and Rohsenow formula, with deviations within ±4%.

4.4.2 The rib-roughened channel

The majority of experiments were conducted in the presence of the ribbed channel configuration, depicted in Fig.4.10. The input parameters were again the Rayleigh number and the aspect ratio of the channel, ranging from 0.05 to 0.4. A further geometrical parameter, the rib pitch-to-height ratio P/e was held fixed (P/e=7.2). For the purpose of comparison with the smooth channel case, the majority of tests were performed under a constant wall-to-fluid temperature difference of 45 K. This gave a Rayleigh number equal to $1.8 \cdot 10^7$. Additional runs were conducted at wall-to-fluid temperature differences in the range 10-45 K.

Owing to the particular geometry adopted, the degree of uniformity in surface temperature was checked by a large number of thermocouples, deployed along the symmetry line of the heated plate as well as laterally. Again, the surface temperature readings were uniform within ±2% of the mean wall-to-fluid temperature difference. The repeatability in overall heat transfer coefficients was within ±1% for the heat balance evaluation and within ±2.5% for the integration of the local optical measurements.

Schlieren images obtained by the colour method are presented in Figs. 4.24-4.26, with the colour filter displaced either in the vertical or in the horizontal position. The perfect steadiness of colour pattern

demonstrated that the flow regime was laminar. First, attention is focused on light deflections occurring along the y-direction. Results are presented for S/H=0.4 (Fig.4.24 a), 0.3 (Fig.4.24 b), 0.2 (Fig.4.25 a), 0.1 (Fig.4.25 b) and 0.05 (Fig.4.25 c). The Rayleigh number was $1.8 \cdot 10^7$. Owing to the presence of ribs, the contour of the coloured region is wavy, except for the image recorded for S/H=0.05 (Fig.4.25 c), where the line of separation between the coloured region and the undisturbed (light blue) region vanishes. In particular, the contour of each coloured line in the inter-rib region is arc-shaped, thus indicating a similitude between thermal fields upstream and downstream of each rib. From inspection of Fig.4.26 it is evident that significant temperature gradients in the vertical direction occur not only close to the leading and trailing edge of the channels but also around each rib. This is due to the presence of the horizontal rib walls that induce upward and downward heat fluxes to the fluid.

Typical schlieren images obtained by the focal filament method are reported in Figs. 4.27 and 4.28 for S/H=0.3 ($Ra=1.8 \cdot 10^7$). The focal filament, when displaced vertically (Fig.4.27), was progressively shifted from Δ_y=0 mm (reference position) to Δ_y=3.4 mm. When the filament was set horizontally (Fig.4.28), it was moved from Δ_x=-1.9 mm to Δ_x=0.9 mm, passing through the reference position Δ_x=0. The contours of the filament shadows are clearly much more complex than those for the smooth channel case. In addition, owing to the complexity of the geometry, both vertical and horizontal components of light deflection are required to evaluate in detail the heat transfer characteristics. Contours of lines deflecting the light by the same amount are plotted in Figs. 4.29-4.33 for $Ra=1.8 \cdot 10^7$ and, in sequence, for S/H=0.4, 0.3, 0.2, 0.1, and 0.05. For each experiment at a given aspect ratio, both curves at equal Δ_y and Δ_x are reported. In order to facilitate the understanding of each graph, different colours have been used to identify lines at equal deviation of light. The corresponding thermal fields have been successively reconstructed.

Temperature results are presented in Fig. 4.34 for S/H=0.4 (a) and 0.05 (b). The isotherm contours were extracted for the first module (space between the first and second rib) and for the last module (space between the fourth and the fifth rib) of the channels. In general, the isotherm plots clearly show the dead zones just upstream and downstream of each rib as well as the wall regions of high heat transfer performance, on the rib top and between the ribs, where a local reduction in the thermal boundary

layer occurs. It can be seen that in the case of a large aspect ratio (S/H=0.4, Fig. 4.34 a) the isotherms are packed close to the ribbed wall. For instance, the lowest isotherm line plotted, corresponding to θ=0.1, is at a distance from the ribbed wall which is between 10 and 15 percent of the channel spacing S, when the first (bottom) module is considered. The distance of the isotherm θ=0.1 from the ribbed wall slightly increases (between 17 and 22%) in the last (top) module, close to the channel exit. This means that a considerable part of the fluid driven upwards through the channel remains practically unheated. For the lowest aspect ratio (S/H=0.05, Fig. 4.34 b) the air flowing into the channel is strongly heated. Its dimensionless temperature θ always exceeds 0.3 in the first module and reaches θ=0.6-0.65 at the adiabatic wall close to the exit of the last module.

Attention is now turned to heat transfer coefficient distributions. Figures 4.35-4-39 show, in sequence, the local heat transfer coefficients along the wall profile for S/H=0.4, 0.3, 0.2, 0.1, and 0.05. As for the smooth channel case, each local heat transfer coefficient was evaluated by averaging the values recorded, at corresponding positions, for the two adjacent symmetrical channels.

The local heat transfer data in all of the figures display a common behaviour. In general, heat transfer coefficients start from high values at the leading edge and then sharply decrease, reaching a very low value (close to zero) upstream of the first rib owing to the reduction in flow velocity due to the obstruction. At the forward facing wall of the first rib an increasing h is apparent from the base to the tip of the rib. On the top of the first rib, the heat transfer coefficient is very high at the leading edge, then drops off towards the middle of the top of the rib and increases slightly as the downstream edge is approached. A strong decrease in heat transfer occurs along the rear facing wall of the rib. In fact, near the corner between this rib wall and the baseplate wall, the fluid is stagnant and the surface is practically adiabatic. In the space between the first and second ribs, the heat transfer coefficient has a progressive increase, reaches a peak value approximately at the inter-rib midpoint and then falls again to a very low value, at the corner between the base plate and the forward facing wall of the second rib. The variation in heat transfer coefficient between subsequent ribs is periodic in nature and the periodicity is equal to the rib pitch. Obviously, comparisons of h values

at points separated by a distance equal to the rib pitch exhibit a progressive reduction from the bottom to the top of the channel. This is due to the developing thermal field and to the definition of heat transfer coefficient here assumed, h being based on the temperature difference between the heated wall and the inlet (not bulk) fluid. It is interesting to note that the heat transfer distributions along the top of the ribs from the second to the fifth do not exhibit the slight increase towards the trailing edge recorded for the first rib, except for the S/H=0.05 case, where the shapes of the profiles are similar for all the ribs. The effect of the aspect ratio on local heat transfer characteristics can be deduced from Fig. 4.40, where h profiles for S/H= 0.4, 0.1, and 0.05 are directly compared. As observed for the smooth channel, the lowest aspect ratio (S/H=0.05) leads to heat transfer enhancement at the leading edge of the plate (here including the first rib top). Then h decreases to levels clearly lower than those recorded for the highest aspect ratio (S/H=0.4). The locations of the maxima in the inter-rib regions do not seem to be significantly affected by the aspect ratio of the channel. This indicates that the stagnant zone upstream and downstream of the rib is scarcely influenced by the channel aspect ratio, in the range of the S/H values studied.

Figure 4.41 shows the heat transfer coefficients averaged per module. The drawing close to the distributions of average heat transfer coefficients clearly shows the extent of each wall module (I, II, III and IV). As expected, module-averaged heat transfer coefficients gradually decay as the exit of the channel is approached. Only small differences occur among data obtained for S/H values from 0.4 to 0.1. Conversely, data recorded for S/H=0.05 are significantly lower, especially for the last wall modules.

The heat transfer coefficients normalised by the corresponding module-averaged values are presented in Fig.4.42. Only data recorded for the two extreme aspect ratios (S/H=0.05 and 0.4) are plotted. It appears from the figure that the profiles of normalised heat transfer coefficients repeat themselves almost identically after the second or third module. The positive role, from the heat transfer point of view, played by the rib top wall is greater for the smaller aspect ratio, especially in the first modules, owing to the acceleration induced in the relatively cool air flow. On the other hand, the heat transfer peak in the inter-rib region is more

pronounced when the aspect ratio is larger.

Overall heat transfer coefficients are shown in Fig.4.43. The overall values h_{av} and h_o obtained by two different procedures are presented. Heat balance and optical results show the same trends and differ from each other by within ±6 percent. The larger differences occur at the lowest S/H, where radiation induces effective errors (affecting h_{av}) and uncertainties in optical data (affecting h_o) are higher. It is apparent from the figure that there is an optimum aspect ratio which maximises heat transfer (S/H about 0.1). For larger aspect ratios (up to 0.4), the overall heat transfer coefficient slightly decreases (to about 5%) while passing from S/H=0.1 to 0.05 the extent of the reduction is higher (about 25%).

Overall heat transfer results for the rib-roughened channel are summarised in Fig. 4.44 and compared with those for the smooth channel. The presentation of data is performed on the basis of the modified Nusselt number against the modified Rayleigh number. The rough channel results plotted on the graph were obtained for S/H ranging from 0.05 to 0.4 and for wall-to-fluid differences from 10 to 45 K. The majority of data are well correlated by the relationship

$$Nu_m = 0.41 \cdot Ra_m^{0.25} \qquad (4.3)$$

It should be noted that for the lowest S/H values (or for the highest e/S values) the rough channel data do not fall on the same line. It means that the modified Rayleigh number does not properly express uniquely the effect of $(T_w - T_{air})$ and geometric parameters, as occurs for the smooth channel case. This suggests that Ra (based on H), S/H, and e/S (P/e being fixed) are likely to act as independent parameters. Therefore, the relationship (4.3) is valid in the following range of parameters:

$P/e = 7.2$;

$Ra_m \cong 2 \cdot 10^2 - 5 \cdot 10^5$;

$S/H \geq 0.075$

$e/S \leq 0.37$

$(T_w - T_{air}) \cong 10\text{-}45$ K.

In the whole ranges of parameters, rough channels results are always below the line fitting the smooth channel results.

Of particular interest is the comparison depicted in Fig.4.45. Here the ratio between Nu numbers pertaining to the rough and smooth channel $Nu_{av,r}/Nu_{av,s}$ is plotted as a function of the aspect ratio, the Rayleigh number being fixed ($Ra=1.8 \cdot 10^7$). In addition, the ratio C_r/C_s (between the

thermal conductances of the rough and smooth channel) is reported. The thermal conductance expresses the product of the overall heat transfer coefficient and the heat transfer area. Since the heights of rough and smooth channels are equal, adding the ribs leads to an increase in surface area that should be taken into account. As is evident from inspection of the figure, the comparison in terms of conductances is not so negative as that in terms of Nusselt numbers. Nevertheless, the increase in heat transfer surface area due to the ribs does not compensate for the decrease in heat transfer coefficient.

Finally, comparisons of the heat transfer results with those published in the literature have been performed. Firstly, local heat transfer coefficients are compared with those obtained by Bhavnani and Bergles (1990) using a Mach-Zehnder interferometer (Fig.4.46). The test section used by Bhavnani and Bergles was slightly different from that employed in this study. In fact the pitch-to-height ratio P/e was 8 (instead of 7.2), the ribbed wall was not faced by an adiabatic parallel wall and the ribs were press-fitted onto the baseplate and not integral with it. Moreover, the Rayleigh number corresponding to the heat transfer coefficient distribution was not given in the reference; only the range of the heated wall temperature (48-75 $^{\circ}$C) in the course of experiments was indicated. Despite the differences in the test conditions, there is good agreement between present data (with S/H=0.4) and those previously published. The shapes of heat transfer distributions are similar, this taking into account that only one value per rib (on the top wall) was recorded by Bhavnani and Bergles. The same Authors developed a relationship giving the heat flux Q as a function of the wall-to-fluid temperature difference ΔT and the height H of the heated plate. For P/e=8, 6 ribs, H=0.1778 m, they found $Q = 0.826\ H\ \Delta T$. On the basis of the description of the experimental runs provided by the Authors, the relationship should apply for ΔT about from 23 to 50 K. For the ΔT considered in this project (45 K), one obtains $Q/(HL) = 292.7$ W/m^2, where L is the test section length in the direction z, aligned to the direction of the light beam, and HxL is the heat transfer area projected on the x-z plane. Experiments conducted for S/H=0.4 gave $Q/(HL) = 258.6$ W/m^2, where Q is the heat flux derived from the energy balance (Eq.A2.16 in Appendix A2), H=0.175 m is the plate height and L is the overall length of the plate assembly in the z-direction (L=0.3 m x 2=0.6 m). The discrepancy between the two results is 12%, which is considered acceptable, taking into

account the experimental uncertainties associated to the experimental methods employed and the above-mentioned differences in the test geometries. Reductions in heat transfer coefficients, relative to the smooth plate, were around 23% (Bhavnani, Bergles) and 27% (Tanda, present project), respectively.

A further comparison of heat transfer results has been performed with measurements made by Acharya and Mehrotra (1993) for a channel formed by two facing rib-roughened plates, heated at constant wall temperature. The geometrical parameters were: P/e=4.8 and 9.6, H=0.1524 m, S/H=0.167, $Ra=3\cdot10^6-7.5\cdot10^6$. For both the pitch-to-height values, Acharya and Mehrotra found, by the calorimetric technique, reductions in heat transfer coefficients, with respect to the smooth channel case, of only 10-13%. It is believed that heat transfer coefficients introduced by these Authors are based on the baseplate surface area (HxW). In this case, the comparison has to be performed with the conductance ratio $C_{av,r}/C_{av,s}$, which turned out to be about 7-8% in the present experiments, for S/H = 0.1-0.2. The relationship between modified Nusselt and Rayleigh numbers found by Acharya and Mehrotra has the same exponent (0.25) as the equation obtained here. The coefficient (0.396) is only 3.5% lower than that found here (0.41), in spite of the different channel configuration (two facing ribbed and heated walls instead of one ribbed heated wall opposite to a smooth unheated wall). The excellent agreement demonstrates that for the Acharya-Mehrotra experiments (at S/H=0.167) the two boundary layers growing along the opposite ribbed walls do not significantly interact. Therefore, for aspect ratio larger than 0.167, the thermal behaviour of vertical channels with one or two ribbed walls is likely to be the same.

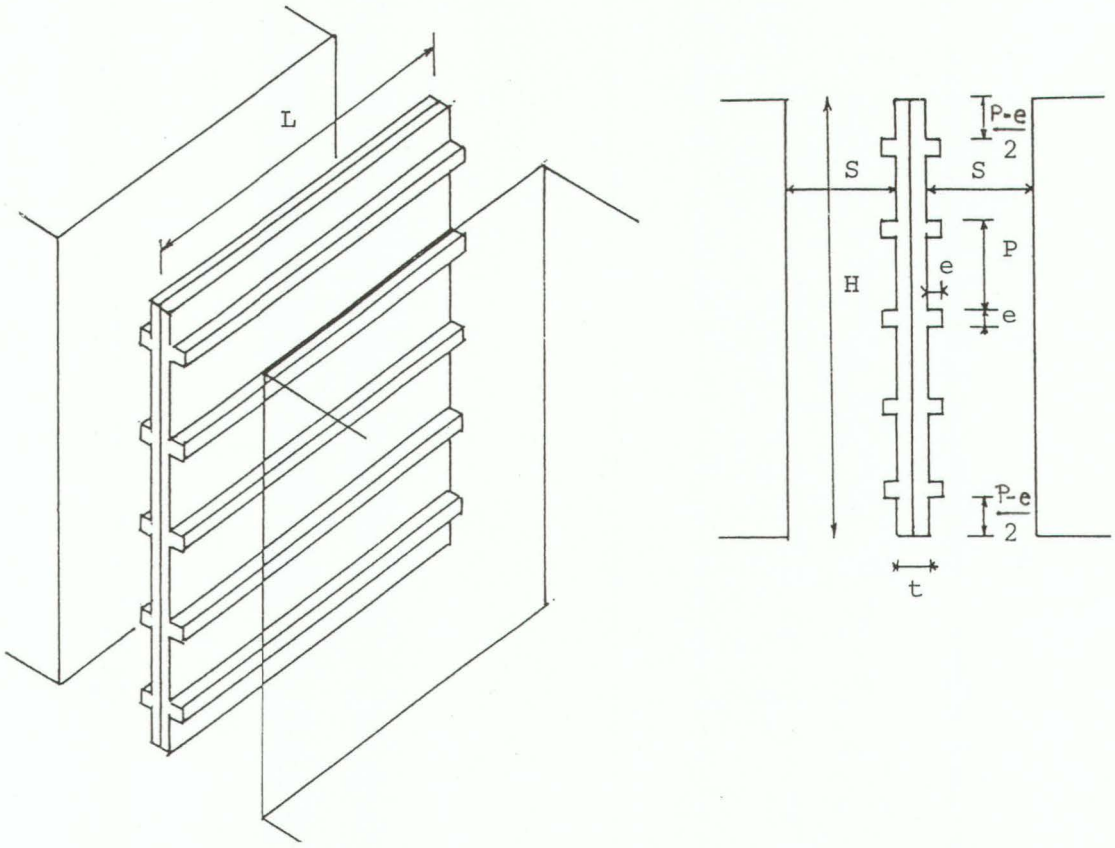

FIGURE 4.1 Schematic view of the test section.

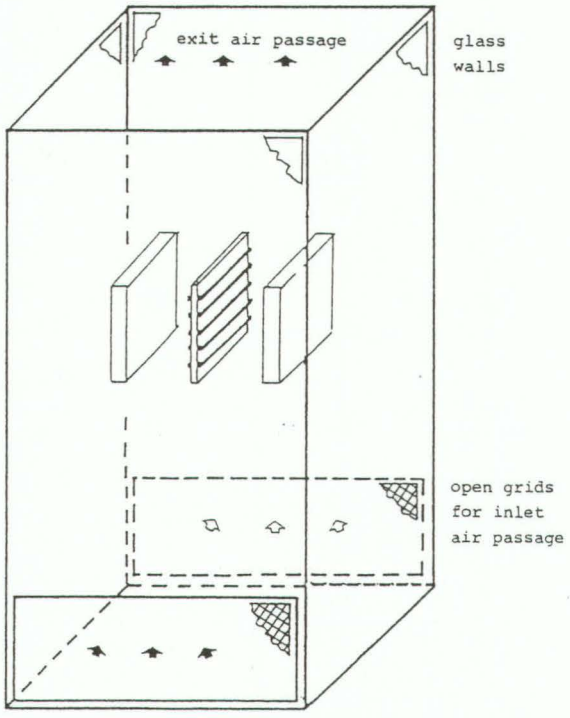

FIGURE 4.2 Detail of the shrouding of the channel and of the buoyancy air flow.

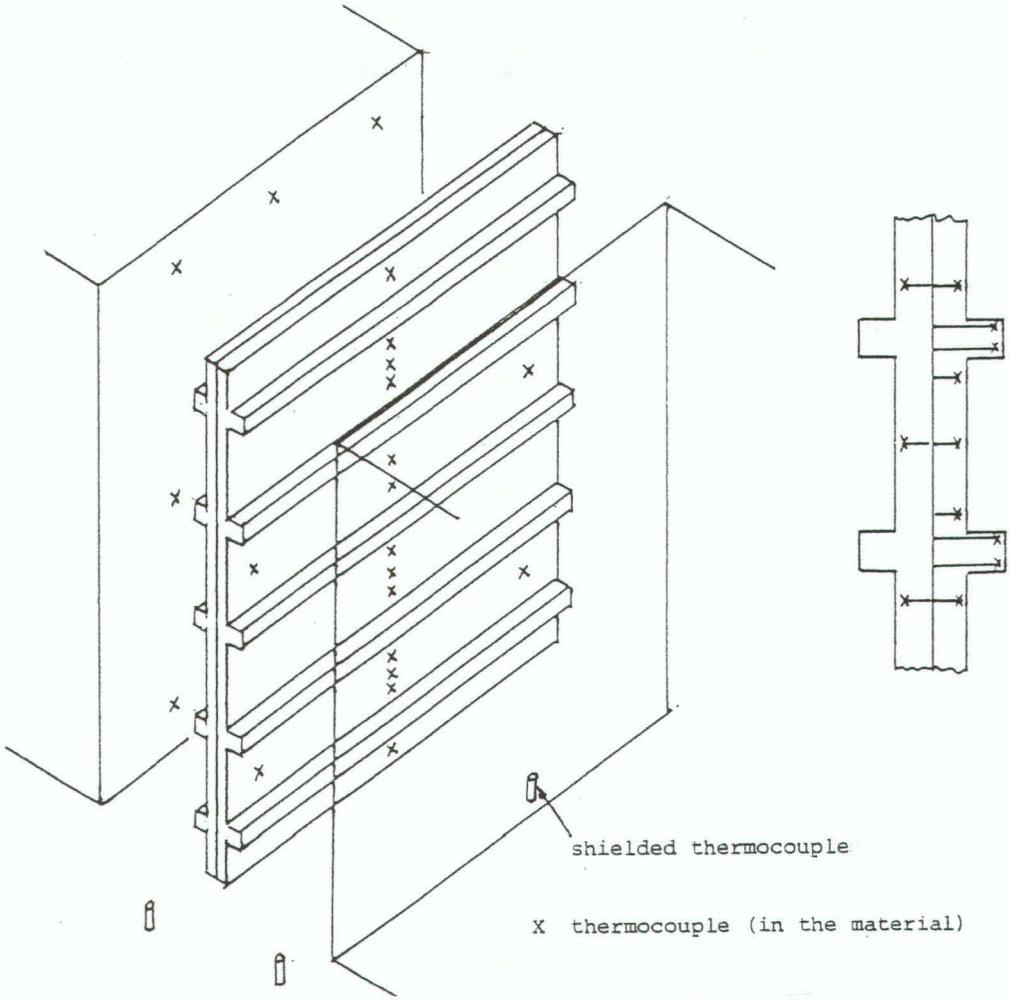

FIGURE 4.3 Positions of thermocouples for wall and air temperature measurements.

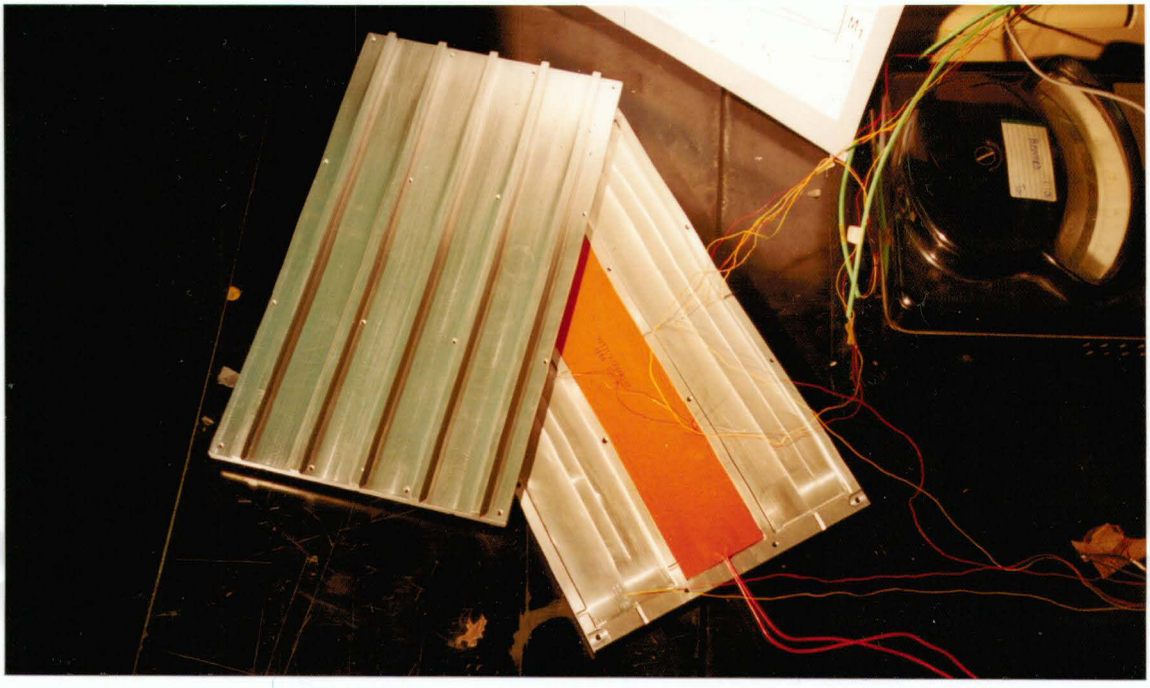

FIGURE 4.4 Photograph showing the detail of the housing of electrical heaters and thermocouples in the aluminium plates.

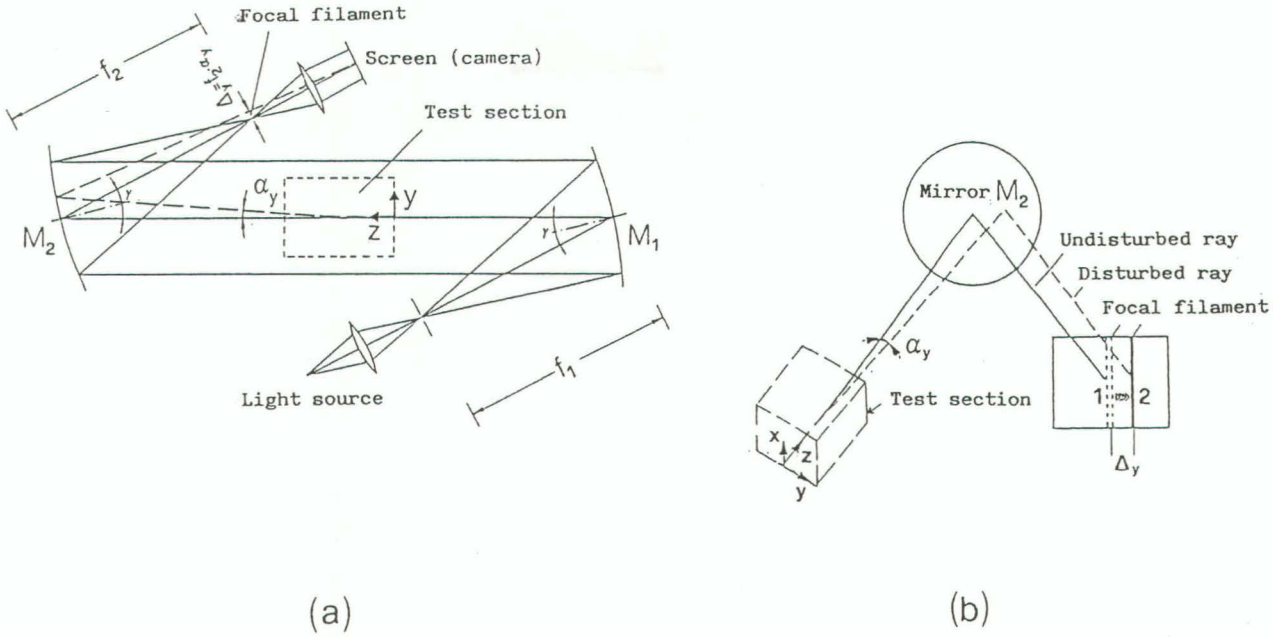

FIGURE 4.5 (a) Schlieren apparatus (top view): M1 and M2 are concave mirrors, with focal lengths f1 and f2, respectively (f1=f2=1.9 m, γ=9°, distance between mirrors about 8 m); (b) measurement of light deviation Δ_y at the focal plane of mirror M2: the focal filament is shifted from position 1 to position 2.

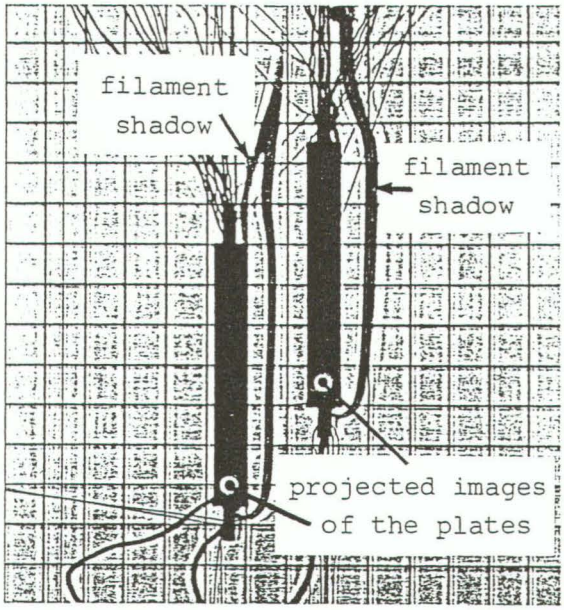

FIGURE 4.6 Schlieren image recorded for a two-staggered-plate assembly.

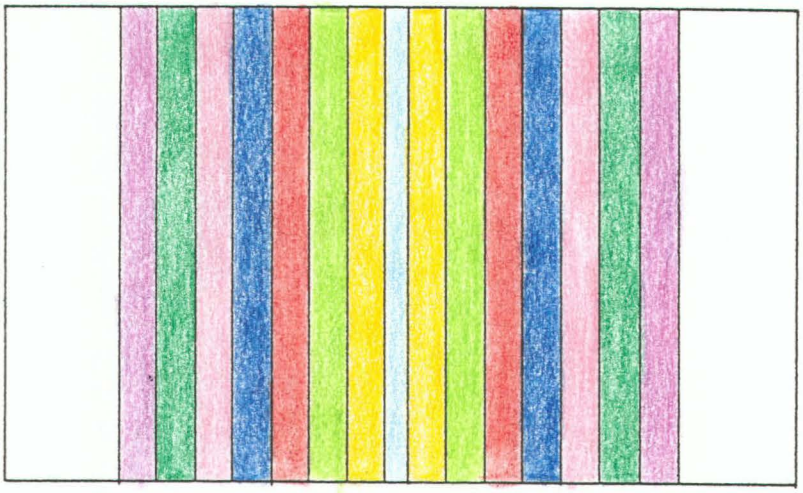

FIGURE 4.7 Coloured-strip filter

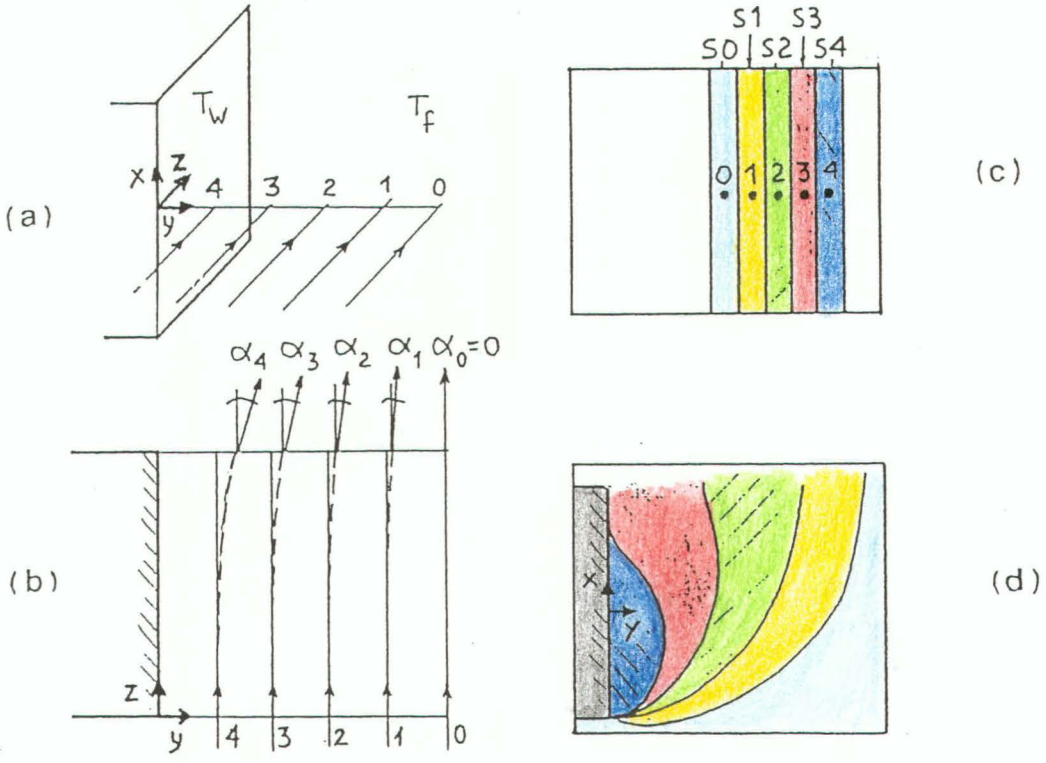

FIGURE 4.8 Colour schlieren method: (a) light beam entering the test section (a vertical heated wall), (b) angular deflections on the z-y plane, (c) positions of 0-1-2-3-4 rays at the focal plane where the colour filter is held, (d) colour schlieren image.

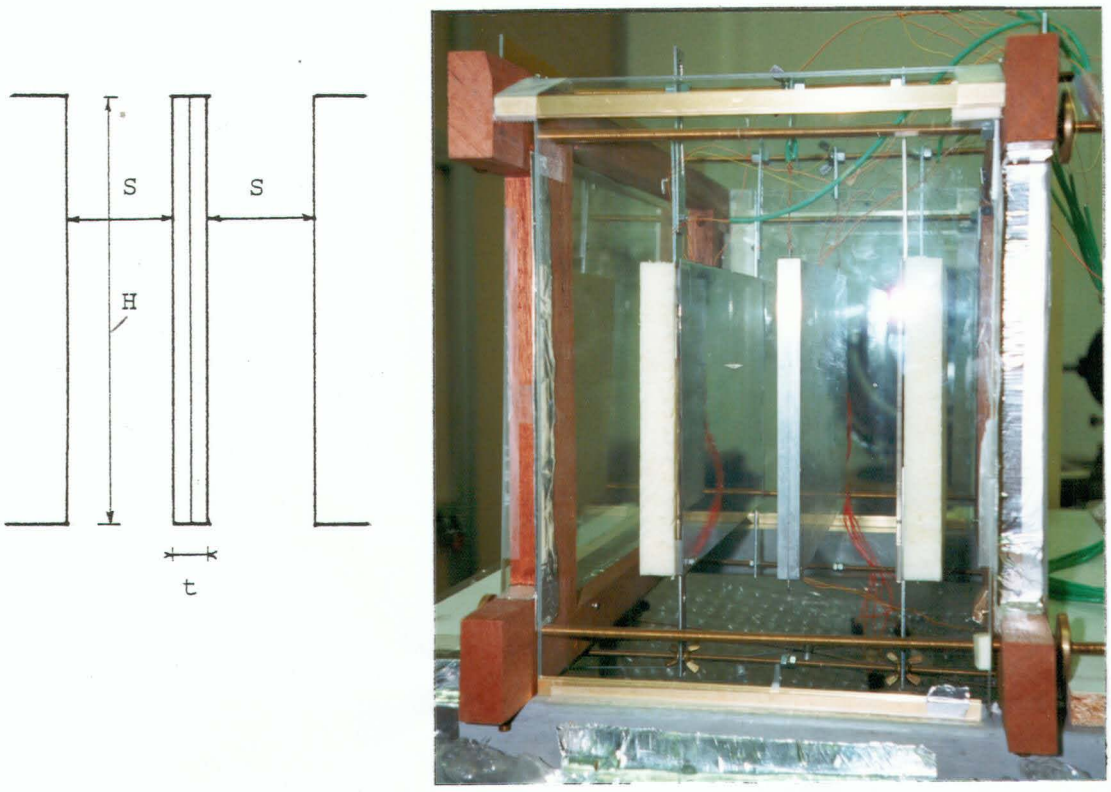

FIGURE 4.9 Sketch and photograph of the **smooth channel** configuration.

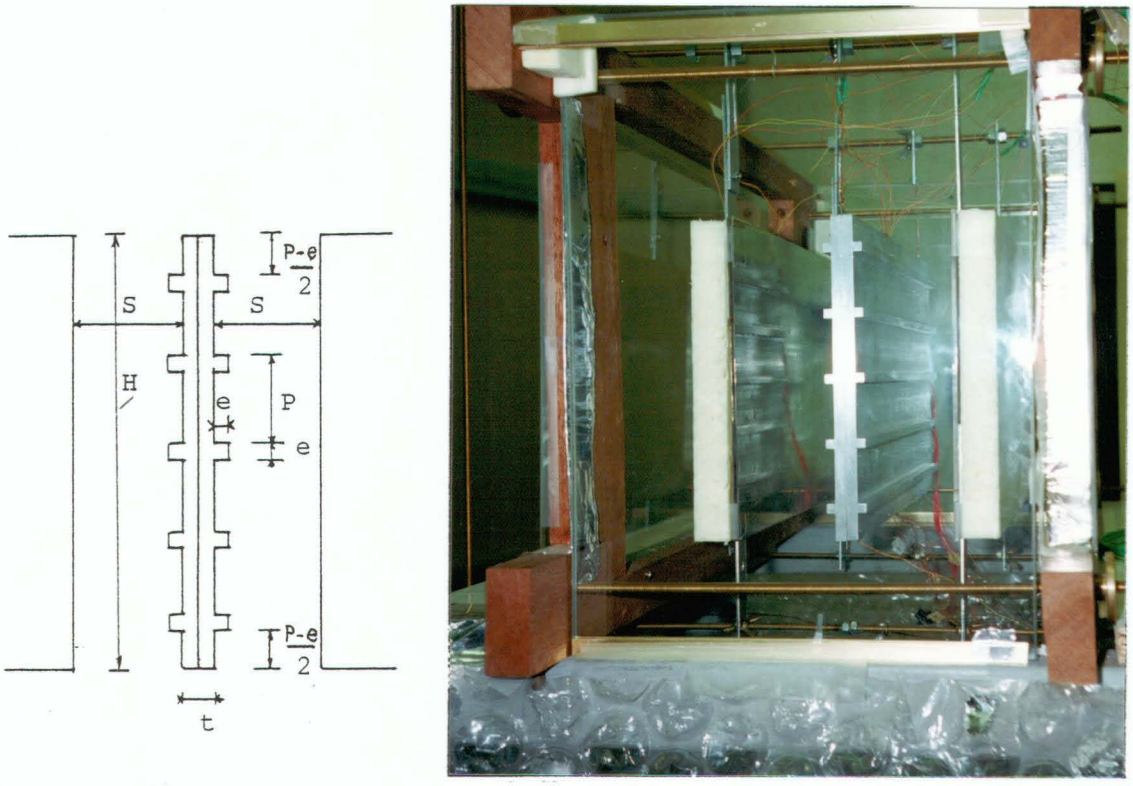

FIGURE 4.10 Sketch and photograph of the **rough channel** configuration.

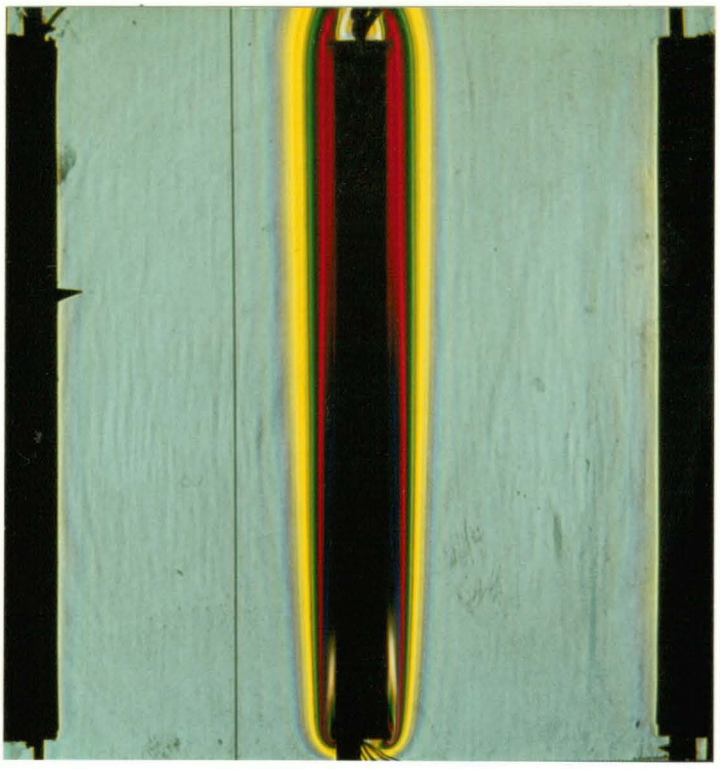

(a)

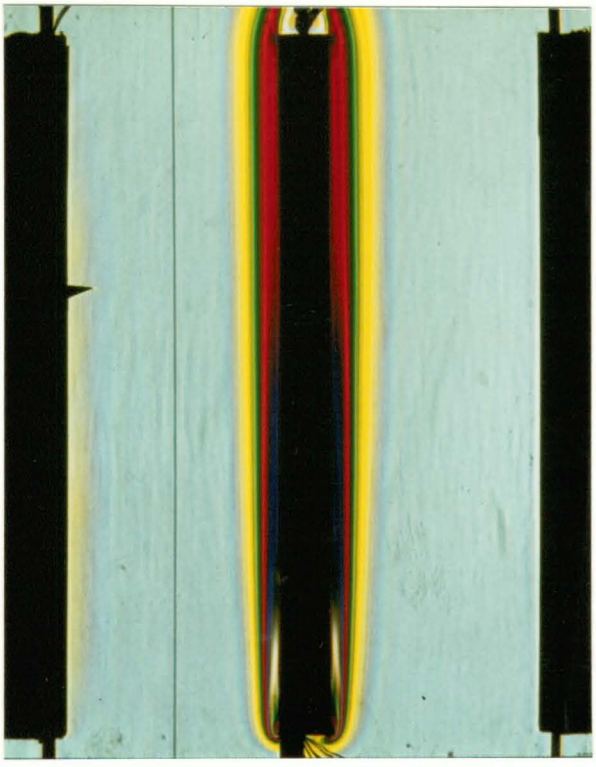

(b)

FIGURE 4.11 Colour schlieren images of the smooth channel assembly, filter mounted vertically, $Ra=1.8 \cdot 10^7$: (a) S/H=0.4, (b) S/H=0.3.

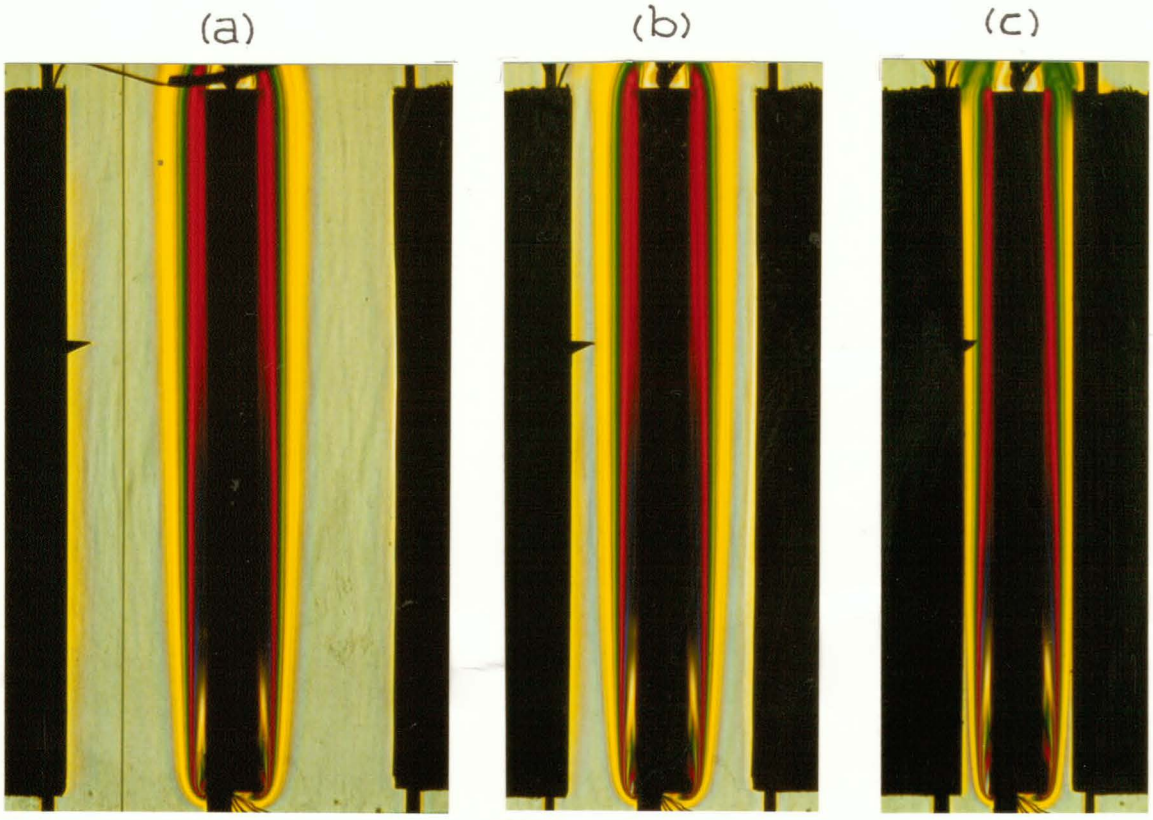

FIGURE 4.12 Colour schlieren images of the smooth channel assembly, filter mounted vertically, $Ra=1.8\cdot10^7$: (a) S/H=0.2, (b) S/H=0.1, (c) S/H=0.05.

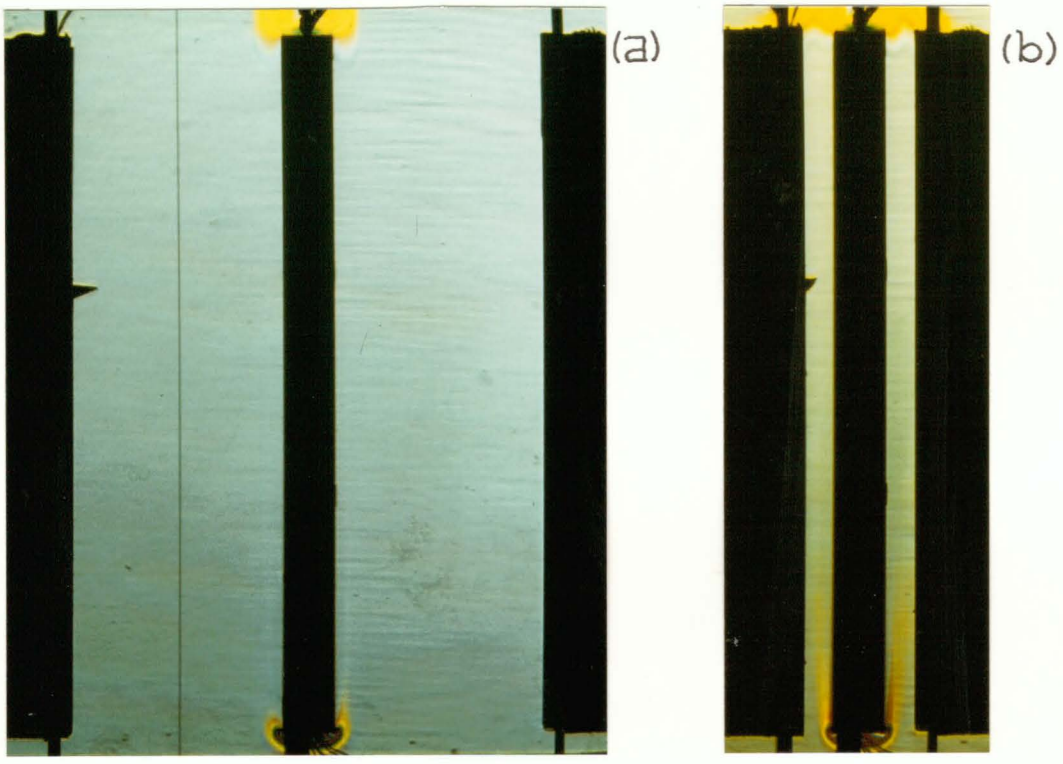

FIGURE 4.13 Colour schlieren images of the smooth channel assembly, filter mounted horizontally, $Ra=1.8\cdot10^7$: (a) S/H=0.3, (b) S/H= 0.05.

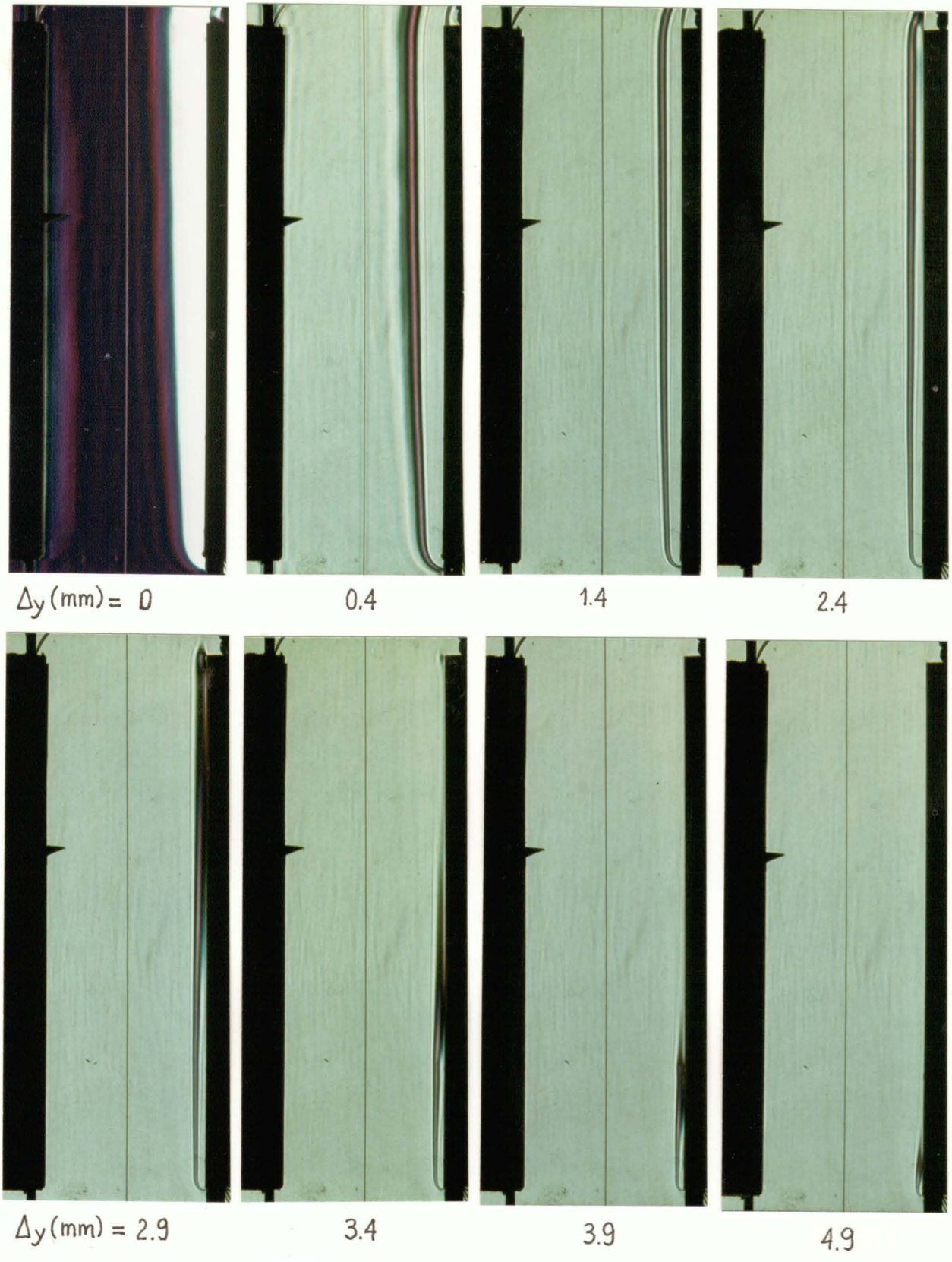

FIGURE 4.14 Schlieren images (focal filament method) of the smooth channel configuration, filter mounted vertically, $Ra=1.8 \cdot 10^7$, S/H=0.3. Δ_y from 0 (top left) to 4.9 mm (bottom right).

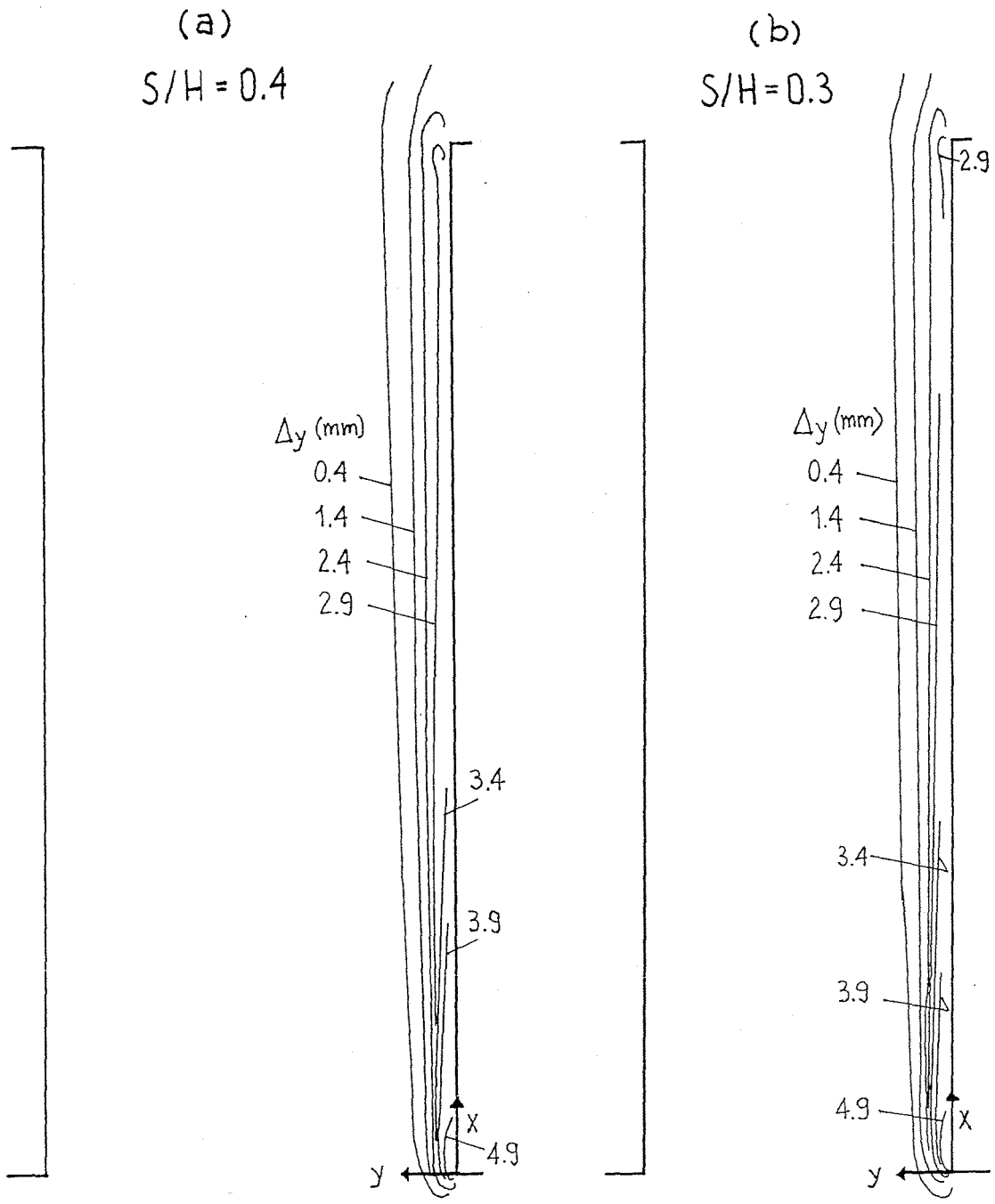

FIGURE 4.15 Lines of constant light-deviation Δy for the smooth channel configuration, $Ra=1.8 \cdot 10^7$. (a) S/H=0.4 , (b) S/H=0.3.

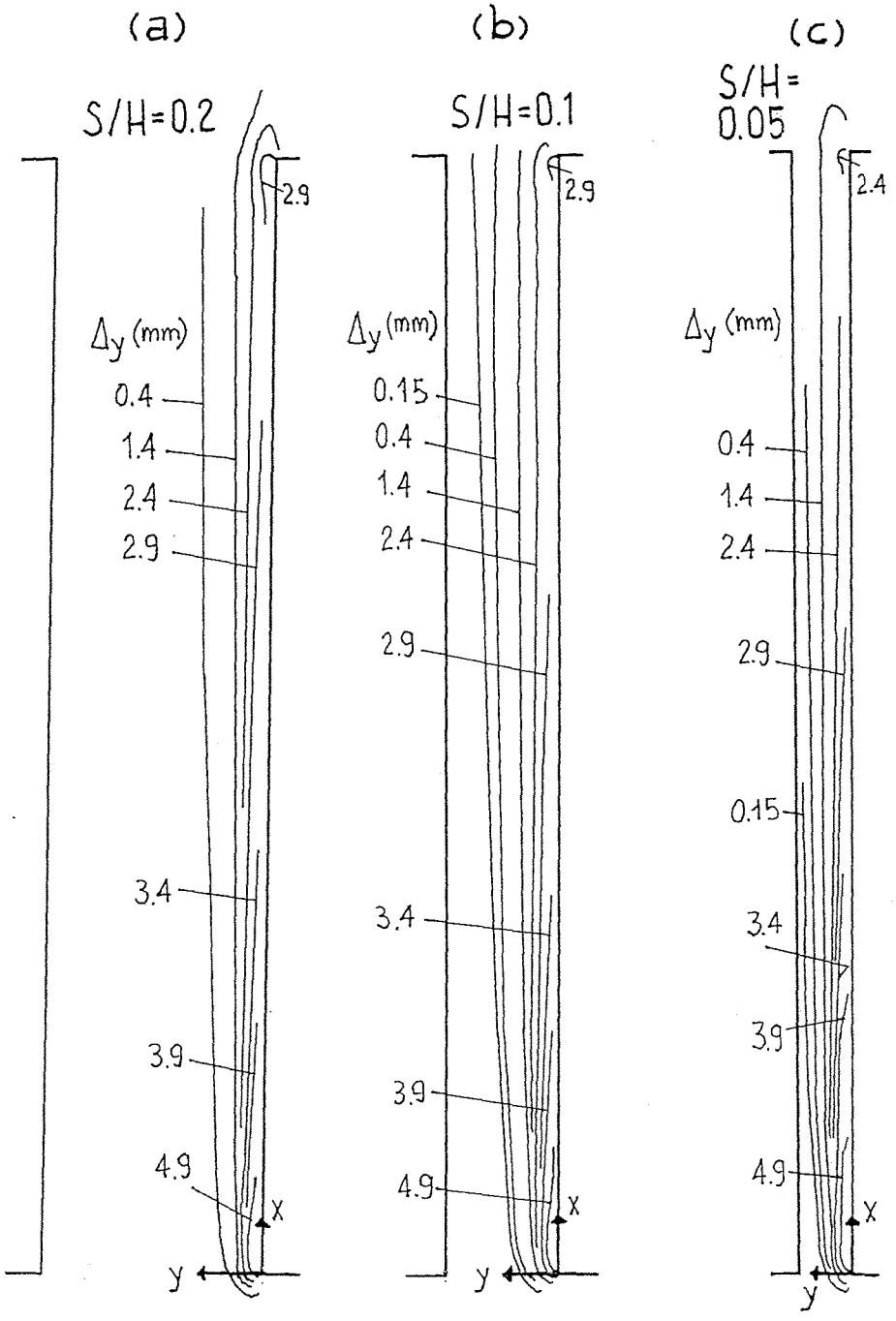

FIGURE 4.16 Lines of constant light-deviation Δy for the smooth channel configuration, $Ra=1.8\cdot10^{7}$. (a) S/H=0.2 , (b) S/H=0.1, (c) S/H=0.05.

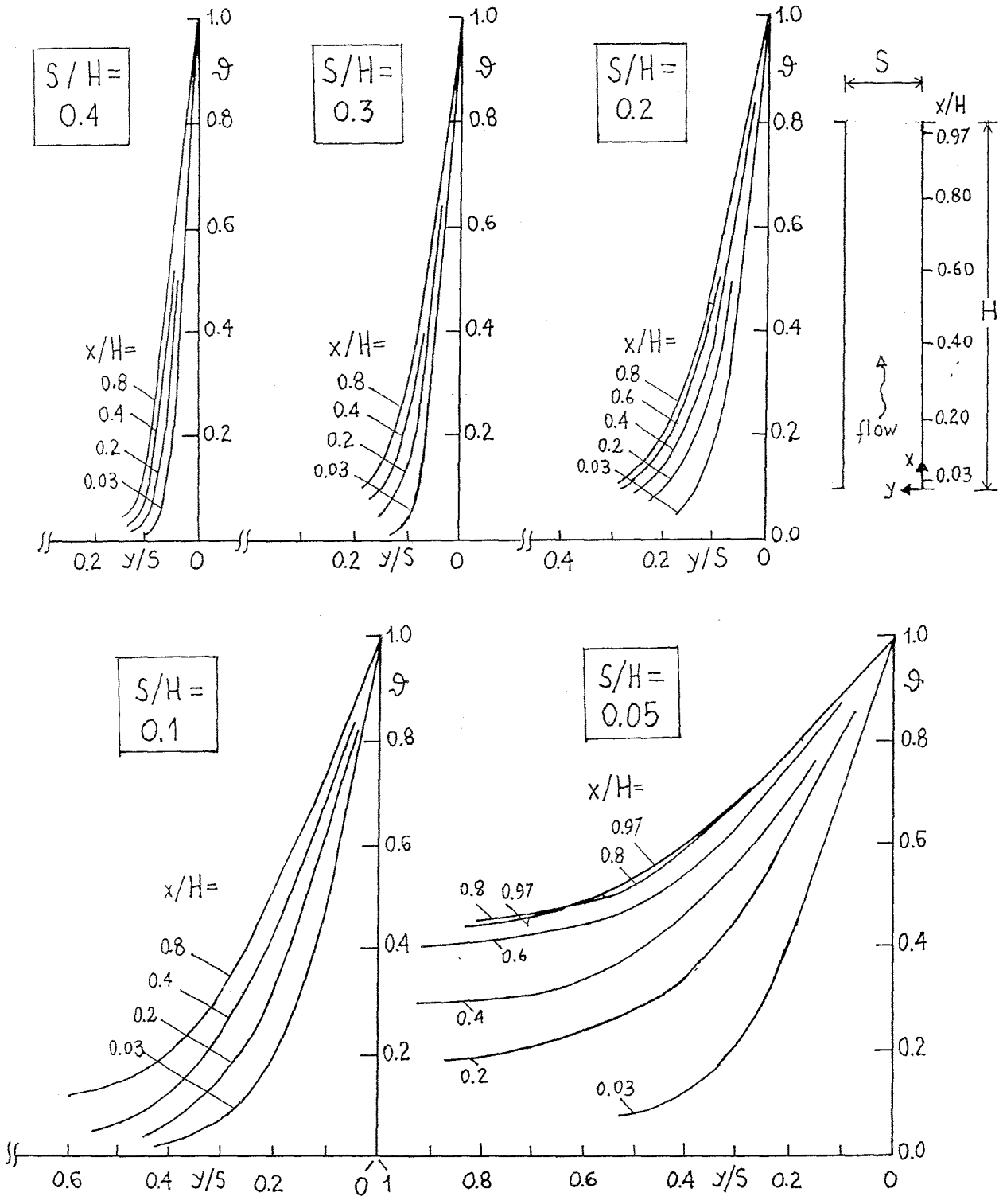

FIGURE 4.17 Dimensionless temperature profiles for the smooth channel configuration, $Ra=1.8 \cdot 10^7$.

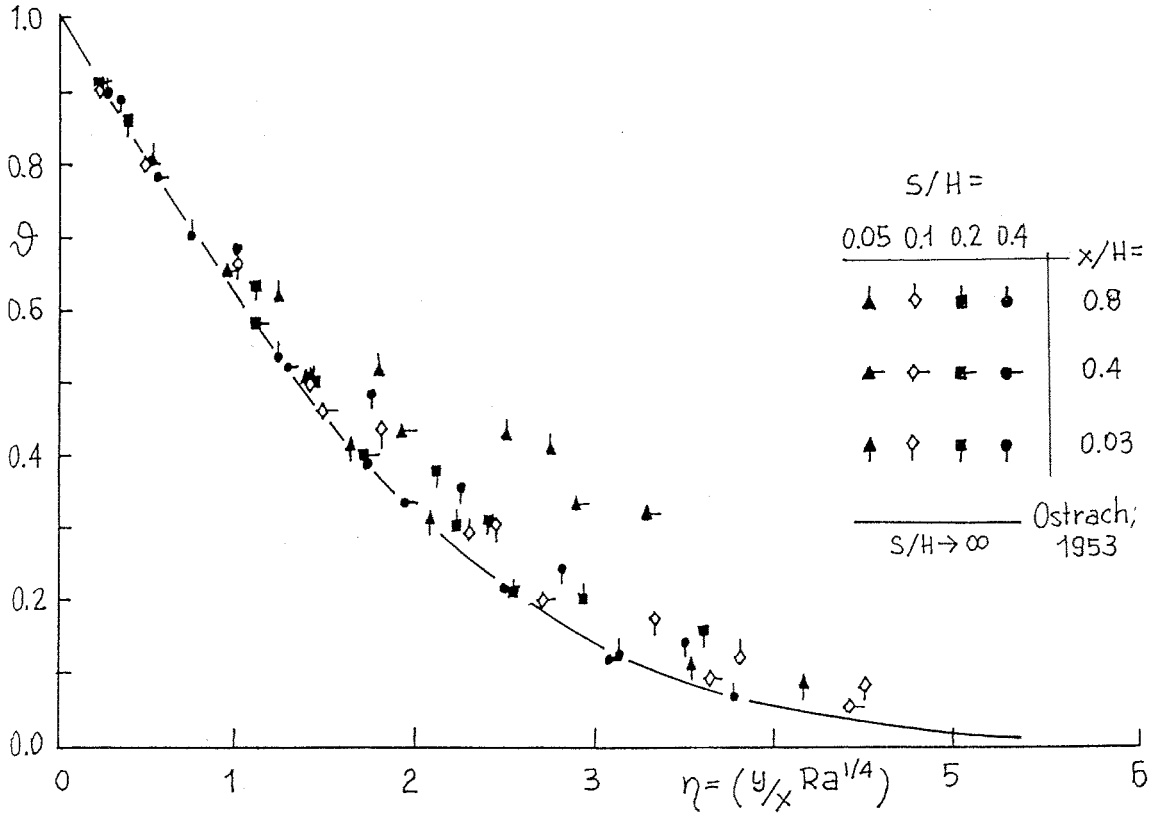

FIGURE 4.18 Dimensionless temperature data against the similarity variable $\eta=(y/x)Ra^{1/4}$.

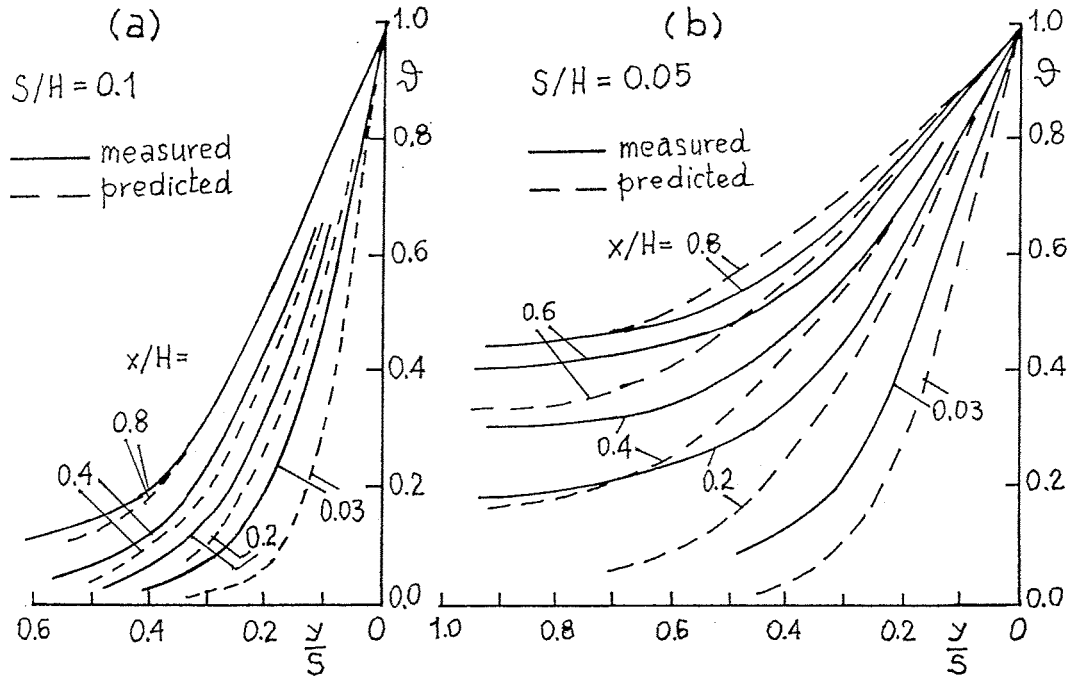

FIGURE 4.19 Comparison of measured temperature profiles with numerical predictions, $Ra=1.8\cdot10^7$: (a) S/H=0.1, (b) S/H 0.05.

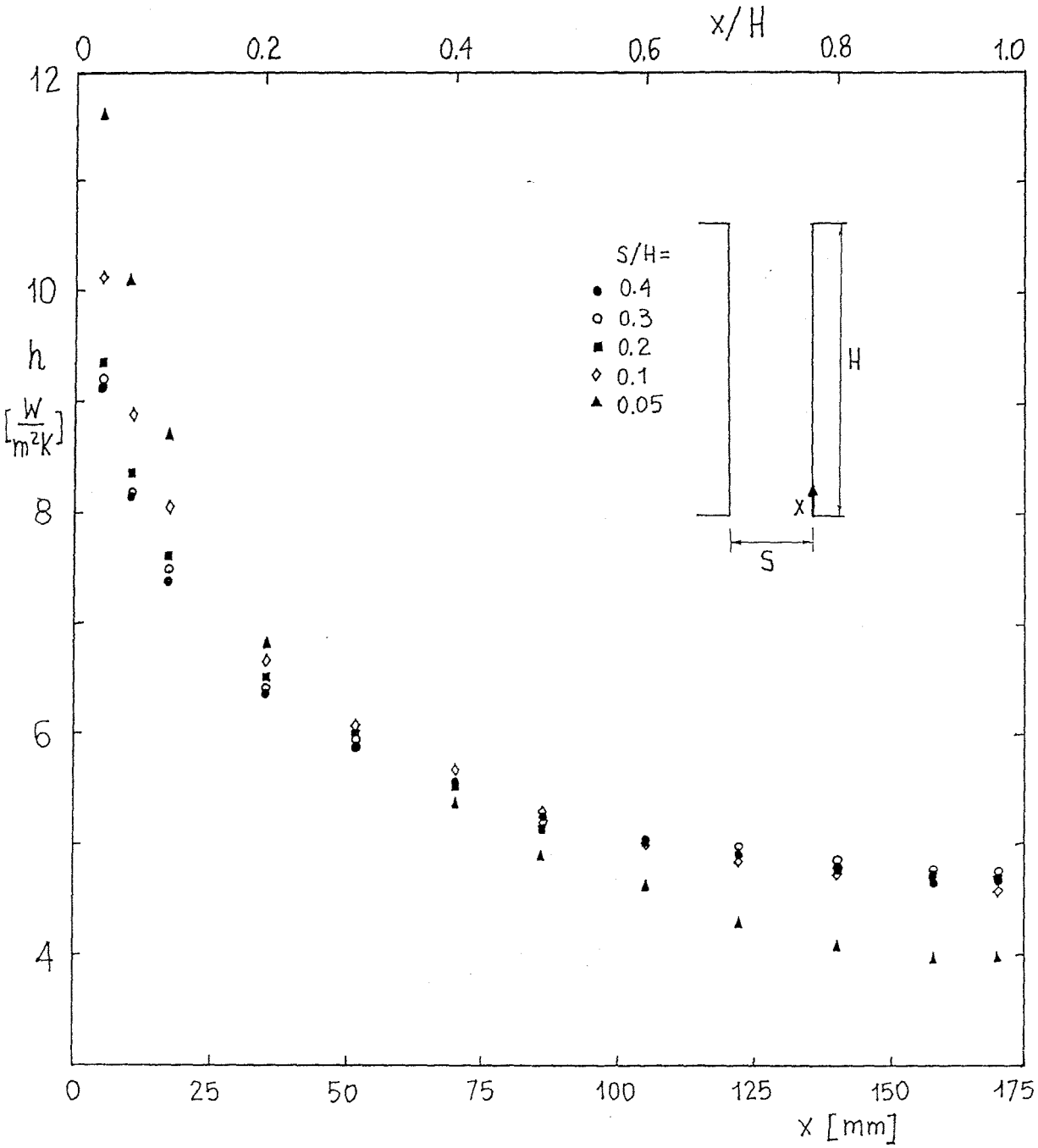

FIGURE 4.20 Heat transfer coefficient distributions, smooth channel configuration, $Ra=1.8 \cdot 10^7$.

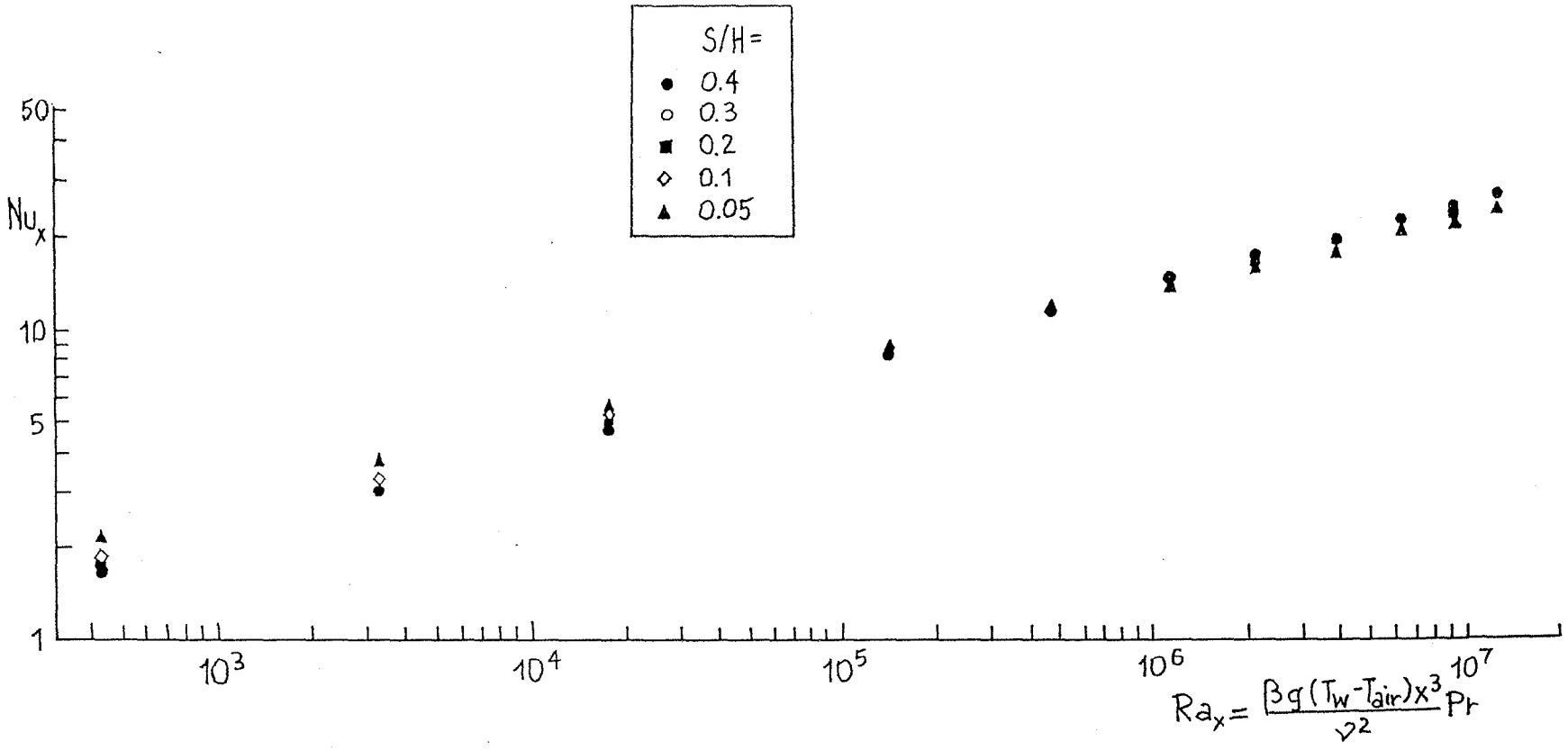

FIGURE 4.21 Local Nusselt number against the local Rayleigh number, smooth channel configuration.

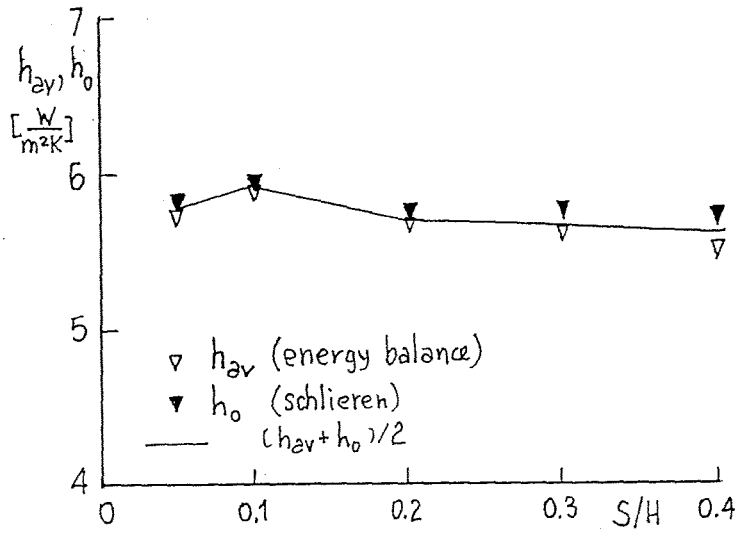

FIGURE 4.22 Overall heat transfer coefficients h_{av} (energy balance) and h_o (optical data) against S/H, smooth channel configuration, $Ra=1.8\cdot10^7$.

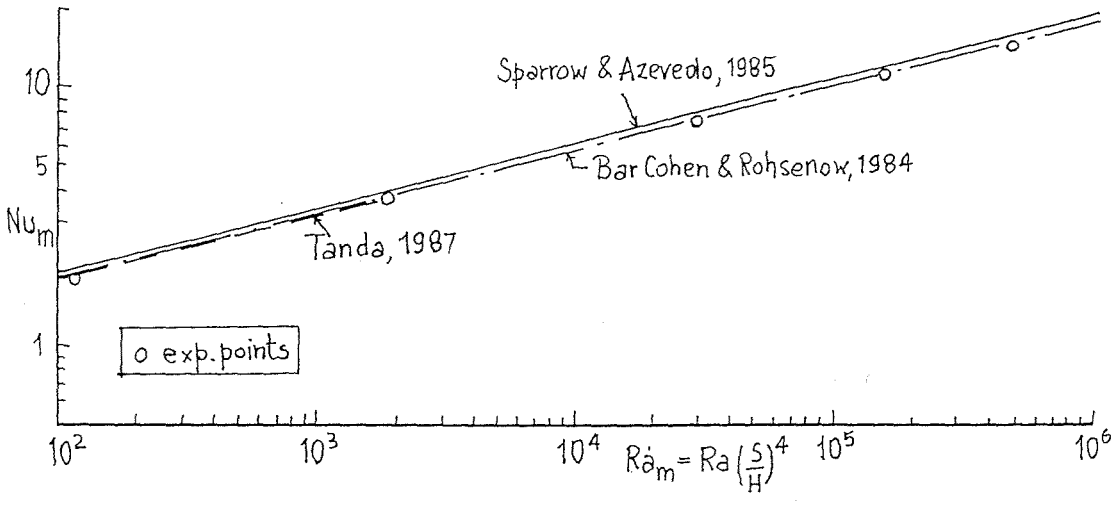

FIGURE 4.23 Overall (modified) Nusselt number against the modified Rayleigh number, smooth channel configuration.

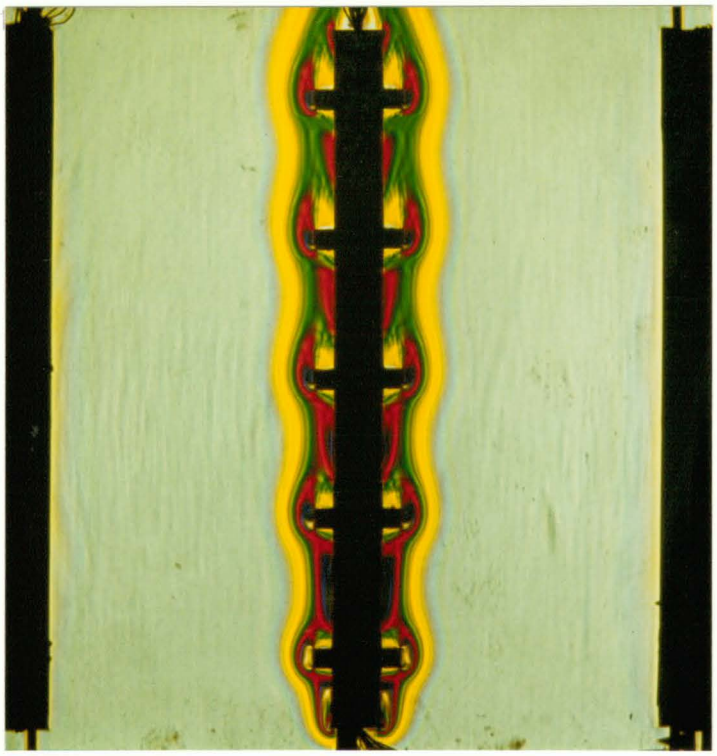

(a)

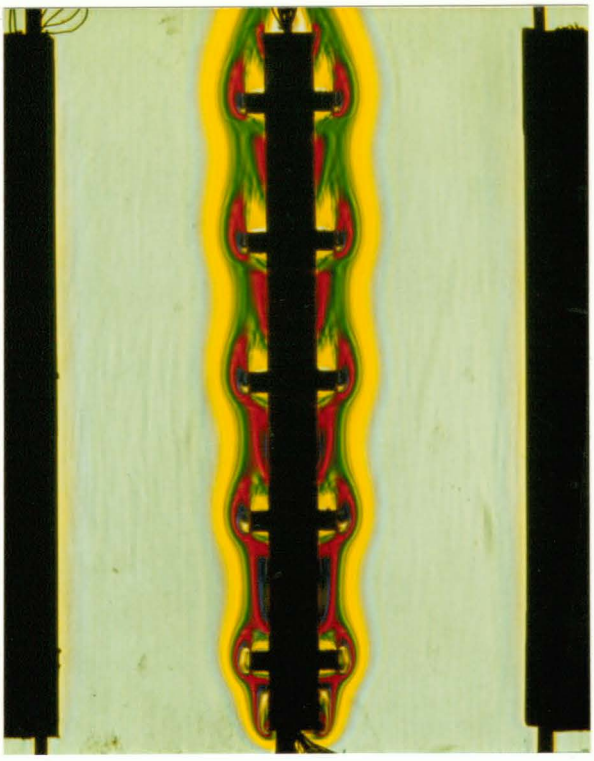

(b)

FIGURE 4.24 Colour schlieren images of the rough channel assembly, filter mounted vertically, $Ra=1.8 \cdot 10^7$: (a) S/H=0.4, (b) S/H=0.3.

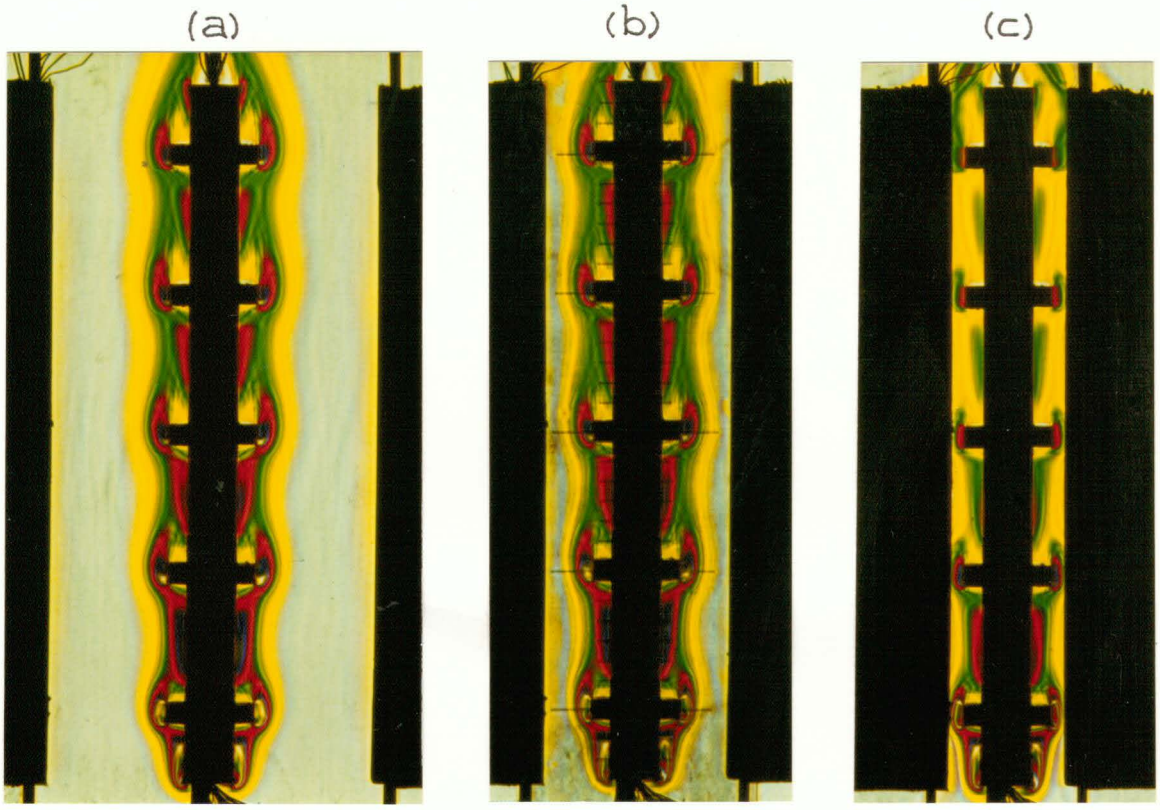

FIGURE 4.25 Colour schlieren images of the rough channel assembly, filter mounted vertically, $Ra=1.8 \cdot 10^7$: (a) S/H=0.2, (b) S/H=0.1, (c) S/H=0.05.

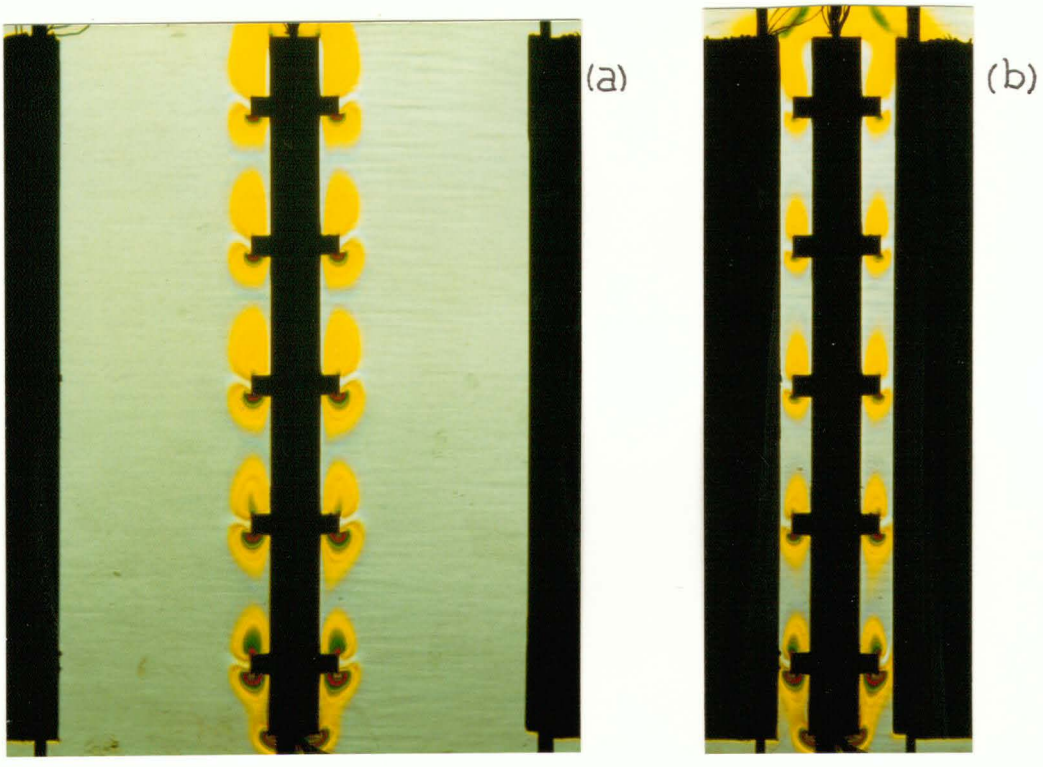

FIGURE 4.26 Colour schlieren images of the rough channel assembly, filter mounted horizontally, $Ra=1.8 \cdot 10^7$: (a) S/H=0.3, (b) S/H= 0.05.

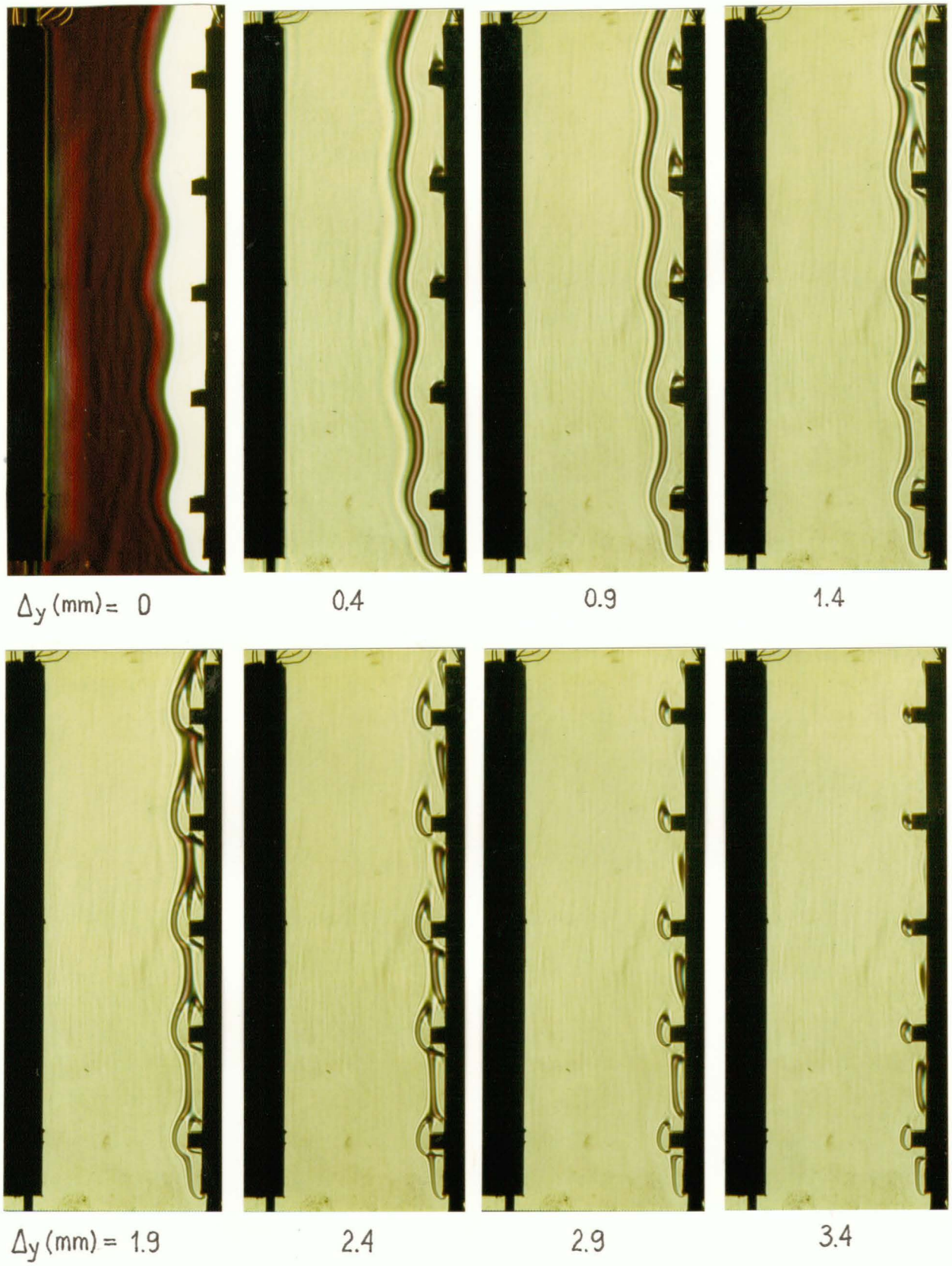

FIGURE 4.27 Schlieren images (focal filament method) of the rough channel configuration, filter mounted vertically, $Ra=1.8 \cdot 10^7$, S/H=0.3. Δ_y from 0 (top left) to 3.4 mm (bottom right).

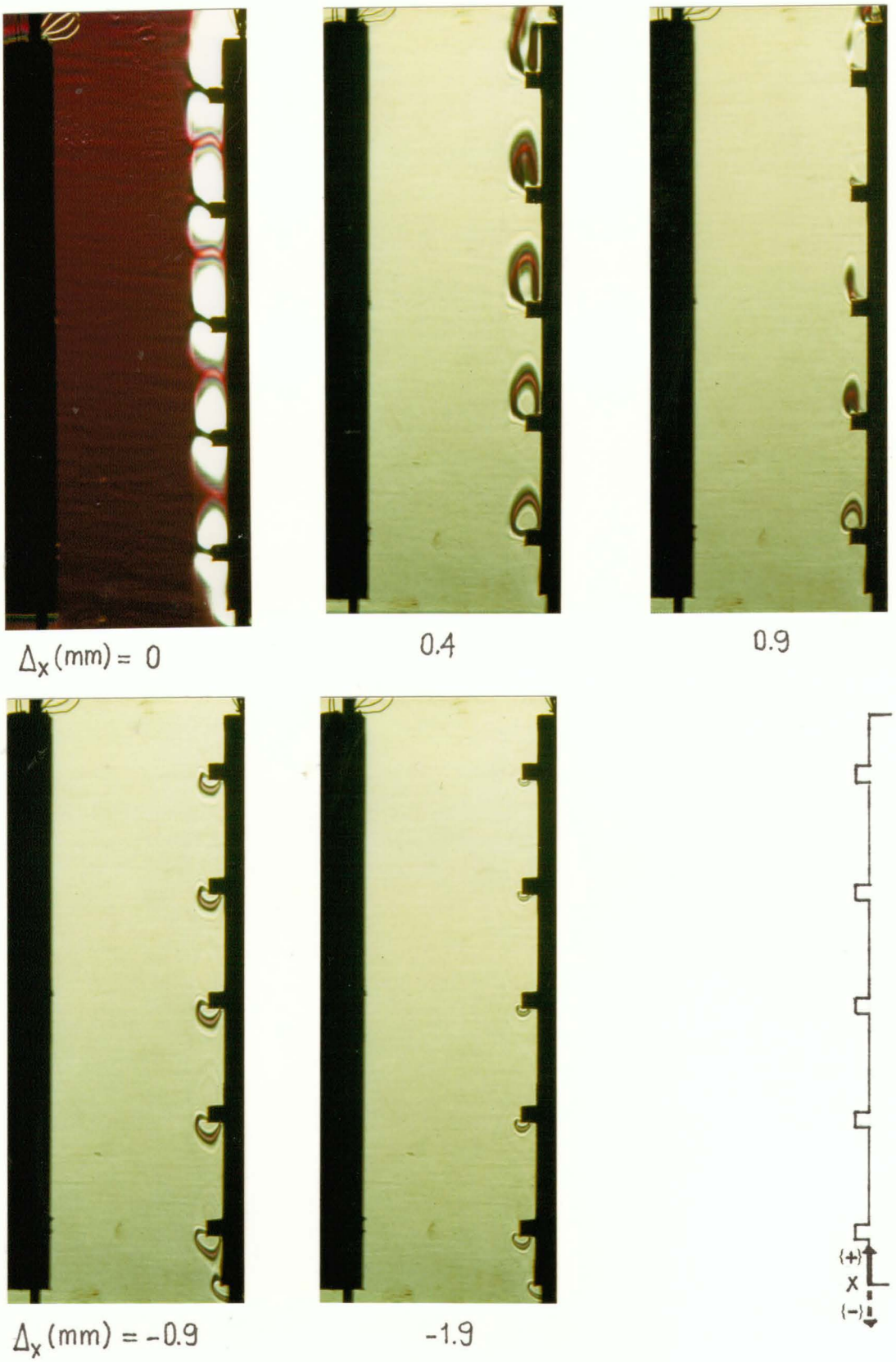

FIGURE 4.28 Schlieren images (focal filament method) of the rough channel configuration, filter mounted horizontally, $Ra=1.8 \cdot 10^7$, S/H=0.3. Δ_x from 0 to 0.9 mm (top) and to -1.9 mm (bottom).

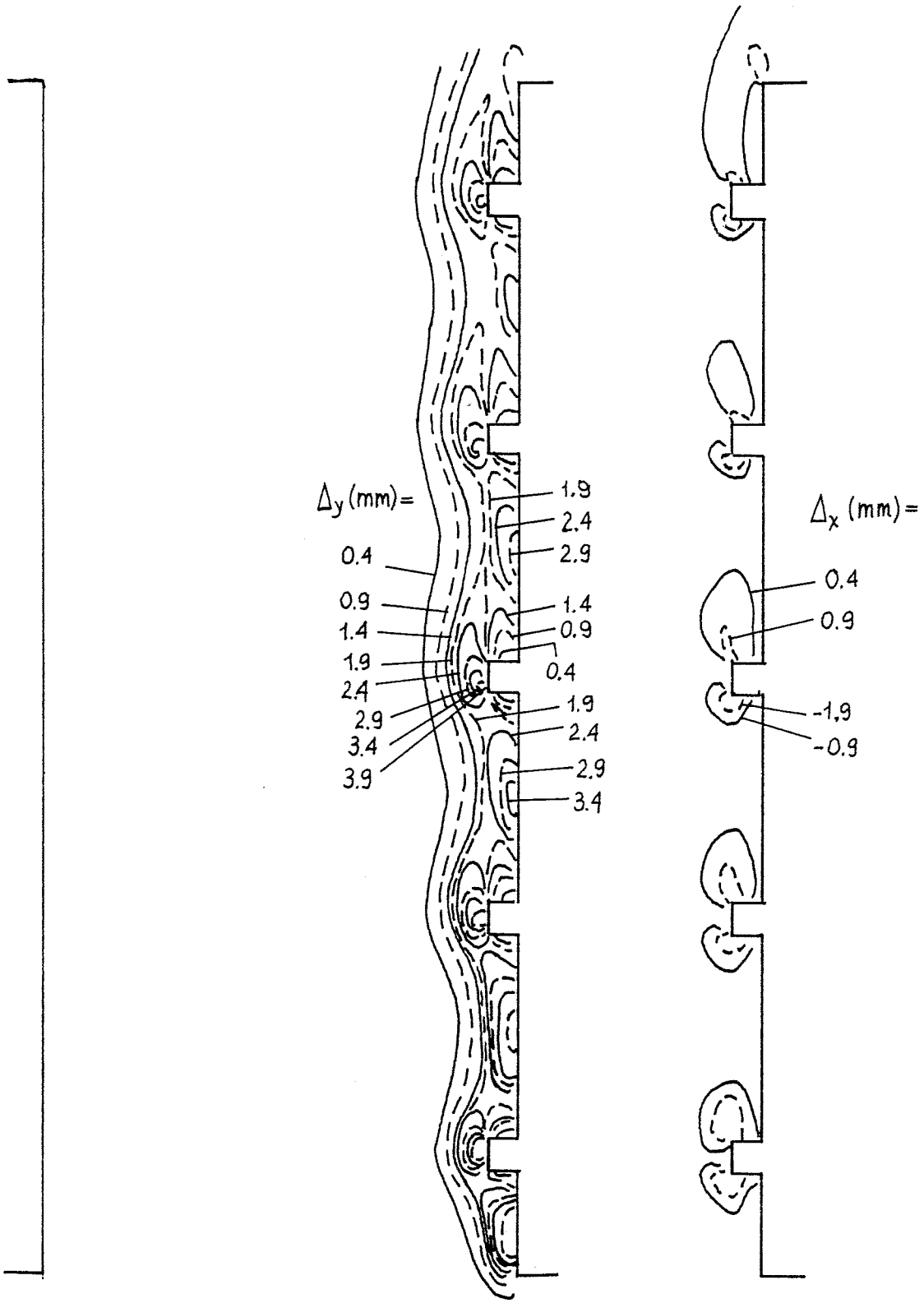

FIGURE 4.29 Lines of constant light-deviation Δy (left) and Δx (right) for the rough channel configuration, $Ra=1.8 \cdot 10^7$. S/H=0.4.

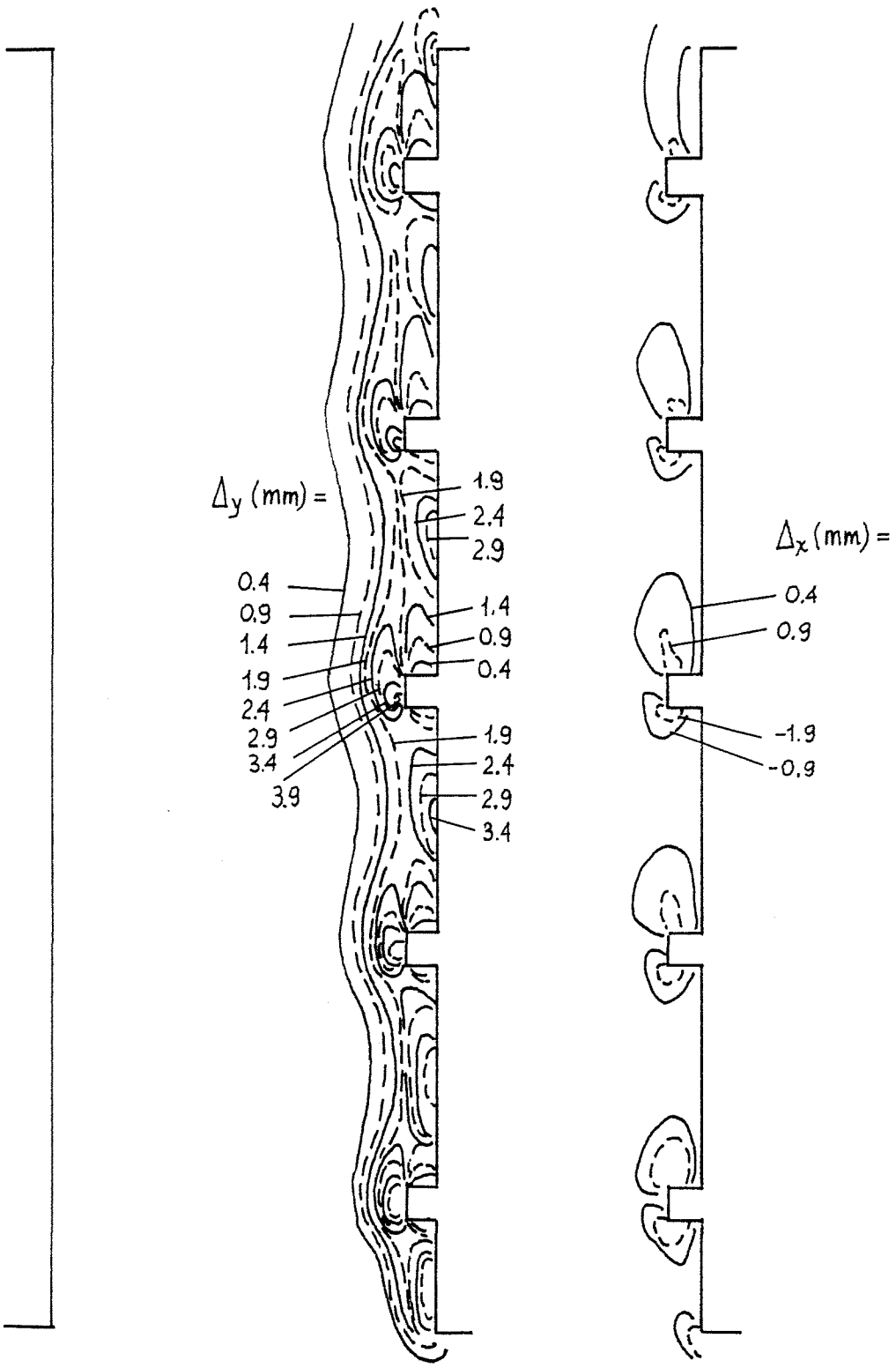

FIGURE 4.30 Lines of constant light-deviation Δ_y (left) and Δ_x (right) for the rough channel configuration, $Ra=1.8 \cdot 10^7$. S/H=0.3.

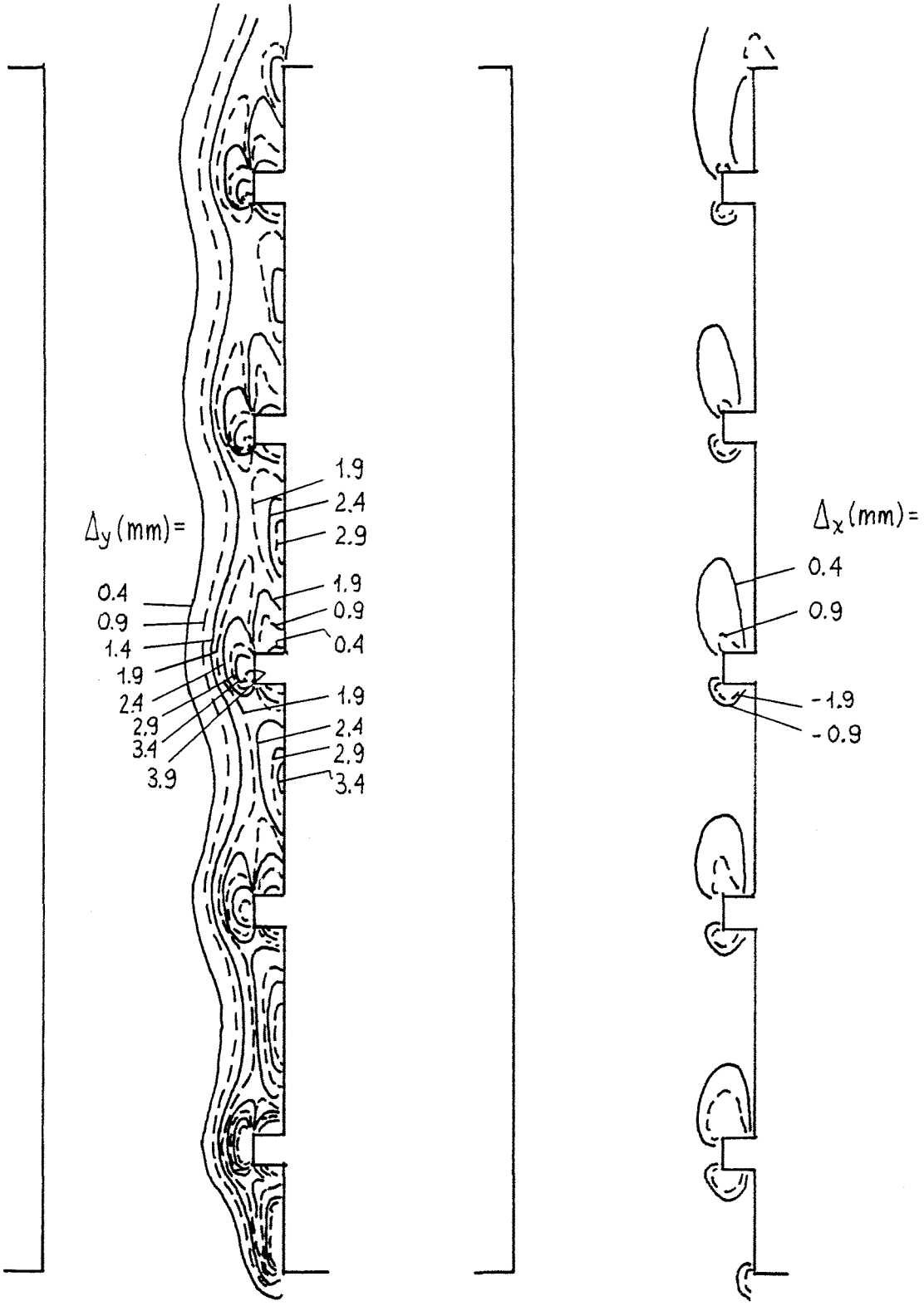

FIGURE 4.31 Lines of constant light-deviation Δy (left) and Δx (right) for the rough channel configuration, $Ra=1.8 \cdot 10^7$. S/H=0.2.

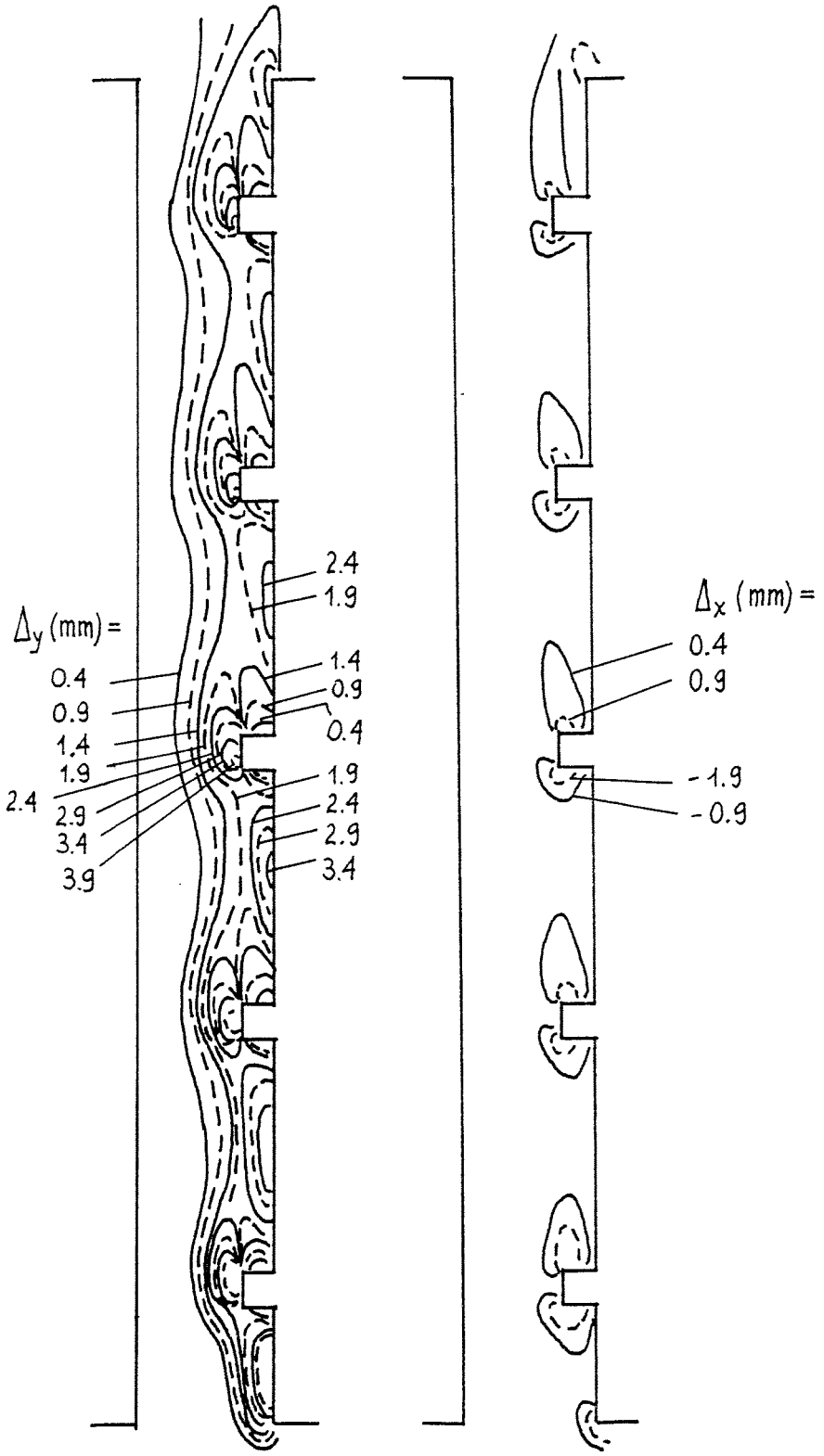

FIGURE 4.32 Lines of constant light-deviation Δ_y (left) and Δ_x (right) for the rough channel configuration, $Ra=1.8 \cdot 10^7$. S/H=0.1.

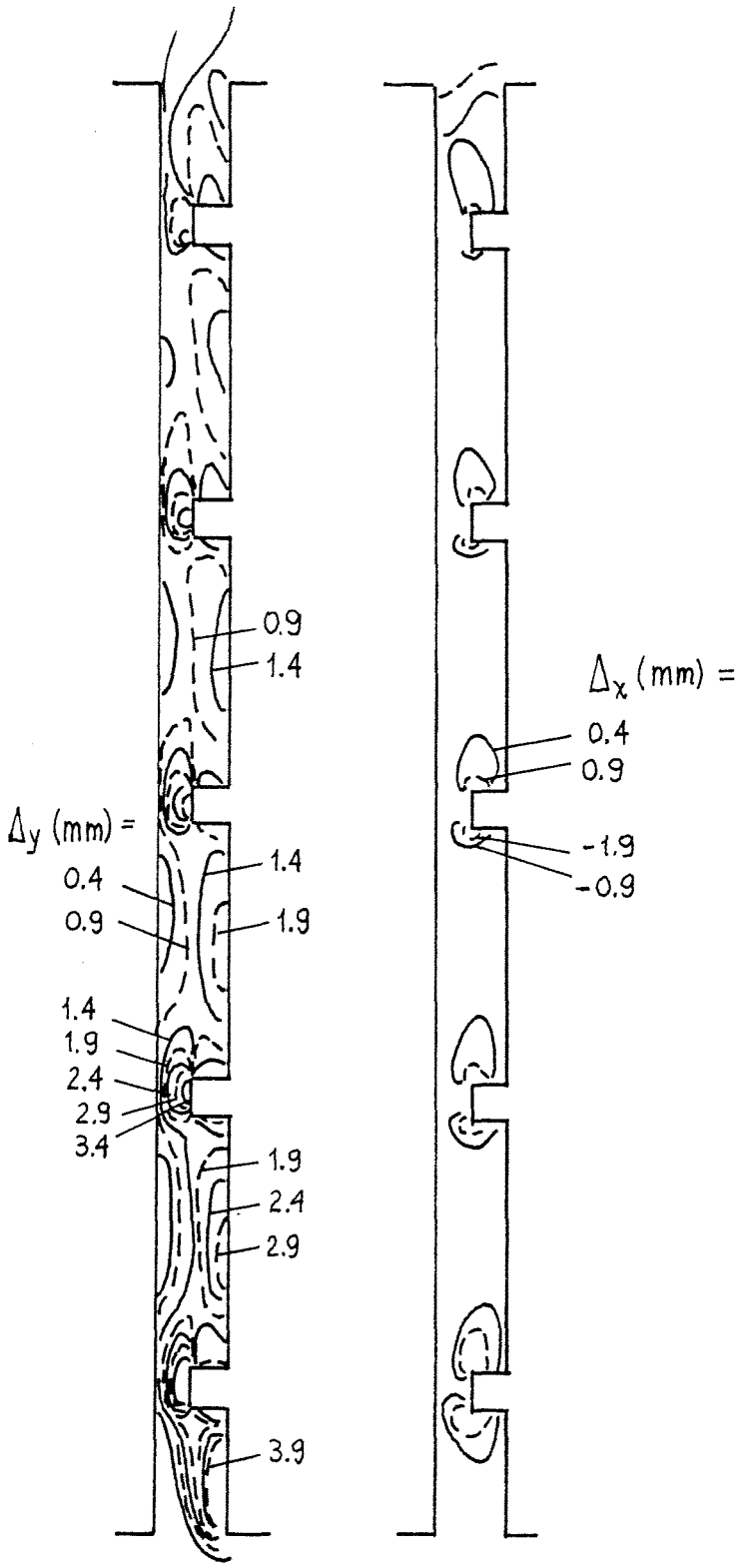

FIGURE 4.33 Lines of constant light-deviation Δy (left) and Δx (right) for the rough channel configuration, $Ra=1.8 \cdot 10^7$. S/H=0.05.

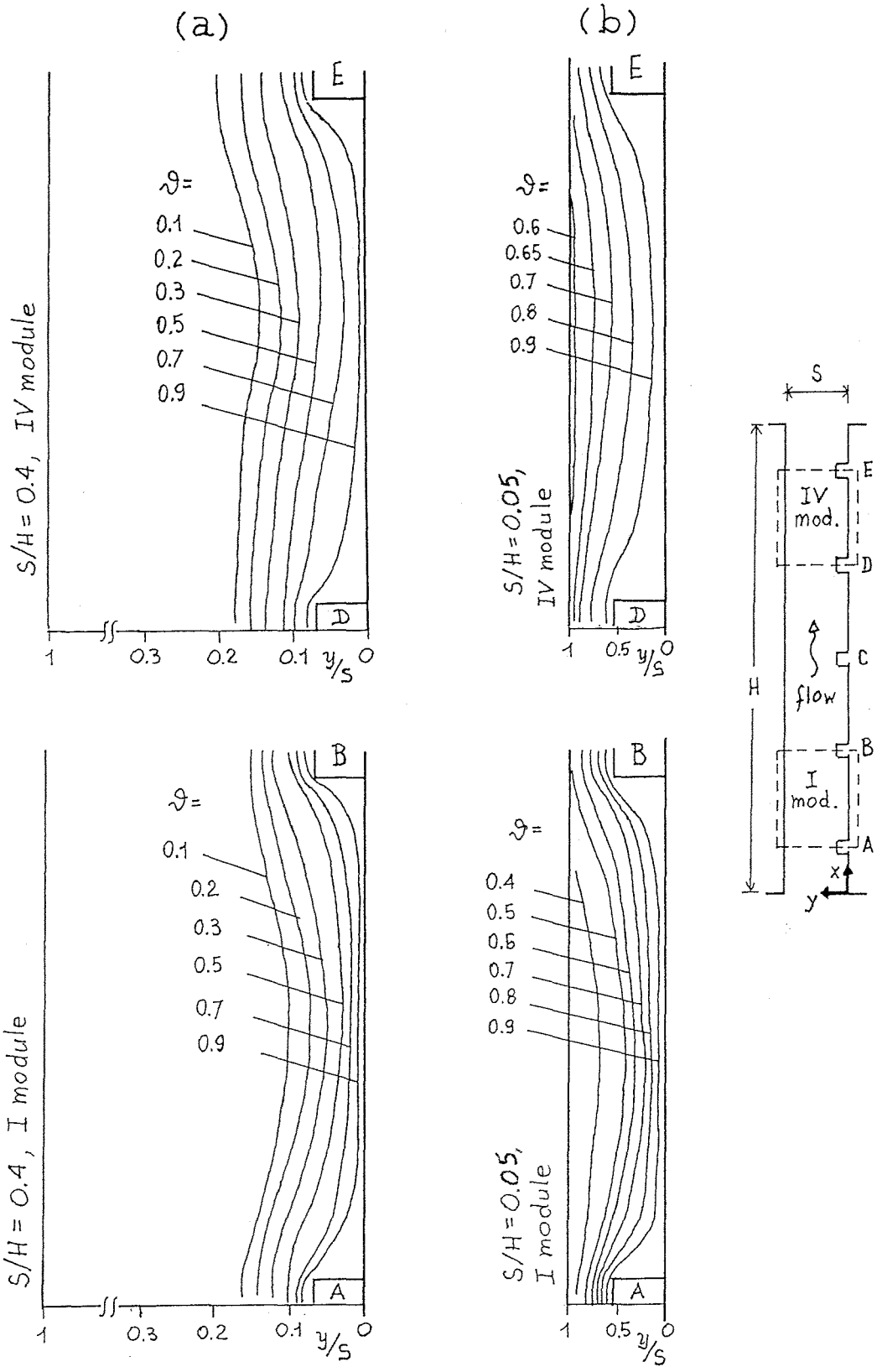

FIGURE 4.34 Isotherm contours for the first and the last module, rough channel configuration, Ra=$1.8 \cdot 10^7$: (a) S/H=0.4 , (b) S/H=0.05.

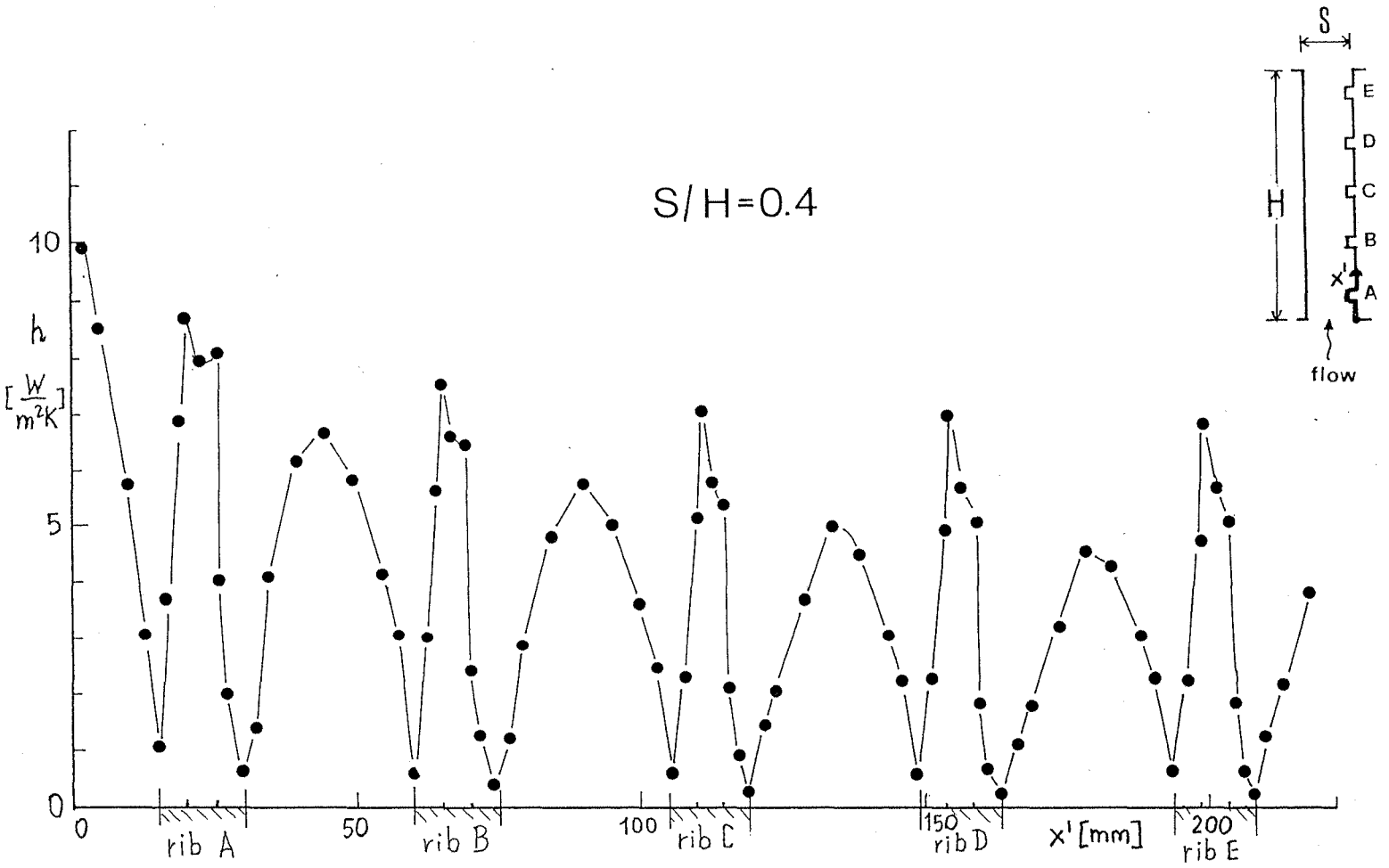

FIGURE 4.35 Heat transfer coefficient distribution, rough-channel config.,Ra=$1.8 \cdot 10^7$,S/H=0.4.

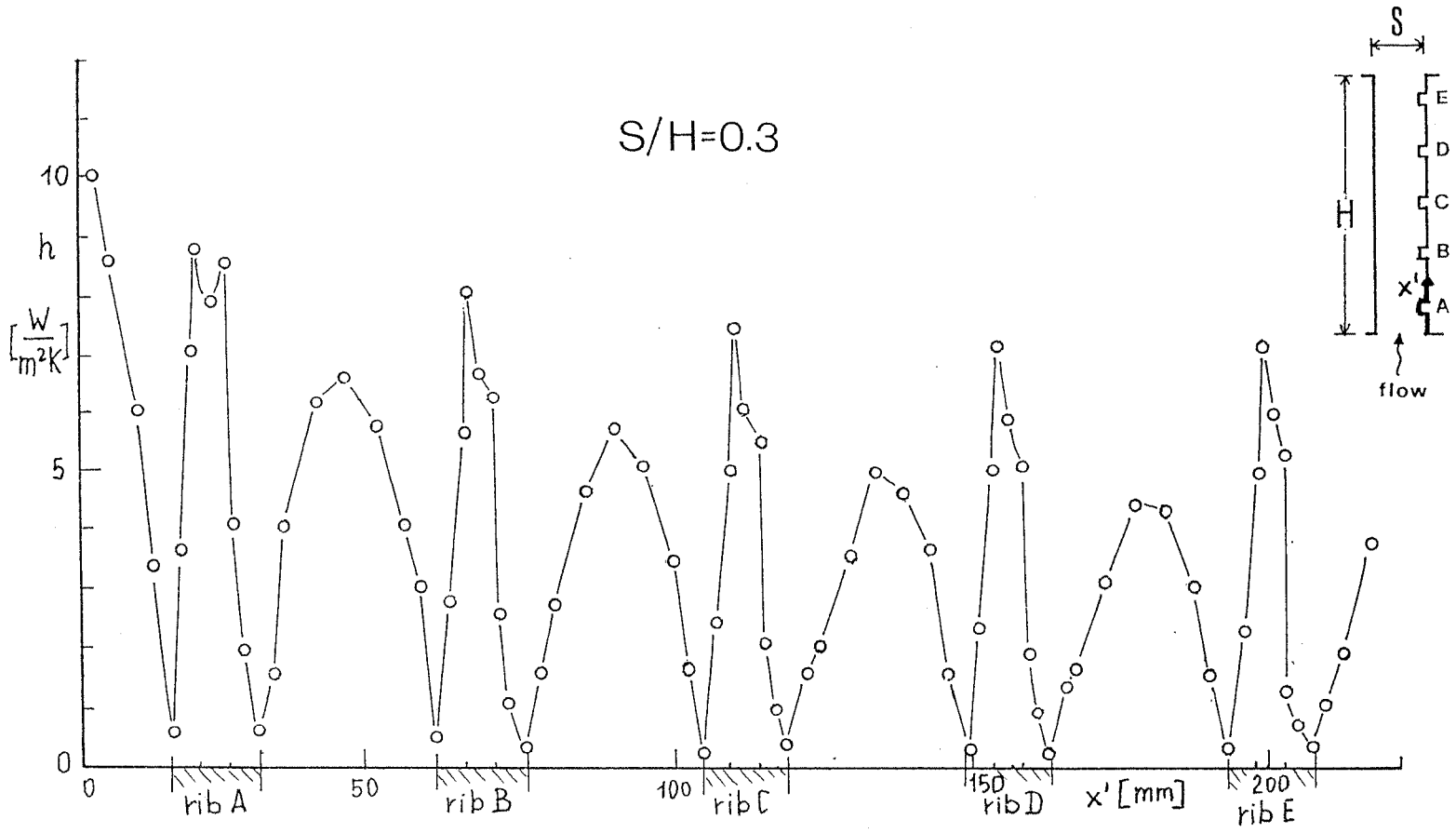

FIGURE 4.36 Heat transfer coefficient distribution, rough-channel config., $Ra=1.8\cdot10^{7}$, S/H=0.3.

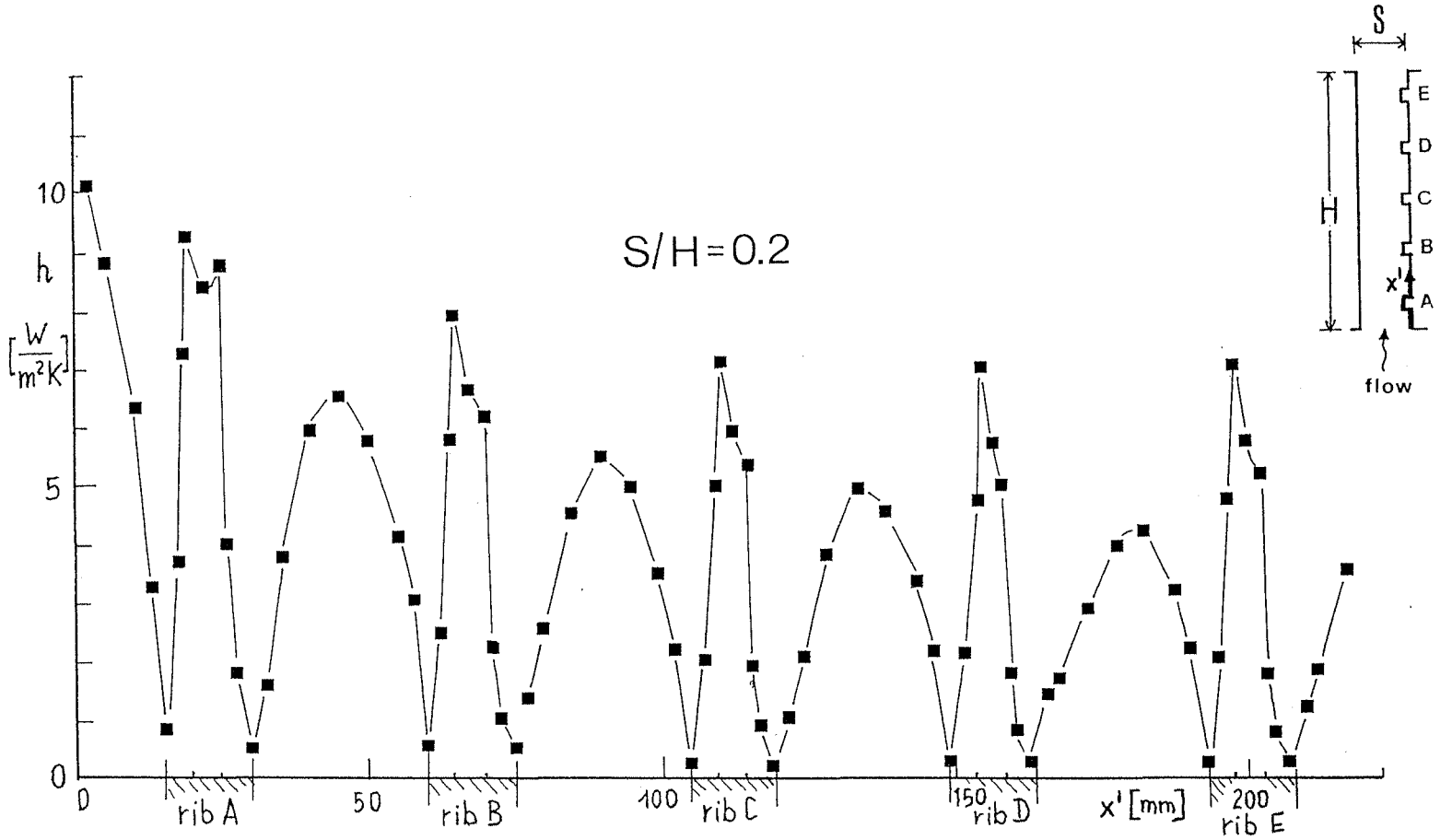

FIGURE 4.37 Heat transfer coefficient distribution, rough-channel config., $Ra=1.8\cdot10^7$, S/H=0.2.

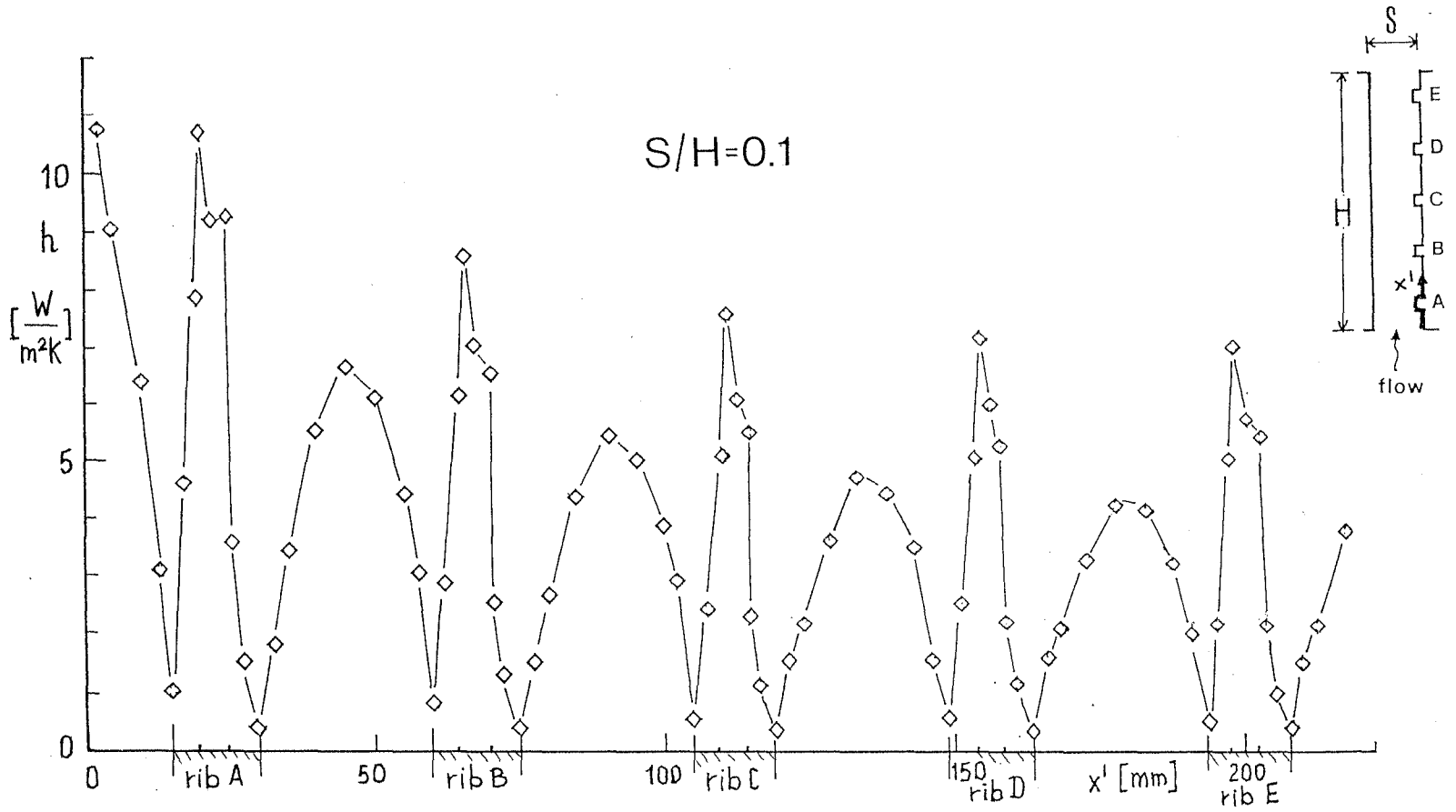

FIGURE 4.38 Heat transfer coefficient distribution, rough-channel config., $Ra=1.8\cdot10^{7}$, $S/H=0.1$.

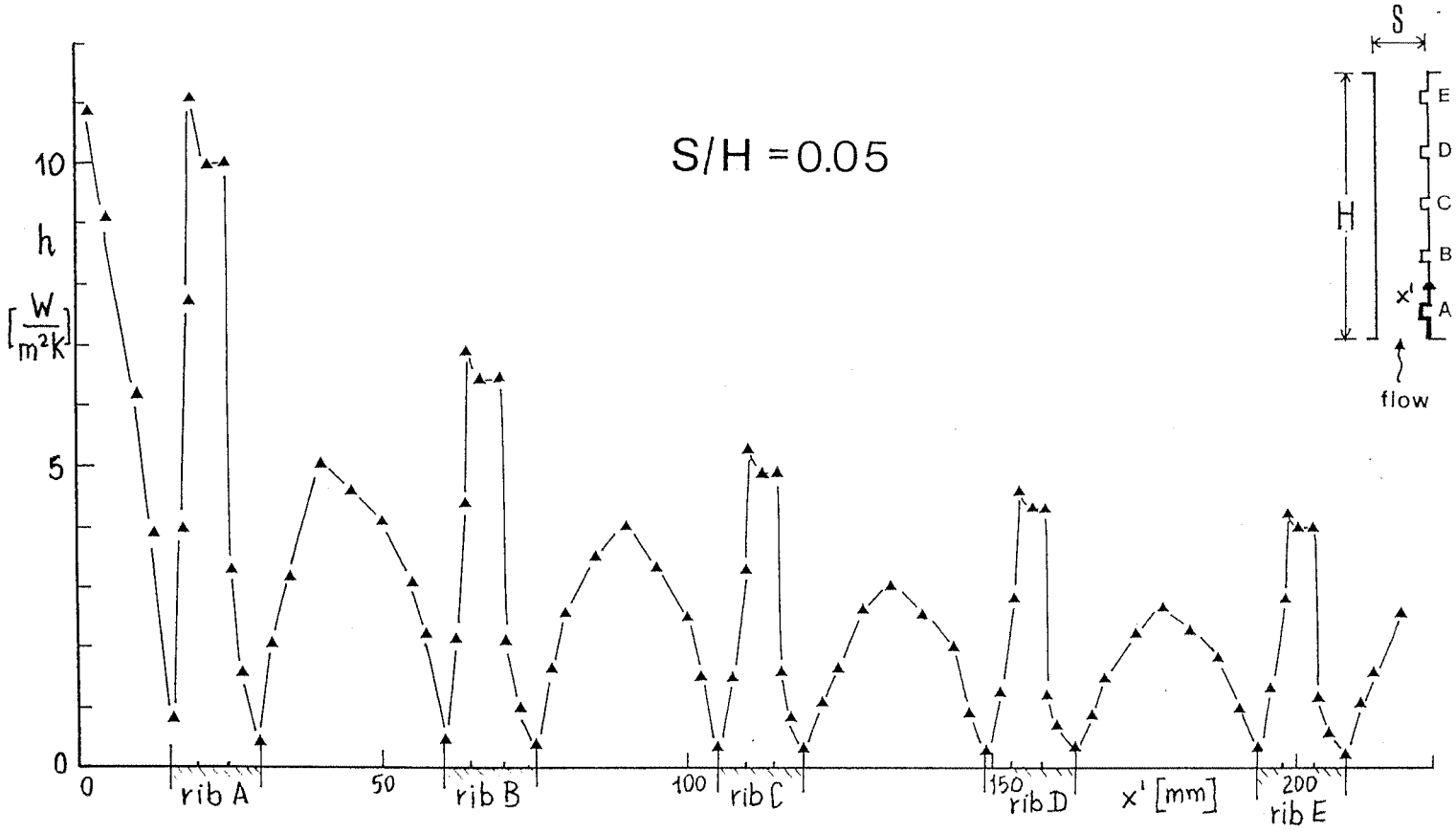

FIGURE 4.39 Heat transfer coefficient distribution, rough-channel config., $Ra=1.8\cdot10^{7}$, $S/H=0.05$.

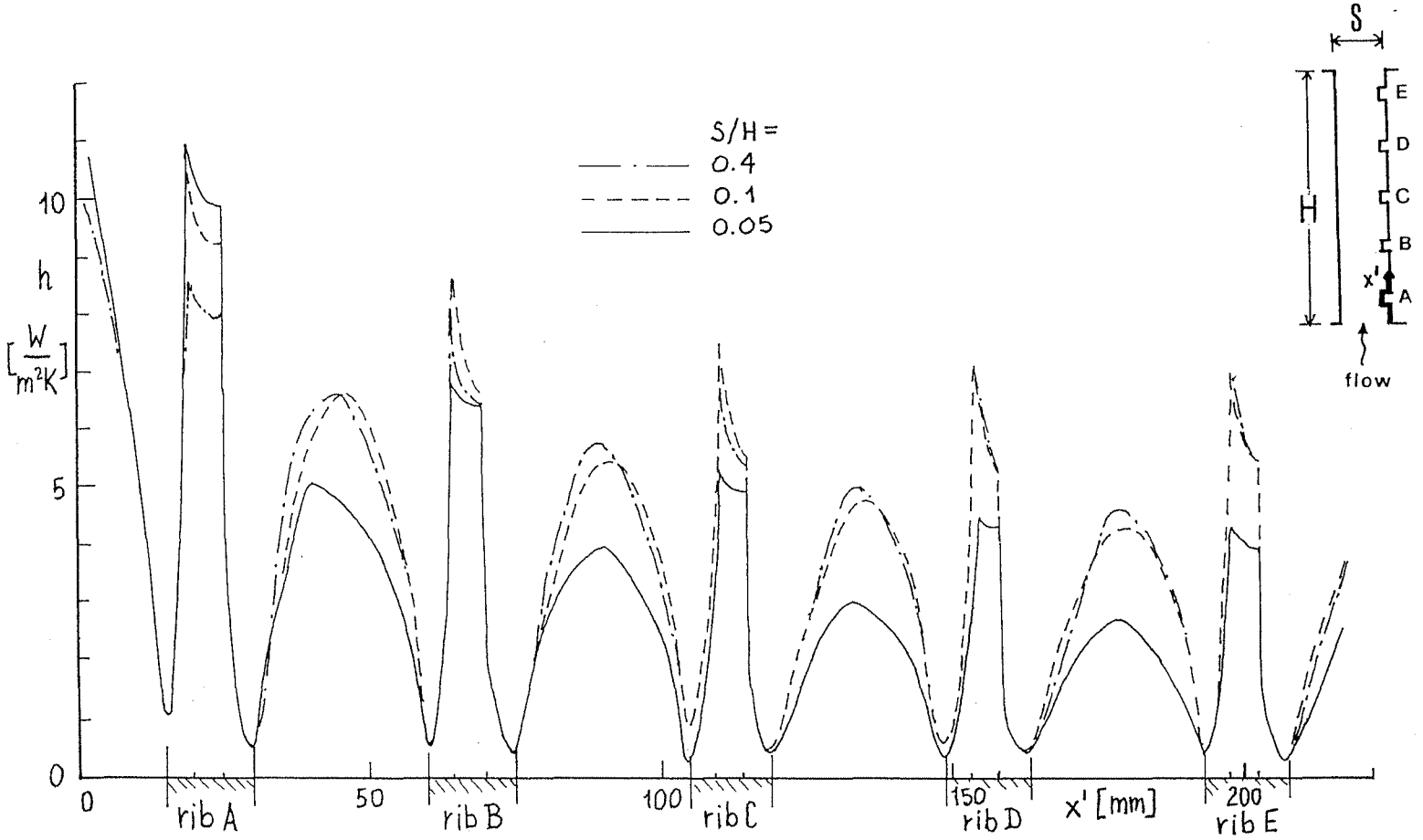

FIGURE 4.40 Comparison among measured heat transfer coefficients for S/H=0.4, 0.1 and 0.05.

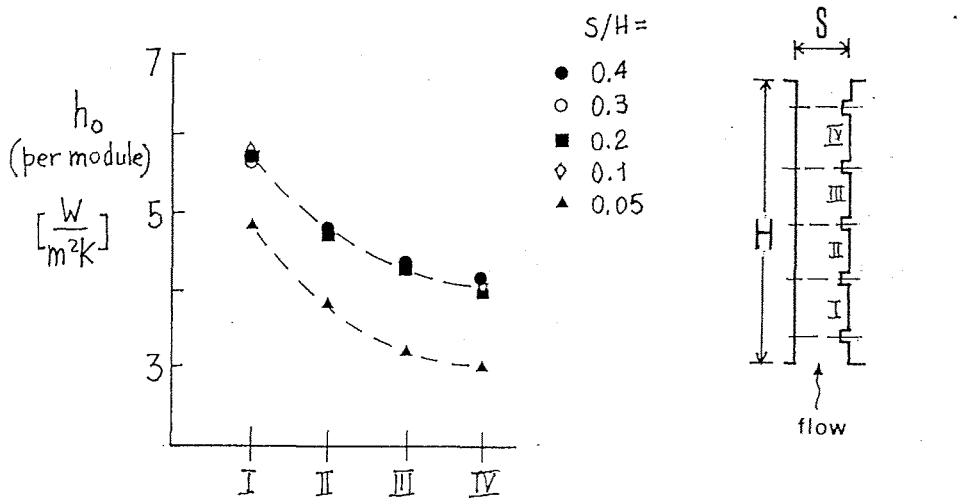

FIGURE 4.41 Heat transfer coefficients averaged per-module; rough channel configuration, $Ra=1.8\cdot10^7$.

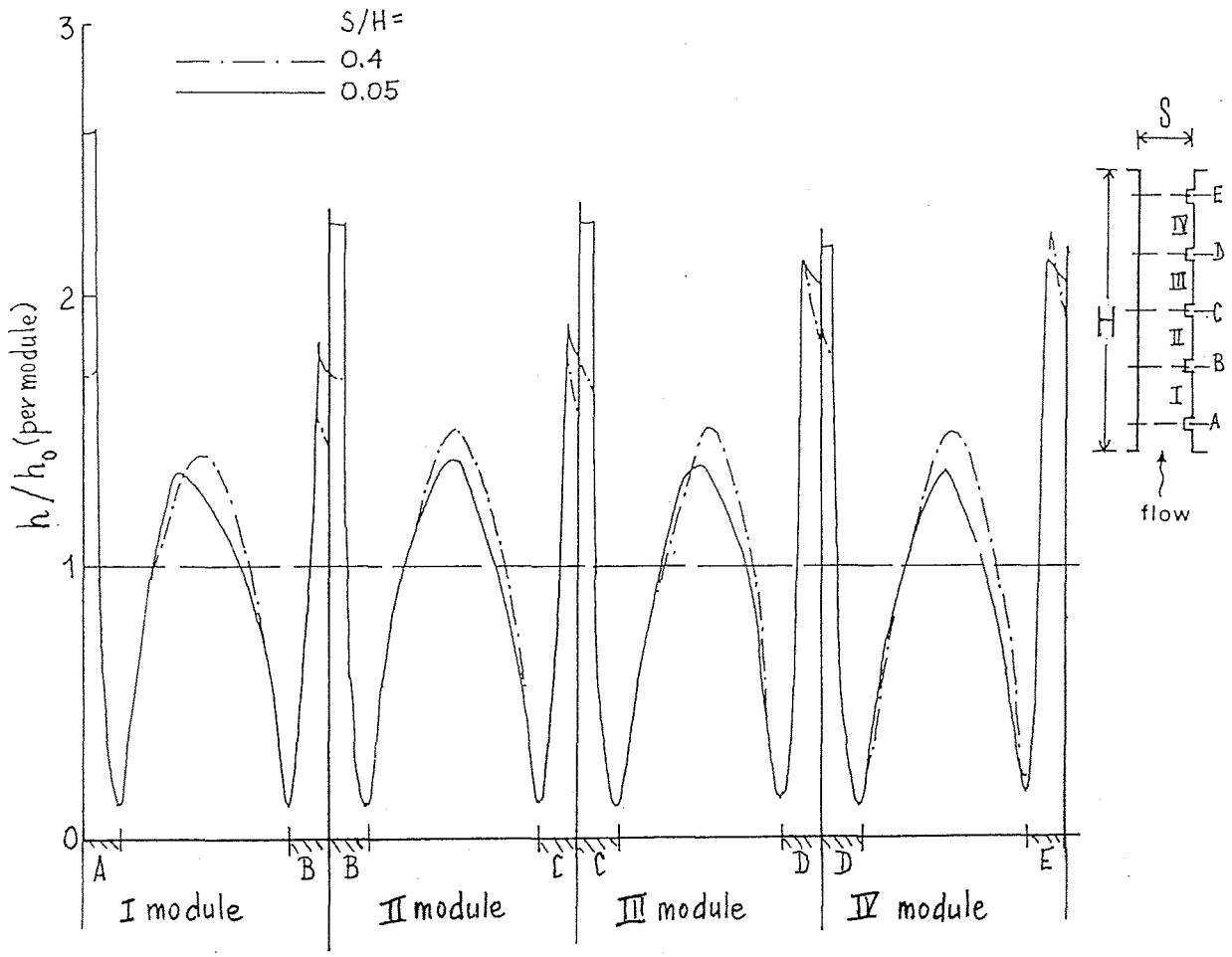

FIGURE 4.42 Heat transfer coefficients normalised by the corresponding module-averaged value. S/H=0.4 and 0.05.

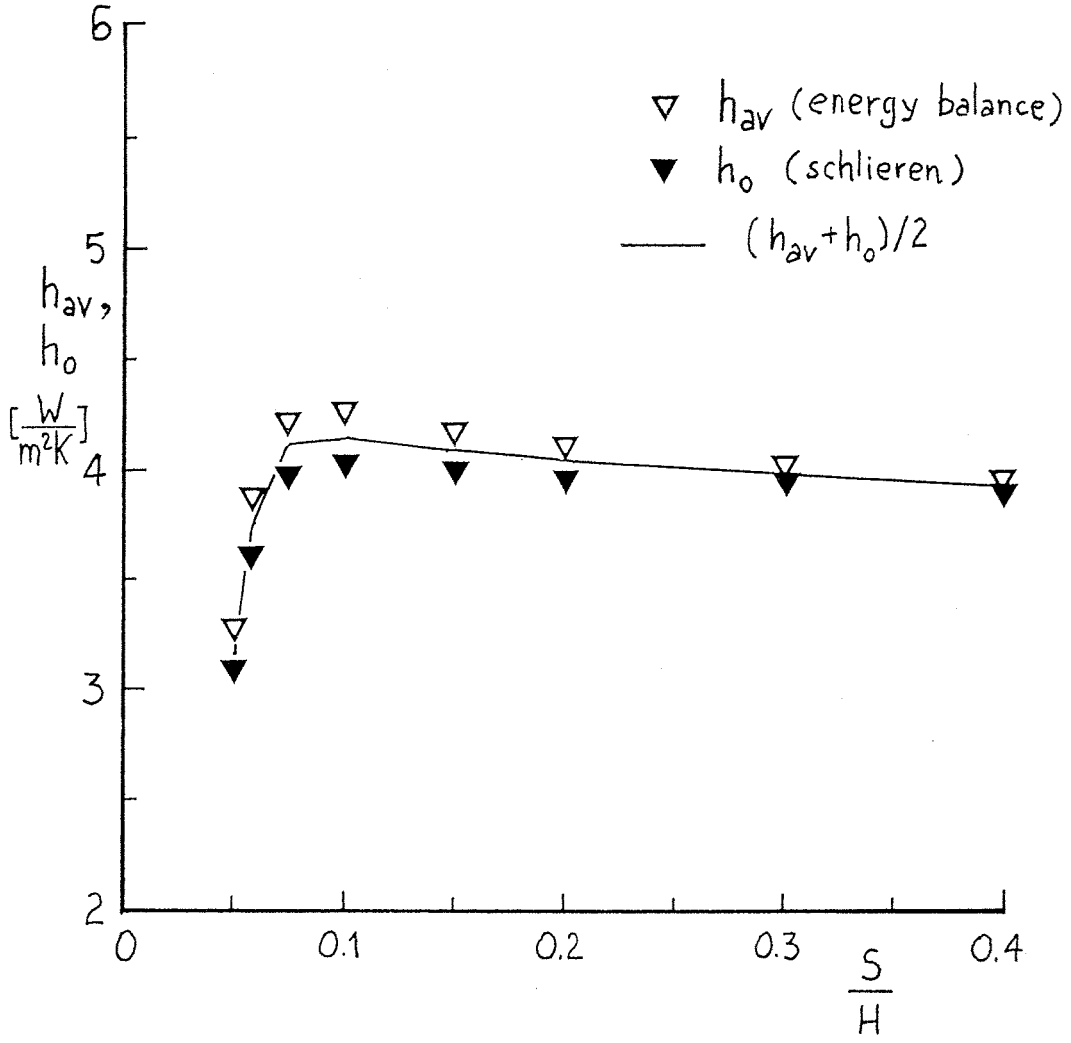

FIGURE 4.43 Overall heat transfer coefficients h_{av} (energy balance) and h_o (optical data) against S/H, rough channel configuration, $Ra=1.8\cdot10^7$.

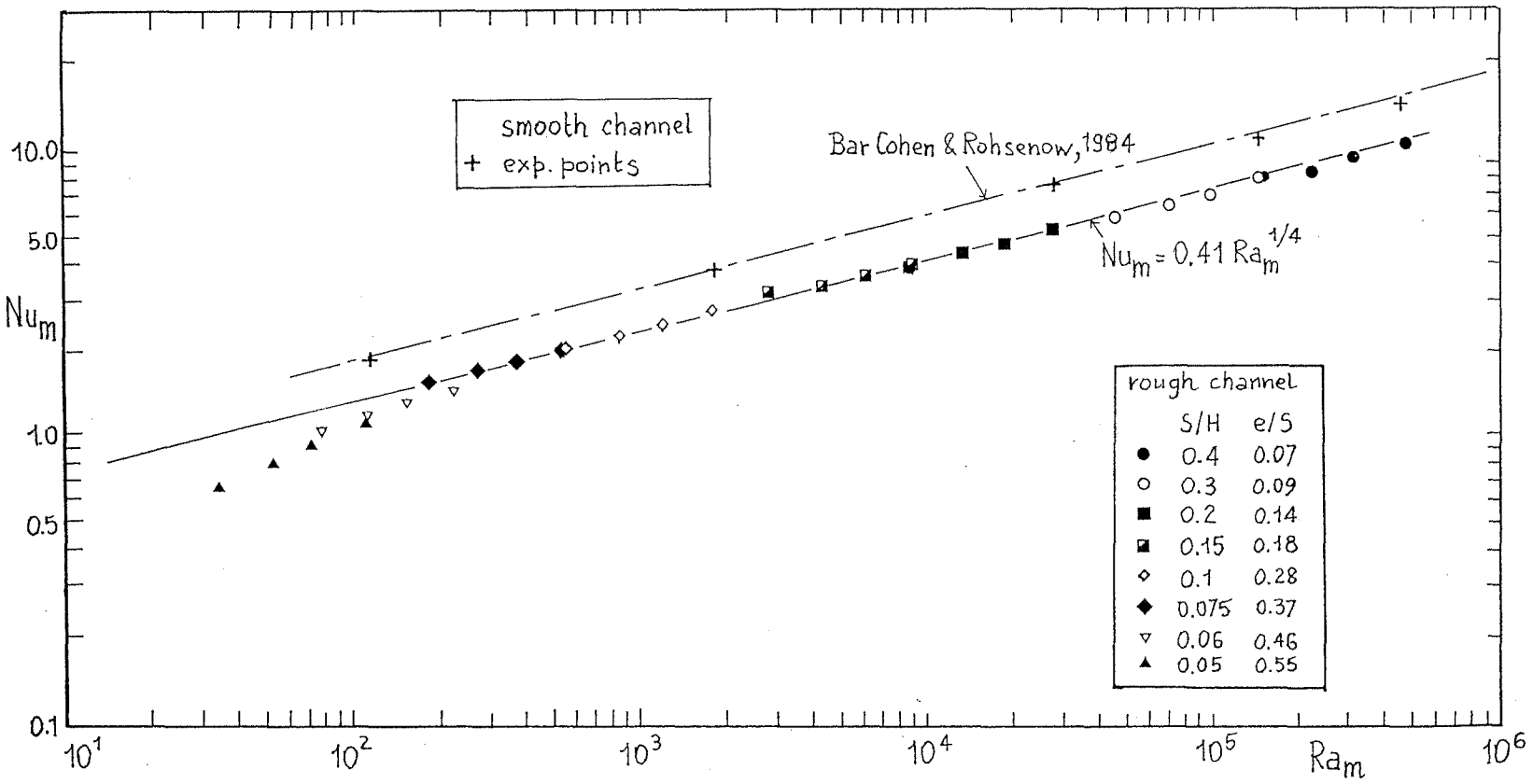

FIGURE 4.44 Overall (modified) Nusselt number against the modified Rayleigh number for the rough channel configuration.

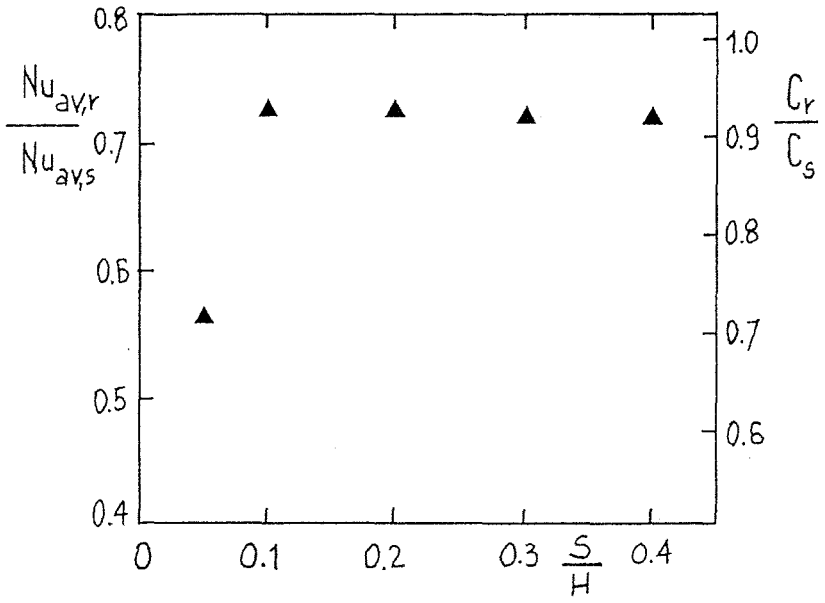

FIGURE 4.45 Nusselt number and thermal conductance of the rough wall, normalised by the values for the smooth wall.

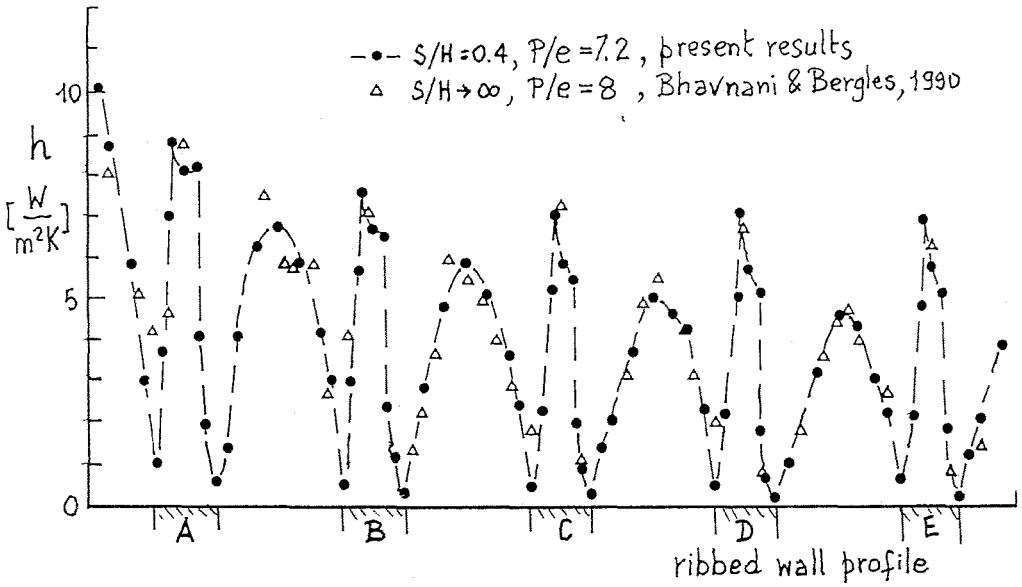

FIGURE 4.46 Heat transfer coefficients of the rough wall. Comparison between present results and published data (Bhavnani and Bergles, 1990).

5. CONCLUSIONS

For most heat transfer convection problems, once precise data on temperature profiles in the thermal layers are acquired, correlations between the heat transfer coefficients can readily be determined with limited additional effort. However, the main difficulty lies in the attainment of a precise temperature gradient at the surface, which should be measured without disturbing the thermal layer. The introduction of thermocouple probes into the thermal layer growing along a heated wall will result in significant flow and thermal disturbances. In this connection, optical techniques represent a useful tool for the study of thermal fields, since they are non-invasive and whole-field in character. Moreover, recent developments in image resolution and optical attachments as well as software and computer capabilities have made easy and relatively cheap the use of optical methods.

In this project the *liquid crystal* and the *schlieren* optical techniques have been applied to the problem of convective heat transfer in rib-roughened channels. This kind of geometry is encountered in several engineering problems, such as cooling of fuel elements in nuclear reactors, thermal control of gas turbine blades, and electronic equipment cooling. Therefore, there are strong motivations to carry out studies on this subject.

In *forced convection* problems, the use of artificially roughening the surfaces by repeated ribs to enhance heat transfer is an old practice. The phenomenon has been extensively studied in the past, mainly from the experimental point of view, and the most important conclusion was that great enhancements in heat transfer could be achieved by roughening the surfaces using appropriate rib dimensions and spacings. In this project, forced convection heat transfer in rib-roughened channels was experimentally investigated by using liquid crystal thermography. Numerous preliminary tests, conducted under different operating conditions, have shown the suitability of the method to analyse this heat transfer problem, in spite of the intrinsic complexity of the geometries investigated. The experimental uncertainty was found to be adequate for application to engineering problems. The results have confirmed the advantages, from the heat transfer point of view, of the use of rough heat transfer surfaces as an alternative to smooth surfaces. The majority of experiments have been

performed for channels in which the ribbed wall is not heated but acts as a promotor of turbulence in the air flow, in order to produce large heat transfer coefficients on the heated walls of the channel. This heat transfer problem has never been studied to date. The original results obtained illustrate the heat transfer modifications induced by the rib-roughened wall mounted normal to a heated flat plate, with heat transfer enhancements, relative to the case without the ribbed wall, locally larger than a factor of two.

In *natural convection* problems, the available literature seems somewhat contradictory about the possibility of enhancing heat transfer by the use of surface roughness elements. In addition, as compared to the abundant literature on forced convection in ribbed channels, relatively few studies exist on natural convection. Therefore, it is important to understand whether or not the ribs produce heat transfer enhancement and how the surface modifications act on heat transfer performance. It is of equal importance to understand the behaviour of rough surfaces on which the roughness occurs naturally, such as electronic circuit boards and microelectronic chip modules. To resolve these issues, natural convection in rib-roughened vertical channels has been experimentally studied by using the schlieren method. This technique has already been successfully applied by the author of this thesis to the study of other free convection phenomena and has been here improved in order to detect thermal gradients along arbitrary directions on the optical field. Optical data, processed by the original mathematical treatment, have permitted the heat transfer coefficient as well as the fluid temperature distributions to be reconstructed. It was found that the ribs, spaced according to a fixed pitch-to-height ratio, have significant effects on natural convection flows in vertical channels. The measurements have clearly established the reduction in heat transfer due to the presence of the ribs. The extent of the reduction is increased by smaller values of the channel aspect ratio. This is an important observation since the thermal design of electronic equipment is often based on the smooth plate correlations; neglecting the effect of the protrusions, which simulate the microelectronic chips, could lead to the underestimation of the working temperature of the components.

It can be concluded that this study has demonstrated the reliability of liquid crystal and schlieren techniques, separately applied to phenomena involving complex flow and thermal fields. However, heat transfer

investigation by these methods still represents an open-ended research area. The synergistic combination of optical techniques and increasingly sophisticated image processing systems will lead to further developments in experimental heat transfer.

REFERENCES

Acharya S., and Mehrotra A., (1993), Natural convection heat transfer in smooth and ribbed vertical channels, Int.J. Heat Mass Transfer, Vol.36, pp.236-241, 1993.

Akino N., Kunugi T., Ichimiya K., Mitsushiro K., and Ueda M., (1989), Improved liquid crystal thermometry excluding human colour sensation, ASME Journal of Heat Transfer, Vol.111, pp.558-565, 1989.

Aliaga D.A., Lamb J.P., and Klein D.E., (1994), Convection heat transfer distributions over plates with square ribs from infrared thermography measurements, Int.J. Heat Mass Transfer, Vol.37, pp.363-374, 1994.

Aytekin A., and Berger F.P., (1979), Turbulent flow in rectangular ducts with low aspect ratios having one rough wall, Nucl. Energy, Vol.18, pp.53-63, 1979.

Bar-Cohen A., and Rohsenow W.M., (1984), Thermally optimum spacing of vertical, natural convection cooled, parallel plates, ASME Journal of Heat Transfer, Vol.106, pp.116-123, 1984.

Bejan A., (1993), Heat Transfer, J.Wiley & Sons, New York, 1993.

Berger F.P., and Hau K.F., (1979), Local mass/heat transfer distribution on surface roughened with small square ribs, Int.J. Heat Mass Transfer, Vol.22, pp.1645-1656, 1979.

Bhavnani S.H., Bergles A.E., (1990), Effect of surface geometry and orientation on laminar natural convection heat transfer from a vertical flat plate with transverse roughness elements, Int.J. Heat Mass Transfer, Vol.33, pp.965-981, 1990.

Brauer H., (1961), Strömmungswiderstand und Wärmeubergang bei Ringsplaten mit Rohren, Atomkernenergie, Vol.4, pp.152-156, 1961.

Choi C.Y., and Ortega A., (1993), Mixed convection in an inclined channel with a discrete heat source, Int.J. Heat Mass Transfer, Vol.36, pp.3119-3134, 1993.

Ciofalo M., and Collins M.W., (1992), Large-eddy simulation of turbulent flow and heat transfer in plane and rib-roughened channels, Int.J. for Numerical Methods in Fluids, Vol.15, 1992.

Collins A.L., Collins M.W., and Hunter J, (1994), A novel tomographic approach for the data processing of limited-angle holographic interferograms for application to flow visualisation, Procs. 2nd Conf. on Optical Methods and Data Processing in Heat and Fluid Flow, London, U.K., 1994, pp.163-171.

Dalle Donne M., and Meerwald E., (1970), Heat transfer from surfaces roughened by thread-type ribs at high temperatures, Procs. 1970 Heat Transfer and Fluid Mechanics Institute, Stanford Univ. Press, Stanford, 1970.

Dalle Donne M., and Meyer L., (1977), Turbulent convective heat transfer from rough surfaces with two-dimensional rectangular ribs, Int.J. Heat Mass Transfer, Vol.20, pp.583-620, 1977.

Devia F., Milano G., and Tanda G., (1993), Evaluation of thermal field in buoyancy-induced flows by a schlieren method, Procs. III World Conf. on Experimental Heat Transfer, Fluid Mechanics and Thermodynamics, Honolulu, 1993, Vol.I, pp.823-830.

Devia F., Milano G., and Tanda G., (1994), Evaluation of thermal field in buoyancy-induced flows by a schlieren method, Exp. Thermal Fluid Science, Vol.8, pp.1-9, 1994.

Eckert E.R.G., and Jackson T.W., (1951), Analysis of turbulent free convection boundary layer on a flat plate, NACA Report No.1015, 1951.

Eckert E.R.G., and Goldstein R.J., (1976), Measurements in Heat Transfer, 2nd Ed., Hemisphere Publ.Corp., Washington, USA, 1976.

Faghri M., and Asako Y., (1994), Prediction of turbulent three-dimensional heat transfer of heated blocks using low-reynolds number two-equation model, Numerical Heat Transfer, Part A, Vol.26, pp.87-101, 1994.

Fann S., Yang W-J, and Zhang N., (1994), Local heat transfer in a rotating serpentine passage with rib-roughened surfaces, Int. J. Heat Mass Transfer, Vol.37, pp.217-228, 1994.

Fedynsky O.S., (1959), Intensification of heat transfer to water in annular channel. Collection of papers: problems of heat transfer, Energetich, pp. 53-66, Inst.Akad.Nuak SSSR, Moskow, 1959.

Fodemski T.R., and Collins M.W., (1988), Flow and heat transfer simulations for two- and three dimensional smooth and ribbed channels, Procs. 2nd UK Nat. Heat Transfer Conf., Glasgow, U.K., pp.845,860, 1988.

Foucault, L., (1859), Memoire sur la construction des Telescopes en verre argente, Ann. de l'Observatoire Imp. de Paris, Vol.5, pp.197-237, 1859.

Fujii T., Fujii M, and Takeuchi M., (1973) Influence of various surface roughness on the natural convection, Int.J. Heat Mass Transfer, Vol.16, pp.629-640, 1973.

Gomelauri V., (1964), Influence of two-dimensional artificial roughness on convective heat transfer, Int.J. Heat Mass Transfer, Vol.7, pp.653-663, 1964.

Hall W.B., (1958), Heat transfer in channels composed of rough and smooth surface, IGR-TN/W p.832, 1958.

Han J.C., (1984), Heat transfer and friction in channels with two opposite rib-roughened walls, ASME J. of Heat Transfer, Vol.106, pp.774-781, 1984.

Han J.C., Glicksman L.R., and Rohsenow W.M., (1978), An investigation of heat transfer and friction for rib-roughened surfaces, Int.J. Heat Mass Transfer, Vol.21, pp.1143-1156, 1978.

Han J.C., and Park J.S., (1988), Developing heat transfer in rectangular channels with rib turbulators, Int.J. Heat Mass Transfer, Vol.31, pp.183-195, 1988.

Hatton A.P., Quarmby. A., and Grundy I., (1964), Further calculations on the heat transfer with turbulent flow between parallel plates, Int.J. Heat Mass Transfer, Vol.7, pp.817-823, 1964.

Hauf W., and Grigull U., (1970), Optical methods in heat transfer, in Advances in Heat Transfer, Vol.6, Academic Press, New York, USA, 1970.

Heya N., Takeuchi M., and Fujii T., (1982), Influence of surface roughness on free convection heat transfer from a horizontal cylinder, J. Chem. Engng., Vol.23, pp.185-192, 1982.

Hiller W.J., and Kowalewski T.A., (1986), Simultaneous measurement of temperature and velocity fields in thermal convective flows, Procs. 4th Int. Symp. on Flow Visualisation, Paris, France, 1986.

Hong Y.-J., and Hsieh S.-S., (1993), Heat transfer and friction factor measurements in ducts with staggered and in-line ribs, ASME J.of Heat Transfer, Vol.115, pp.58-65, 1993.

Hung, Y.H., and Lin H.H., (1992), An effective installation of turbulence promoters for heat transfer augmentation in a vertical rib-heated channel, Int.J. Heat Mass Transfer, Vol.35, pp.29-42, 1992.

Ireland P.T., and Jones T.V., (1986), Detailed measurements of heat transfer on and around a pedestal in fully developed passage flow, Procs. 8th Int.Heat Transfer Conf., San Francisco, USA, 1986, Vol.3, pp.975-980.

Jofre R.J., and Barron R.F., (1967), Free convection heat transfer to a rough plate, ASME Paper No. 67-WA/HT-38, 1967.

Jones T.V., (1981), The use of liquid crystals in aerodynamic heat transfer testing, Procs. 4th Int. Symp. on Transport Phenomena in Heat and Mass Transfer, Sydney, Australia, 1991, Vol.4, pp.1199-1230.

Kattchee N., and Mackiewicz W.V., (1963), Effects of boundary layer turbulent promoters on the local film coefficient of ML1 fuel elements, Nucl.Sci.Engng., Vol.16, pp.31-38, 1963.

Kjellström B., and Hedberg S., (1966), On shear stress distribution for flow in smooth or partially rough annuli, Report AE-243 AB Atomenergi, 1966.

Lee B.K., Cho N.K., and Choi Y.D., (1988), Analysis of periodically fully developed turbulent flow and heat transfer by k-ε equation model in artificially roughened annulus, Int.J. Heat Mass Transfer, Vol.31, pp.1797-1806, 1988.

Lewis M.J., (1975), An elementary analysis for predicting the momentum and heat transfer characteristics of a hydraulically rough surface, ASME J.of Heat Transfer, Vol.97, pp.249-254, 1975.

Liou T.-M., and Hwang J.-H., (1993), Effect of ridge shapes on turbulent heat transfer and friction in a rectangular channel, Int.J. Heat Mass Transfer, Vol.36, pp.931-940, 1993.

Lockett, J.F., and Collins, M.W., (1990), Holographic interferometry applied to rib-rougheness heat transfer in turbulent flow, Int.J. Heat Mass Transfer, Vol.33, pp.2439-2449, 1990.

McAdams, W.H., (1954), Heat Transmission, 3rd Edn., Mc-Graw-Hill, New York, USA, 1954.

Maubach, K., (1969), Reibungsgesetze turbulenter Strömungen in geschlossenen glatten und rauhen Kanälen von beliebigem Querschnitt, Externer Bericht INR-4/69-22, Kernforschungszentrum Karlsruhe, BRD, 1969.

Maubach, K., (1972), Rough annulus pressure drop. Interpretation of experiments and recalculation for square ribs, Int.J. Heat Mass Transfer, Vol.15, pp.2489-2498, 1972.

Meerwald E., (1971), Druckverlust und Wärmeubergang an glatten und rauhen Flächen bei hohen Temperaturen und turbulenter Strömung und deren Darstellung durch universelle Gesetze, Externer Bericht INR-4/71-29,Kernforschungszentrum Karlsruhe, BRD, 1971.

Merzkirch W., (1974), Flow Visualization, Academic Press, New York, USA, 1974.

Michael Y.C., and Yang K.T., (1992), Three-dimensional Mach-Zehnder interferometric tomography of the Rayleigh-B nard problem, ASME Journal of Heat Transfer, Vol.114, pp.622-629, 1992.

Moffat, R.J., (1988), Describing the uncertainties in experimental results, Exp.Thermal Fluid Science, Vol.1, pp.3-17, 1988.

Myrum T.A., Qiu X., and Acharya S., (1993), Heat transfer enhancement in a ribbed duct using vortex generators, Int.J. Heat Mass Transfer, Vol.36, pp. 3497-3508, 1993.

Nunner W., (1956), Wärmeubertragung und Druckabfall in rauhen Rohren, VDI-Forsch., pp.455, 1956.

Ostrach S., (1953), An analysis of laminar free-convection flow and heat transfer about a flat plate parallel to the direction of the generating body force, NACA Report No.1111, 1953.

Ramakrishna K., Seetharamu K.N., and Sarma P.K., (1978), Turbulent heat transfer from a rough surface, ASME J. of Heat Transfer, Vol.100, pp.727-729, 1978.

Rowley G.J., and Patankar S.V., (1984), Analysis of laminar flow and heat transfer in tubes with internal circumferential fins, Int.J. Heat Mass Transfer, Vol.27, pp.553-560, 1984.

Settles G.S., (1985), Colour-coding schlieren techniques for the optical study of heat and fluid flow, Int.J. Heat Fluid Flow, Vol.6, pp.3-15,1985.

Sparrow E.M., and Azevedo L.F.A., (1985), Vertical-channel natural convection spanning between the fully developed limit and the single plate boundary-layer limit, Int.J. Heat Mass Transfer, Vol.21, pp.1847-1857, 1985.

Sparrow E.M., Chrysler G.M., and Azevedo L.F.A., (1984), Observed flow reversals and measured-predicted Nusselt numbers for natural convection in a one-sided heated vertical channel, ASME Journal of Heat Transfer, Vol.106, pp.325-332, 1984.

Sparrow E.M., and Tao W.Q., (1983), Enhanced heat transfer in a flat rectangular duct with sreamwise-periodic disturbances at one principal wall, ASME Journal of Heat Transfer, Vol.105, pp.851-861, 1983.

Stasiek J., (1992), Liquid crystal thermography and image processing in heat and fluid flow experiments, PhD thesis, City University, London, 1992.

Takase K., Hino R., Miyamoto Y., and Akino N., (1994), Experimental and numerical studies on heat transfer and flow characteristics of a fuel rod with transverse square ribs, Procs. 10th Int. Heat Transfer Conference, Brighton, UK, 1994, Vol.5, pp.245-250.

Tanaka T., (1988), Visualisation of the temperature field in thermal storage tanks by using the thermosensitive liquid crystal suspension method, Procs. Int. Symp. on Fluid Control, Measurement, Mechanics and Flow Visualisation, Sheffield, U.K., 1988, pp.212-215.

Tanda G., (1987), Analisi numerica della convezione naturale in regime laminare all'interno di canali verticali riscaldati, Pubblicazioni del Dipartimento di Ingegneria Energetica, Report DINE-EGR/11, Genova, 1987.

Tanda G., (1988), Natural convection in partially heated vertical channels, Wärme- und Stoffubertragung, Vol.23, pp.307-312, 1988.

Tanda G., (1992,a), Sulla valutazione del coefficiente di scambio termico per convezione con tecniche ottiche. Il metodo schlieren, Pubblicazioni del Dipartimento di Ingegneria Energetica, Report DINE-EGR/18, Genova, 1992.

Tanda G., (1992,b), Studio sperimentale dello scambio termico per convezione naturale in un sistema di piastre verticali sfalsate, Procs. X Italian Heat Transfer Conf. (U.I.T.), Genova, 1992, pp.189-200.

Tanda G., (1993,a), Studio sperimentale sulla refrigerazione per convezione naturale di due piastre verticali sfalsate, Procs. II Italian Conf. on Thermal Control of Electronic Equipment (A.S.T.E.), Genova, 1993, pp.1-16.

Tanda G., (1993,b), Natural convection heat transfer from a staggered vertical plate array, ASME Journal of Heat Transfer, Vol.115, pp.938-945, 1993.

Tanda G., (1995), Experiments on natural convection from two staggered vertical plates, Int.J. Heat Mass Transfer, Vol.38, pp.533-543, 1995.

Thomas L., (1980), Fundamentals of heat transfer, Prentice-Hall, N.J., USA, 1980.

Tiggelbeck S., Mitra N.K., and Fiebig M., (1991), Flow structure and heat transfer on a channel wall with multiple longitudinal vortex generators, Procs. 2nd World Conf. on Exp.Heat Transfer, Fluid Mech., and Thermodyn., Dubrovnik, Croatia, 1991, pp.126-133.

Töpler A.,(1864), Beobachtungen nach Einer Nueun Optischen Methode, M.Cohen & Son Pub., Bonn, Germany, 1864.

Vasil'ev L.A., (1971), Schlieren Methods, Keter Inc., New York, 1971.

Walklate P.J., (1983) A holographic technique for the study of heat transfer from a rib-roughened surface, Procs. 3rd Int.Symp. on Flow Visualization, University of Ann Arbor, 1983.

Warburton C., and Pirie M. A. M., (1973), An improved method for analysing heat transfer and pressure drop tests on roughened rods in smooth channels, CEGB RD/B/N 2621, Berkeley Nuclear Laboratories, 1973.

Watts J., and Williams F., (1981), A technique for the measurement of local heat transfer coefficients using copper foil, CEGB RD/B/5023/N81, Berkeley Nuclear Laboratories, 1981.

Webb B.W., and Hill D.P., (1989), High Rayleigh number laminar natural convection in an asymmetrically heated vertical channel, ASME Journal of Heat Transfer, Vol.111, pp.649-656, 1989.

Webb R.L., Eckert E.R.G., and Goldstein R.J., (1971), Heat transfer and friction in tubes with repeated-rib roughness, Int.J. Heat Mass Transfer, Vol.14, pp.601-617, 1971.

Wilkes N.S., (1980), Prediction of the turbulent fluid flow through a channel with rib roughened surfaces, Harwell Report AERE-R 9874, 1980.

Wilkie D., (1966,a), Forced convection heat transfer from surfaces roughened by transverse ribs, Procs. 3rd Int. Heat Transfer Conference, Chicago, USA, 1966, Vol.1, pp.1-19, 1966.

Wilkie D., (1966,b), Calculation of heat transfer and flow resistance of rough and smooth surfaces contained in a single passage, Procs. 3rd Int. Heat Transfer Conference, Chicago, USA, 1966, Vol.1, pp.20-31.

Wilkie D., Cowin M., Burnet P., and Bugoyne, T., (1967),Friction factor measurements in a rectangular channel with walls of identical and non-identical roughness, Int.J. Heat Mass Transfer, Vol.10, pp.611-621, 1967.

Williams F., and Watts J., (1970), The development of rough surfaces with improved heat transfer performance and a study of the mechanisms involved, Procs. 4th Int. Heat Transfer Conference, Versailles, France, 1970, Vol.2, pp.1-11.

Zhang Y.M., Gu W.Z., and Han J.C., (1994), Heat transfer and friction in rectangular channels with ribbed or ribbed-grooved walls, ASME J.of Heat Transfer, Vol.116, pp.58-65, 1994.

Zhu J.X., Fiebig M., and Mitra N.K., (1995), Numerical investigation of turbulent flows and heat transfer in a rib-roughened channel with longitudinal vortex generators, Int.J. Heat Mass Transfer, Vol.38, pp.495-501, 1995.

APPENDIX A1) Liquid crystal thermography

A1.1 Theory

The distribution of the colour component pattern on a liquid crystal layer is related to the thermal field. Recording the colour pattern by a RGB video camera and converting the stored image to the HSI (Hue, Saturation, Intensity) domain allows one to reconstruct the isotherm lines within the colour play interval of liquid crystals. During experiments, a uniform wall temperature condition is imposed on the bottom side of the test plate, while the top side (coated by the liquid crystal sheet) exchanges heat by forced convection with air (Fig.A1.1). If $T_{s,w}$ and $T_{s,a}$ denote respectively the surface temperatures of the test plate on the water side (bottom surface) and on the air side (top surface), the local specific heat flux q across the test plate is given by

$$q = (T_{s,w} - T_{s,a}) \cdot C_{tp} \qquad (A1.1)$$

Here C_{tp} represents the thermal conductance (per unit heat transfer area) of the test plate, composed of 8 mm of perspex plus 0.15 mm of LC sheet. In Eq.(A1.1) the assumption of heat flux lines normal to the test plate surfaces has been made. Since temperature gradients normal to the flat plate are much larger than those occurring in the plane of the test plate, the assumption is expected to be well satisfied. The definition of the heat transfer coefficient h is now introduced

$$h = q \,/\, (T_{s,a} - T_{air}) \qquad (A1.2)$$

where T_{air} is a convenient air temperature, here assumed to be the mean temperature of the flowing air measured at the inlet of the test section.

The heat transfer coefficient can be recast in dimensionless form by using the hydraulic diameter of the tunnel (d=0.0896m) and the thermal conductivity of air k_{air}:

$$Nu = h\, d/k_{air} \qquad (A1.3)$$

where Nu is the local Nusselt number.

A further dimensionless parameter is given by the Reynolds number:

$$Re = w_{max}\, d/\nu_{air} \qquad (A1.4)$$

where w_{max} and ν_{air} are the maximum air velocity (measured at the centre of

the test section inlet) and the air kinematic viscosity, respectively.

Turning to the Nusselt number, by combining Eqs (A1.1),(A1.2), and (A1.3) one obtains:

$$Nu=[(T_{s,w}-T_{s,a})/(T_{s,a}-T_{air})]\cdot C_{tp}\, d/k_{air} \qquad (A1.5)$$

Since thermal conductivities of perspex and air are fairly constant during experiments, Eq.(A1.5) can be written in the following form

$$Nu= (const.)\ x\ \theta \qquad (A1.6)$$

$$\theta= (T_{s,w}-T_{s,a})/(T_{s,a}-T_{air}) \qquad (A1.7)$$

The dimensionless temperature θ, related to the local Nusselt number through a constant proportionality factor, is obtained directly from experiments. In fact, T_{air} is recorded (by thermocouple) at the test section inlet, $T_{s,w}$ the mean value of thermocouples embedded in the perspex close to the water side of the test section and $T_{s,a}$ given by the liquid crystal colour pattern.

In principle, in order to map the lines at constant θ (or Nu), only one (true colour) liquid crystal image may be required. Processing that image in order to extract lines at constant $T_{s,a}$ enables the Nu contours on the wall to be determined. Unfortunately, the LC colour play interval is narrow and does not allow the simultaneous reconstruction of θ for the whole optical field. A technique for obtaining contours of θ between its minimum and maximum values consists of (a) processing only one colour band and (b) changing, in the course of an experiment at a given air flow rate, either the air temperature T_{air} or the water-side temperature $T_{s,w}$. If only one colour band is used, $T_{s,a}$ in Eq.(A1.7) is the surface temperature corresponding to the selected hue range. The procedure requires that the natural convection effects are negligible, that is the heat transfer coefficient is not affected by $(T_{s,a}-T_{air})$. This assumption is supported by the low values of Gr/Re^2 in the experiments, owing to the small temperature difference $(T_{s,a}-T_{air})$, usually few °C degrees, in presence of a turbulent (in the majority of tests) air flow.

In the experiments only the green band in the hue range between 45 and 55 has been chosen. Calibration gave the corresponding temperature as **32.1°C** ± 0.1°C. If the water-side temperature $T_{s,w}$ is progressively changed by adjusting the temperature of the thermostatic bath, T_{air} being held constant, and the green band contours ($T_{s,a}$=32.1°C) are recorded after the intermediate stationary states were reached, one can obtain lines at

constant θ over its range of variation. This procedure was termed ATF (Air Temperature Fixed). Alternatively, varying the air temperature T_{air}, and keeping $T_{s,w}$ and $T_{s,a}$=32.1°C fixed, leads to the same results for the WTF procedure (Water Temperature Fixed).

The technique of varying, step by step, either the water or the air temperature in order to map the θ contours for a given Re number was followed for the flat plate configuration as well as for the rib-roughened configurations R1 and R2. Since the latter configurations (R1 and R2) should be regarded as "enhanced" geometries (from the heat transfer point of view) with respect to the flat plate, an additional parameter can be introduced:

$$N = \theta/\theta_{fp} = Nu/Nu_{fp} \qquad (A1.8)$$

where the index $_{fp}$ denotes quantities referred to the flat plate configuration. The larger the value of N, the higher is the heat transfer enhancement achieved by introducing the ribs.

A1.2 Measurement of the thermal conductance of the test plate

The absolute Nusselt number evaluation requires the test plate thermal conductance C_{tp} to be evaluated. Since a one-dimensional conductive heat flux across the test plate occurs, the conductance C_{tp} can be measured in a separate apparatus. A one-dimensional conductive heat flux is imposed across a sample having the same composition and thickness as the test plate and measuring the extent of the heat flux and the temperature drop between the opposite sides.

To this end, a guarded hot plate apparatus has been constructed. A schematic view of the apparatus is presented in Fig.A1.2, together with a photograph illustrating the main components of the experimental setup (Fig.A1.3). The apparatus consists of two plates, the lower called the "hot plate" (an aluminium disk with a plane electric heater attached underneath) and the higher the "cold plate" (a brass plate with a serpentine fitted inside through which a refrigerant fluid flows). The plates are instrumented with numerous thermocouples carefully located as close as possible to the plate surfaces in contact with the sample, and a guard plate (connected to an independent power supply) to minimise the heat losses.

During tests, a given amount of electrical current from the main power

supply was dissipated into the heater attached to the hot plate. The high conductivity of the aluminium allows a uniform hot plate temperature to be reached. At the same time, the cold plate was refrigerated by the flow rate of a given refrigerant coming from a thermostatic bath. The high conductivity of the brass and the significant thickness (1 cm) of the plate ensure a uniform cold plate temperature to be reached. The test sample is a 55 mm-dia. disk, 8.15 mm thick, (8 mm perspex plus 0.15 mm LC sheet) and sandwiched between the hot and cold plates. Care was taken to ensure a perfect thermal contact between the sample and the plates. The guard plate was heated (by the second power supply) in order to establish a zero temperature drop between the guard and the hot plates. These conditions ensure that the power input to the hot plate crosses the sample by one-dimensional conduction and is transferred to the cold plate. A lateral insulation (a 2 cm-thick ring of expanded-extrudate polystyrene, k=0.03 W/mK) of the sample was introduced to minimise radial conductive losses to the ambient air. As a consequence of the overall design, at steady state, the computation of the thermal conductance of the sample may be made from the relationship:

$$C_{tp} = Q / [A (T_h - T_c)] \qquad (A1.9)$$

where T_h and T_c represent the hot plate and cold plate temperatures respectively. The latter are measured as close as possible to the sample surfaces. A is the surface area of the sample ($=\pi/4 \times 0.055^2$ m^2), while Q is the electric power dissipated in the main heater, from which radiant conductive losses must be subtracted. Conductive losses through the lateral insulation depend on the difference between the mean temperature of the sample and the air ambient temperature; their extent can be evaluated by means of a simple model. During the majority of tests, their contribution was in the range 0-3.5%. The hot plate temperature T_h was evaluated by means of three fine-gauge, type T thermocouples, embedded in three small grooves machined on the aluminium surface in contact with the sample. After the thermocouples have been fitted in the plate, the surface was made perfectly plane. The cold plate temperature T_c was measured by means of two fine-gauge, type T thermocouples attached to the surface in contact with the sample, with the same method for the hot plate. All the thermocouples were connected to a Keithley 9-channel digital thermometer and calibrated to ±0.1 K. During tests, thermocouples deployed along the hot plate (as well as those along the cold plate) were in agreement with each other

within 0.1 K. Finally, the power supplied to the main heater was evaluated by means of the voltage across the heater and its electric resistance.

The error analysis conducted by means of error propagation theory led to a (20/1) uncertainty of 5% for the thermal conductance.

The measurement of C_{tp} was performed by imposing thermal conditions as close as possible to those occurring in the liquid crystal experiments. Therefore, repeated tests were conducted with a mean temperature of the test sample (= 1/2 (T_h+T_c)) around 35 °C.

The tests were performed with a range of temperature drops across the sample. Results for four tests are presented in Table A1.1.

	Test No.1	No.2	No.3	No.4
T_h ,°C	45.25	42.1	37.6	38.4
T_c ,°C	24.25	27.95	23.0	32.1
(T_h-T_c),°C	21.00	14.15	14.6	6.3
$Q_{electric}$,W	1.295	0.857	0.872	0.400
losses (estim.),W	0.029	0.029	0.019	0.029
losses ,%	2.2%	3.3%	2.2%	7.2%
Q ,W	1.266	0.828	0.853	0.371
$(T_h+T_c)/2$,°C	34.75	35.0	30.3	35.25
C_{tp} W/m^2K	25.37	24.63	24.59	24.79
$C_{tp\,(average)}$		24.84 W/m^2K		

TABLE A1.1 Results of thermal conductance measurements

From the thermal conductance C_{tp}, the apparent thermal conductivity of the test plate can be deduced:

$$k_{tp} = C_{tp}\, t_{tp} \qquad \text{(A1.10)}$$

where t_{tp} is the overall thickness of the sample (=0.00815 m). The apparent thermal conductivity turned out to be 0.202 W/mK, very close to the value reported in textbooks for perspex (k=0.184 W/mK at 20°C, Bejan, 1993).

A1.3 Error analysis

According to the procedure outlined by Moffat (1988), the experimental uncertainty δX of a quantity X, assumed to be a function of several variables $x_1, x_2, \ldots x_N$, can be estimated using a root-sum-square combination:

$$\delta X = [\ \Sigma_{i=1}^{N} (\partial X/\partial x_i)^2 (\delta x_i)^2\ ]^{1/2} \qquad \text{(A1.11)}$$

δx_i being the uncertainty (conventionally at the 95% confidence level) in the generic variable x_i. Equation (A1.11) can be rewritten in a different form when X is given as a product of variables and the uncertainties δx_i are known as percentages of x_i:

$$X = x_1^{a1} \cdot x_2^{a2} \cdot x_3^{a3} \cdot \ \cdots\ \cdot x_N^{aN} \qquad \text{(A1.12)}$$

$$\delta X/X = [\ \Sigma_{i=1}^{N} (a_i)^2 (\delta x_i/x_i)^2\ ]^{1/2}$$

The uncertainty δx_i in the generic variable x_i has to take into account the components associated with fixed errors ($\delta x_{i,fix}$) and with random errors ($\delta x_{i,rnd}$) as follows:

$$\delta x_i = [\ (\delta x_{i,fix})^2 + (\delta x_{i,rnd})^2\ ]^{1/2} \qquad \text{(A1.13)}$$

Variables for which the uncertainty evaluation is of great importance are θ, Nu and Re. The calculation of uncertainty is based on experiments performed by imposing an upward heat flux across the test plate and keeping the air temperature fixed (HFU + ATF procedures) since the majority of tests were conducted under these conditions.

θ is directly related to temperature measurement since it is equal to $(T_{s,w} - T_{s,a})/(T_{s,a} - T_{air})$. T_{air} is measured by means of thermocouples calibrated to ± 0.1°C (fixed errors). An additional 0.1°C-uncertainty can be ascribed to random errors. Since the inlet air temperature is not strictly uniform, the extent of temperature non-uniformity can be interpreted as an additional uncertainty (about 0.5°C). Errors in $T_{s,w}$ take into account the uncertainty in thermocouple readings (0.1°C fixed and 0.1°C random) and the departure from isothermal conditions on the water-side of the test plate. The latter contribution was estimated by recording $T_{s,w}$ at several points and evaluating the maximum surface

temperature non-uniformity relative to the mean value. This term can be expressed for the majority of experiments as a percentage (about 7%) of the $(T_{s,w}-T_{s,a})$ temperature drop and was considered to be a fixed error because, if occurred, it had a systematic influence on the result. Finally, the liquid-crystal reference temperature $T_{s,a}$ was assumed to be affected by uncertainties equal to 0.1°C both for fixed and random errors. It is apparent that the large uncertainties are associated with regions where the temperature differences $(T_{s,w}-T_{s,a})$ and $(T_{s,a}-T_{air})$ are small. While $(T_{s,a}-T_{air})$ was fairly constant in the experiments (4-5°C), the extent of $(T_{s,w}-T_{s,a})$ depends on the local heat transfer rate. If the law of the error propagation (A1.12) is applied, one obtains:

Low Reynolds number (Re=3500) $\quad \delta\theta/\theta = 17.4\text{-}19.5$ %

High Reynolds number (Re=20000) $\quad \delta\theta/\theta = 13.0\text{-}13.4$ %

The Reynolds number affects the value of θ-uncertainty since heat transfer increases with Re. In addition, at a given Re, regions with higher local heat transfer coefficients are characterised by a lower θ-uncertainty.

The relationship between Nusselt number and θ is expressed by Eq.(A1.5). Under the hypothesis of heat transfer propagation only in the direction normal to the test plate, the uncertainty in Nu value is mainly affected by uncertainties in the θ value (reported above) and in the C_{tp} value (5%). It follows that:

Low Reynolds number (Re=3500) $\quad \delta Nu/Nu = 18.1\text{-}20.1$ %

High Reynolds number (Re=20000) $\quad \delta Nu/Nu = 13.9\text{-}14.3$ %

When the ratio N between Nu values for the test plate with and without ribs is evaluated, the overall error in N is expected to be reduced. In fact, the systematic components of errors in Nusselt values play the same role for the ribbed and unribbed configuration experiment. It means that if Nu (with ribs) and Nu_{fp} (without ribs) are both systematically estimated in excess by 15%, for instance, their ratio is unaffected by the systematic error. When this consideration is applied to the estimate of uncertainty in N values, $\delta N/N$ is determined to vary between 11 and 16% at low Re (3500) and to be 7% at high Re (20000).

Finally, the uncertainty in Re values, estimated on the basis of the errors associated with the velocity probes, was found to be 14%.

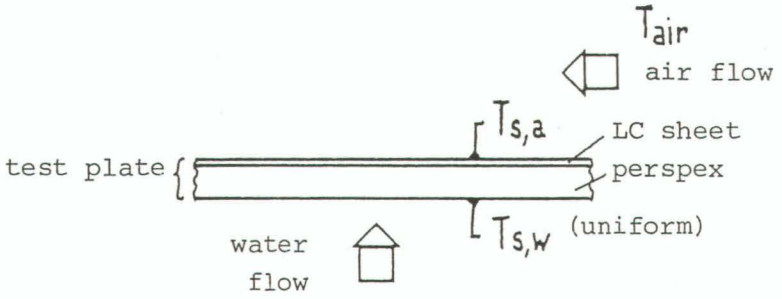

FIGURE A1.1 Sketch of the heat transfer mechanism through the test plate.

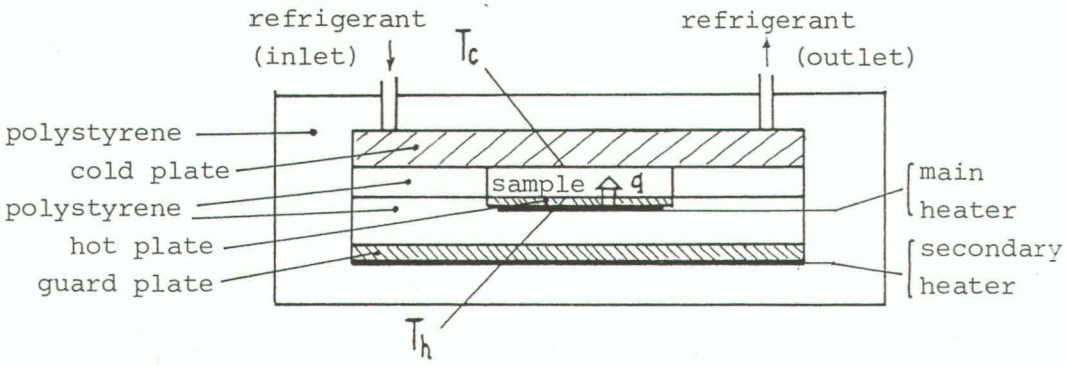

FIGURE A1.2 Schematic of the apparatus for the measurement of the thermal conductance of the test plate.

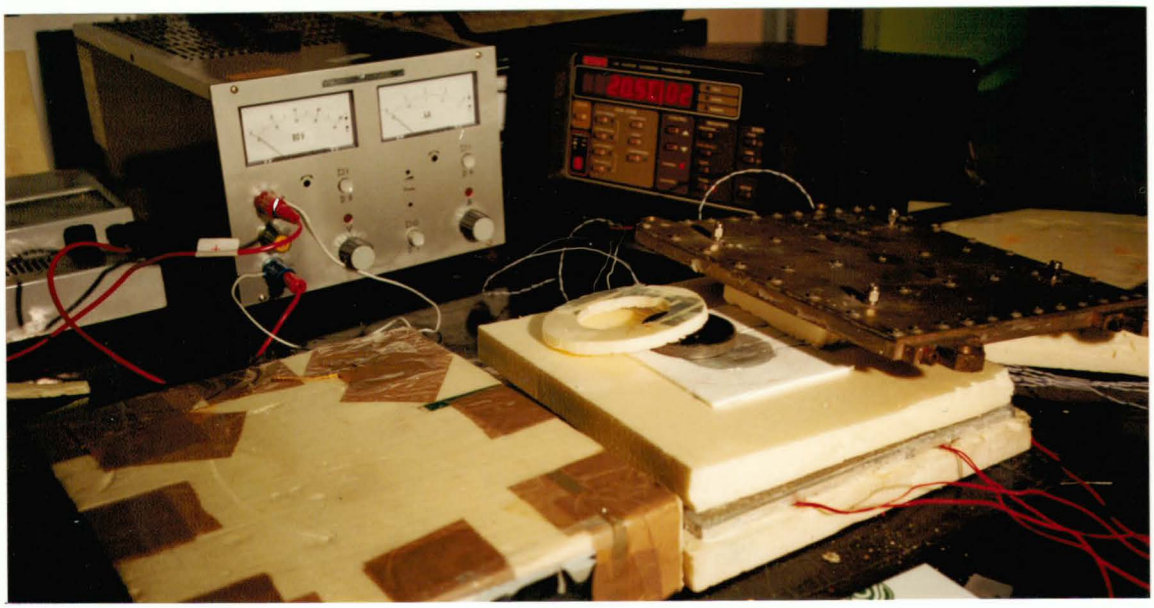

FIGURE A1.3 Photograph of the experimental apparatus for C_{tp} measurements

APPENDIX A2 The schlieren method

A2.1 Theory

The schlieren optical system is based on deflection of light occurring when a beam travels through a non-isothermal transparent medium. With reference to the schlieren arrangement sketched in Fig.A2.1, owing to inhomogeneities along the y direction, a light ray travelling along the z-direction is deflected by an angle α_y. The relation between the angular deflection and the refractive index gradient of fluid $\partial n/\partial y$ has been proved in Paragraph 2.3.2 to be:

$$\alpha_y = \frac{1}{n_o}\frac{\partial n}{\partial y} L \qquad (A2.1)$$

where n_o is the refractive index of air at reference conditions and L is the length (along z) of the disturbed region. Use of Eq.(A2.1) implies that the thermal field should be two-dimensional (i.e. independent of the z-coordinate). This condition is assumed to be well satisfied in the experiments, because of the low non-uniformity in temperature of the heated plates and the large ratio of the plate length to the channel spacing. By introducing the Gladstone-Dale formula ($n = C\rho+1$) and the state equation of the ideal gas ($\rho=P/RT$), one obtains

$$\alpha_y = -\left(\frac{C\,P\,L}{R\,n_o}\right)\frac{1}{T^2}(\partial T/\partial y) \qquad (A2.2)$$

where C is the Gladstone-Dale constant of air, P the pressure (whose variations near the test section are assumed to be negligible) and R the gas constant of air. Since the light ray shift Δ_y, recorded at the focal plane of mirror M_2, is equal to $f_2 \cdot \alpha_y$, it follows that

$$\Delta_y = -f_2\left(\frac{C\,L}{R\,n_o}\right)\frac{P}{T^2}(\partial T/\partial y) = \frac{\Omega}{T^2}(\partial T/\partial y) \qquad (A2.3)$$

in which the constant Ω is equal to $-0.0456 m^2 K$ in the present experiment.

Applying the same considerations to deflections occurring in the x-z plane leads to

$$\Delta_x = -f_2\left(\frac{C\,L}{R\,n_o}\right)\frac{P}{T^2}(\partial T/\partial x) = \frac{\Omega}{T^2}(\partial T/\partial x) \qquad (A2.4)$$

Attention is now turned to the deflection of rays passing in the vicinity of heated walls, recorded in the direction normal to the surface orientation. The deviation at the surface Δ_w can be determined by collimating the centreline of the filament shadow (projected onto the screen) on the point of the surface profile at which the measurement has to be performed. This is shown in Fig.A2.2. Since the focal filament is connected to a micrometer, the displacement of the filament (equal to Δ_w) can be easily obtained. It follows that:

$$\Delta_w = \Omega \, (\partial T/\partial n)_w / T_w^2 \qquad (A2.5)$$

where $(\partial T/\partial n)_w$ is the temperature gradient in the direction normal to the plate surface and evaluated at the wall, and T_w is the wall temperature. By introducing the definition of local heat transfer coefficient

$$h = \frac{-k_w (\partial T/\partial n)_w}{(T_w - T_{air})} \qquad (A2.6)$$

where k_w is the thermal conductivity of the fluid at the surface temperature and T_{air} is the ambient air temperature, it follows that

$$h = -k_w \Delta_w T_w^2 / (\Omega \, (T_w - T_{air})) \qquad (A2.7)$$

A2.2 Thermal field reconstruction

In order to reconstruct the temperature distribution in the optical field for a given experiment, the following steps are required:

- images corresponding to the same test but recorded for different positions of the focal filament (i.e. different light deviation Δ values) have to be superimposed to obtain the pattern of Δ lines, as shown in Fig. A2.3;
- from the distribution of Δ values, the function T(x,y) is obtained from the equation:

$$\Delta_\xi = \Omega \, (\partial T/\partial \xi)/T^2 \qquad (A2.8)$$

where ξ is the line along which the T(x,y) reconstruction is performed. For example, Fig. A2.4 schematically shows the temperature reconstruction along a line at constant x, by using information on Δ_y only. This operation requires a mathematical treatment of optical data. Two procedures can be

followed: (i) the direct integration of Eq.(A2.8), (ii) the application of an inverse technique.

(i) Direct integration

Equation (A2.8) can be easily integrated (for instance along lines at constant x) by separating the variables and obtaining:

$$T = [\ 1/T_{\xi=0} - (\ \int_0^{\xi} \Delta_{\xi}\, d\xi\ )/\Omega\ ]^{-1} \qquad (A2.9)$$

where $T_{\xi=0}$ is the boundary condition, for instance the known temperature at the wall. If the function Δ_{ξ} is known with high precision at several points close to each other, Eq.(A2.9) provides the solution with great accuracy, as the only (numerical) error is due to the kind of discretised algorithm adopted for the integration of Δ_{ξ}. If, on the contrary, the values of Δ_{ξ} are perturbed by noise, as always occurs in experimental tests, and/or optical data are available at a limited number of points, the accuracy of the direct integrating technique may be poor. For instance, this may occurs when Eq.(A2.9) is used to derive the temperature "at the infinite" (i.e. at large distances from ξ=0). In such cases, a different mathematical procedure based on the inverse technique can be preferred.

(ii) Iterative inverse technique (OLS method)

If the measured and calculated displacement of light rays are denoted by Δ_m and Δ_c, for the solution of the inverse problem in the OLS formulation it is necessary to find a vector of unknown temperature $\mathbf{T} = \{T_i\}_{i=1,N}$ which minimises the sum:

$$S_N = [\ \Delta_m - \Delta_c(T)\ ]^t \cdot [\ \Delta_m - \Delta_c(T)\ ] \Rightarrow \min \qquad (A2.10)$$

where N is the total number of measured light deflections and $[\ ]^t$ denotes the transposition operator. The calculated displacement is given by:

$$\Delta_c(T) = \Omega \cdot (\partial T/\partial \xi)/T^2 \qquad (A2.11)$$

and the unknown vector of parameters **T** is subjected to some constraints by using appropriate thermal boundary conditions, which depend on the kind of each convective experiment. As the calculated function Δ_c is a nonlinear function of T, the minimisation process has been constructed with successive approximations using recursively the linearised Gauss algorithm. In vectorial form the iterative process at the generic iteration k+1 can be

written:

$$\mathbf{T}^{k+1} = \mathbf{T}^{k} - \frac{1}{2}\,\mathbf{P}^{k}\,\mathrm{grad}\{S_N^k\} \qquad \text{(A2.12)}$$

and stops when the minimum values of the target functional s is reached. In Eq.(A2.12), the gradient of S_N and the var/covar matrix **P** at the generic iteration k can be determined as follows:

$$\mathrm{grad}\{S_N\} = -2\,\mathbf{X}^{t}\cdot[\Delta_m - \Delta_c] \qquad \text{(A2.13)}$$

$$\mathbf{P} = [\mathbf{X}^{t}\cdot\mathbf{X}]^{-1} \qquad \text{(A2.14)}$$

where **X** is the sensitivity matrix of Δ_c with respect to the parameters $\{T_i\}$ at the measuring points ξ_i (i=1,N).

It can be seen from Eq.(A2.11) that in order to calculate the function Δ_c, temperature and temperature gradients of the fluid must be evaluated. This can be accomplished by assuming that the unknown temperature distribution $T(\xi)$ along the ξ-line is represented by a proper class of functions, for example polynomial approximations, cubic B-splines, etc. In this work, a simple local, second-order, three points, polynomial approximation has been chosen:

$$T = T_i + a(\xi-\xi_i) + b(\xi-\xi_i)^2 \qquad \text{(A2.15)}$$

where the subscript i=1,N refers to each of the N measured light deflection data and

$$a = (T_{i+1}\delta_i^2 + T_i(\delta_{i+1}^2 - \delta_i^2) - T_{i-1}\delta_{i+1}^2)/c$$

$$b = (T_{i+1}\delta_i - T_i(\delta_{i+1}+\delta_i) + T_{i-1}\delta_{i+1})/c$$

$$c = \delta_i\delta_{i+1}(\delta_i+\delta_{i+1})$$

In the above relationships, the quantity δ indicates the distance between two adjacent iso-deflection lines, namely $\delta_i=\xi_i-\xi_{i-1}$ and $\delta_{i+1}=\xi_{i+1}-\xi_i$. This way, the unknown temperature function $T(\xi)$ is parameterised by a moving parabola, and the derivative $\partial T/\partial\xi$ can be easily calculated by using a central formula of second order accuracy. The sensitivity matrix **X** and therefore the var/covar matrix **P** and the quantity $\mathrm{grad}\{S_N\}$ can be calculated too, making the iterative solution of Eq.(A2.12) possible.

Several simulated tests have shown that the above formulation is able to reconstruct the temperature field and estimate the heat transfer

coefficient at the wall from noisy measured optical data (Devia, Milano and Tanda, 1993, 1994). In the above references, comparisons between results obtained from the two reconstruction method are reported for laminar free convection on a vertical plate.

The thermal field reconstruction from optical data can be performed manually or automatically. The **manual procedure** requires firstly the assembly of schlieren images for a given experiment. Projecting the sequence of images (slides) onto a screen and marking on a transparent paper the position of filament shadow centrelines enable the light deviation pattern to be obtained. Then, once the line of integration has been chosen, the distribution of light deviation along it has to be extracted by measuring the distances from the intercepts to a reference point (the wall, for instance) and taking into account the magnification factor between the real scale and the image plotted on the paper. Finally, light deviation data and their coordinates are the input data for the computer programme which reconstructs the temperature profile by direct integration or by the inverse technique. The whole procedure has to be repeated along all ξ-lines of interest in the optical field. Therefore, the complete analysis of a given experiment may be time-consuming, typically occupying one or two full days' work by one person. In the **automatic mode** the sequence of schlieren images is transferred from a videotape to a desk-top computer through a Microeye IC Full Colour Video Digitiser. Even though the Microeye card allows one to digitise images with 256 colours, optimum results were obtained by transferring the images in the black-and-white format. After the digitising operation, each image is filtered and compressed. Then, the coordinates of the filament shadow centreline are identified. Once each single image has been treated, they are superimposed by a special algorithm which makes it possible to avoid misalignments of images. The final step is the selection of the lines along which the temperature profile has to be reconstructed. This operation is performed by fixing the extrema of integration of Eq.(A2.8) by the "mouse" of the computer on the image of the optical field plotted onto the computer screen. When the choice is completed, the mathematic routine provides for the elaboration of optical data and the supply, by numerical and graphical means, of the temperature distribution. Fig.(A2.5) gives a sample illustration of a printed copy of the screen at the end of the automatic procedure. Most of the computer programs used in the automatic temperature

reconstruction are not commercially available but have been self-written (in Quick-basic language) by the author of this project.

A2.3 Data reduction

As previously explained, the local heat transfer coefficient h can be obtained by means of optical measurements, according to Eq.A2.7. Further variables can be obtained by heat flux and temperature measurements. For the heated plate assembly the energy balance leads to

$$Q_{el} = Q + Q_r \tag{A2.16}$$

where Q_{el}, Q, and Q_r denote, respectively, the electrical power input, the convective heat transfer, and the radiant heat transfer. Q can be determined by using the measured value of Q_{el} and the calculated value of Q_r. The average heat transfer coefficient per-plate was evaluated from:

$$h_{av} = Q / [A\ (T_w - T_{air})] \tag{A2.17}$$

In the above equation A is the plate surface area, T_w is the surface temperature and T_{air} the ambient air temperature. The surface temperature T_w of the heated plate was evaluated by averaging the readings of the thermocouples embedded in the wall. Similarly, the ambient temperature T_{air} was obtained by averaging the readings of the thermocouples deployed below the plate assembly.

For a dimensionless presentation, measured data were recast in a dimensionless form by introducing Rayleigh and Nusselt numbers and a scale temperature function:

$$Nu = h\ H/k \tag{A2.18}$$

$$Nu_{av} = h_{av} H/k \tag{A2.19}$$

$$Ra = g\beta\rho^2(T_w - T_{air})H^3Pr/\mu^2 \tag{A2.20}$$

$$\theta = (T - T_{air})/(T_w - T_{air}) \tag{A2.21}$$

The thermophysical properties of the fluid appearing in Eqs.(A2.18-A2.20) were evaluated at the film temperature $(T_w + T_{air})/2$. For the purpose of comparing with the published data, heat transfer quantities are sometimes expressed using characteristic lengths which differ from the channel height

H. For instance, a subscript x is introduced when the local Nusselt number $Nu_x = h\,x/k$ and the Rayleigh number Ra_x $(=g\beta\rho^2(T_w-T_{air})x^3Pr/\mu^2)$ are referred to the vertical coordinate x as characteristic length. The subscript m denotes the modified (overall) Nusselt number $Nu_m = h_{av}S/k$, (characteristic length S) and the modified Rayleigh number $Ra_m = (S/H)g\beta\rho^2(T_w-T_{air})S^3Pr/\mu^2 = Ra(S/H)^4$.

By means of the numerical integration of measured coefficients h along the heated surfaces (by Eq.A2.7) a mean value h_o can be obtained. Therefore, the overall heat transfer coefficient of the heated plate assembly can be estimated from the energy balance (h_{av}) as well as by the integration of local optical measurements (h_o). After runs, this quantity, estimated by using either 24 points (smooth plate assembly) or 140 points (rough plate assembly) turned out to be only slightly different (0 to 6 percent) from the coefficient h_{av} introduced by Eq.(A2.17). The difference can be ascribed both to the experimental uncertainty of the two different evaluations and to the role played by the edge surfaces, for which a local measurement was not feasible.

A2.4 Error analysis

The uncertainty in the results (at 95 percent confidence level) was evaluated by using a root-square combination of the effects of each individual measurement, according to the procedures outlined by Moffat (1988) and briefly summarised in Paragraph A1.3. The uncertainty in each variable was estimated by evaluating the fixed error and the random error observed during running trials (33 observations with the apparatus at a steady state).

Uncertainties in the Rayleigh number Ra and the Nusselt number Nu_{av} are mainly affected by the uncertainty in (T_w-T_{air}) for the former, and by the uncertainties in (T_w-T_{air}) and Q for the latter. Since the wall temperature uniformity was good and the input power evaluation was very accurate, tolerances in Ra and Nu_{av} were reduced to a few percent (5 and 7%, respectively).

The accuracy of the optical measurements performed by the schlieren method is generally sensitive to the circumstances involved. These include dimensions of optical components and their alignment, and length of the perturbed optical path. Therefore the error analysis performed is strictly

valid for the apparatus employed (whose optical parameters were previously described) and for a perturbed optical path of 30 cm. The uncertainty in the light deviation Δ_w readings was found to be the major source of error in the h measurements. Several causes contribute to systematic and random errors: preliminary hypotheses (ideal gas assumption, small deflection angles involved), optical coma and astigmatism, light diffraction effects, aberration of optical components, refraction effects within the test section, finite widths of the source slit and of the focal filament, for example. It can be shown that the accuracy in Δ_w readings improves with increasing Δ_w. As a consequence, the uncertainty in h values turned out to be inversely proportional to the recorded Δ_w values. More explicitly, for Δ_w values between 0.8 and 8 mm (range in which the majority of the measurements were performed), the uncertainty in h values was estimated to range from 20 to 8 percent. Since integration averages the noise in the local Nusselt number values, the average Nusselt number data (from integration of local values) are likely to be more accurate than the local Nusselt number data.

The uncertainty in the reconstructed temperature T, assessed by introducing, in the reconstruction procedure for a simulated experiment, an artificial "noise" on input light deflection Δ equal to the corresponding experimental uncertainty, was about 2-4 percent of the maximum wall-to-ambient temperature difference. This gave a maximum uncertainty of ± 0.04 in θ values.

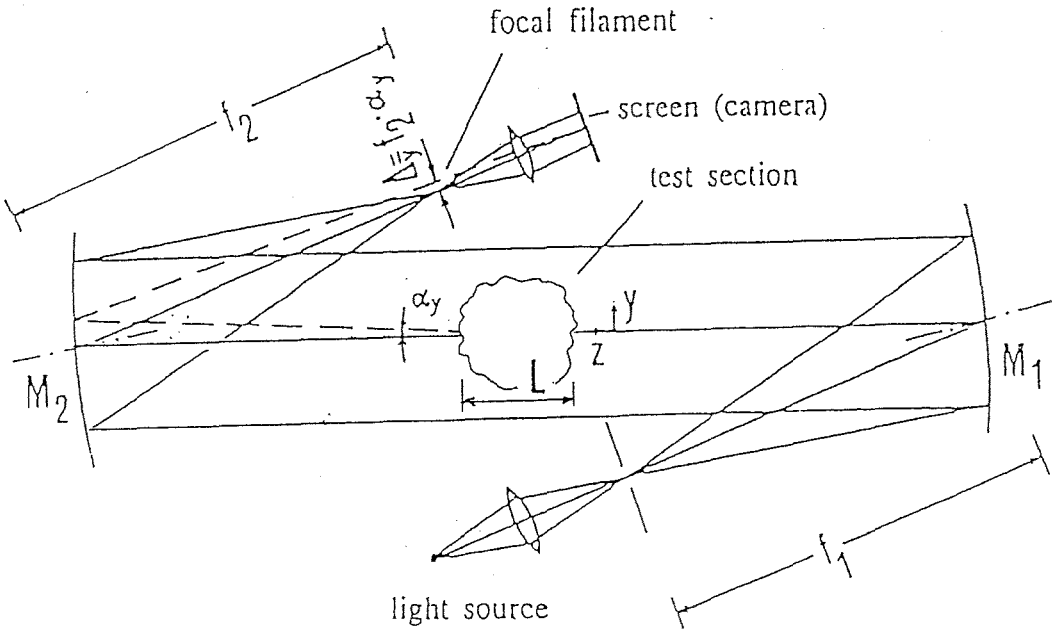

FIGURE A2.1 Light ray deflection in a schlieren apparatus (Z arrangement)

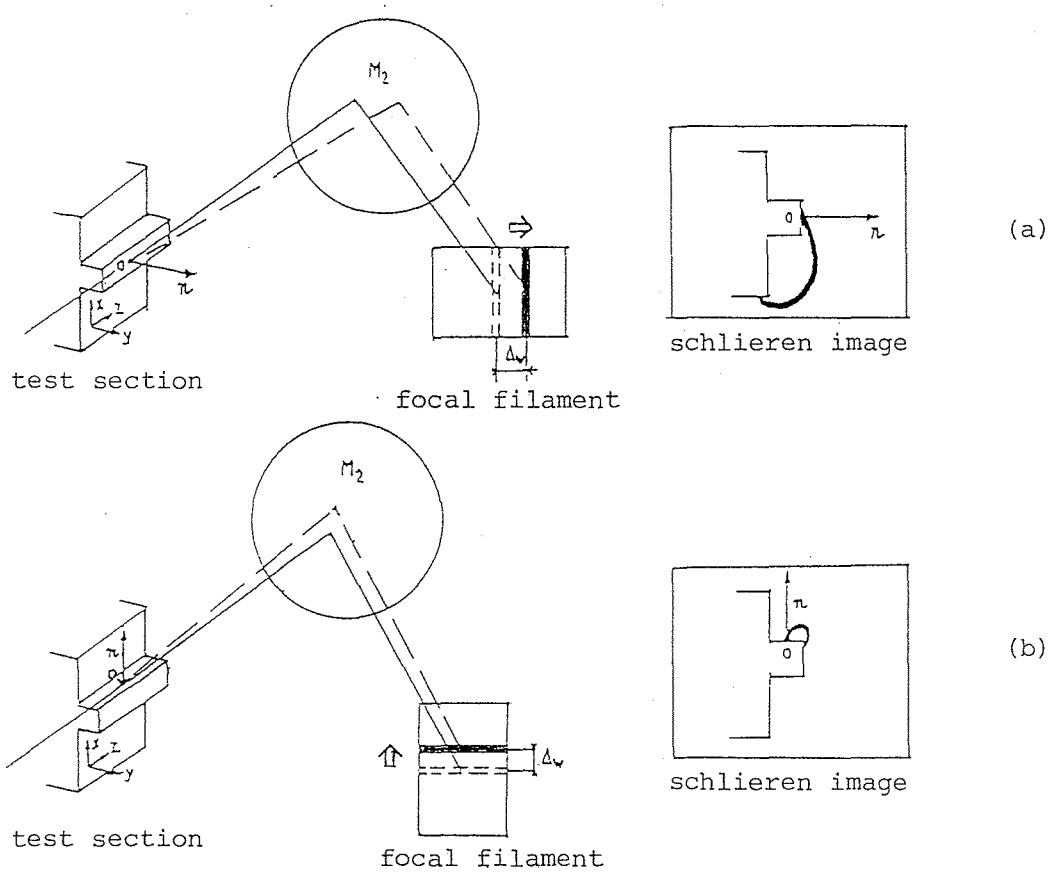

FIGURE A2.2 Schlieren image of a heated square protrusion: the filament shadows indicate the loci of points which deflect light by the same amount Δw (a) along the y-direction, (b) along the x-direction. At the intersection of the filament shadow centreline with the wall profile (point 0) the local heat transfer coefficient is related to the local deviation Δw

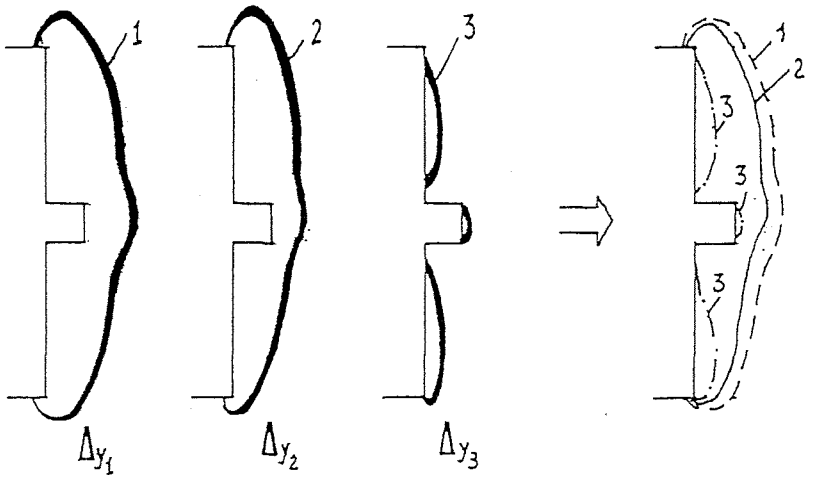

FIGURE A2.3 Overlapping of a series of schlieren images (recorded for a single test) to obtain the pattern of curves at equal light deviation.

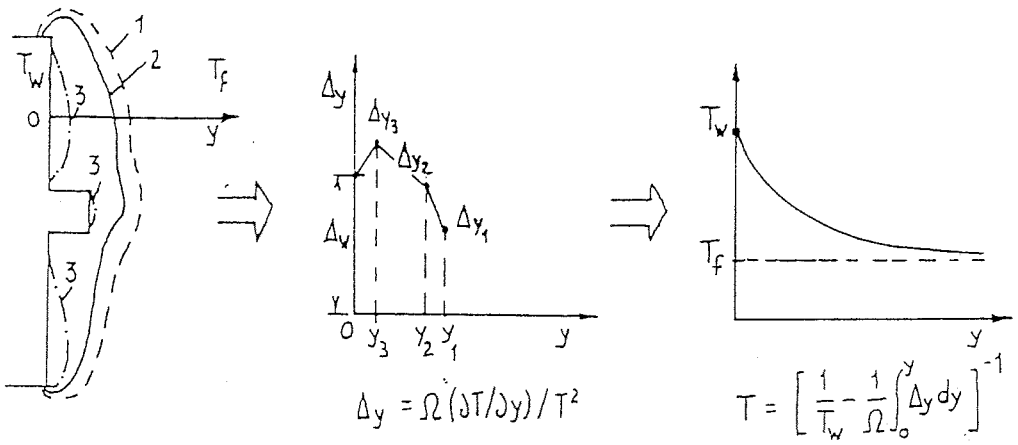

FIGURE A2.4 Reconstruction of the temperature distribution from the pattern of curves at equal light deviation.

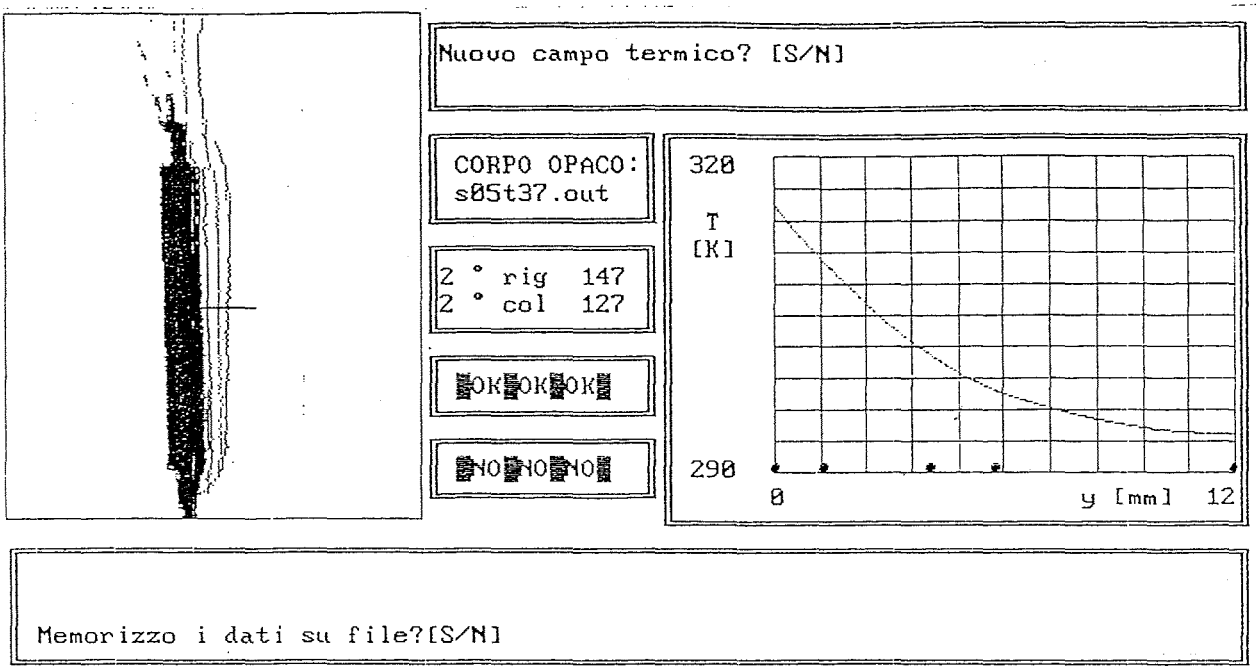

FIGURE A2.5 Print of the computer screen after the automatic temperature profile reconstruction around a heated vertical plate.